INTERNATIONAL JOURNAL OF
IJCOE
COASTAL, OFFSHORE AND
ENVIRONMENTAL ENGINEERING

Experimental and Numerical Study of Scour Beneath Two Pipelines in Tandem Due to Tidal Currents
Darioush Hosseini , Habib Hakimzadeh

Hydrodynamic Effects of Cap Water Entry on Subsea Distribution Unit Suction Caisson Foundation Lowering Response
Mehdi Shirani

Investigation of Microplastics and Heavy Metals contamination in Southwestern Caspian Sea
Sara Emami ,Mohammad Reza Rezaei , Mohammad Hossein Sayadi

Reliability Analysis of Berm Breakwaters based on the environmental data on the Northern coasts of Oman sea
Pouya Zarbipour, Hassan Akbari , Ali SheykhBahai

Tidal Datum Transfer in Shallow Waters: A Comparison of Classical and Parametric Methods in the Northern Persian Gulf
Hamed Esmacil Nazari , Abbas Abedini,Bahman Tajfirooz

The impact of Rivers, Ports, and Coastal Sediment Transport on Sediment Distribution Along the Southern Shore of the Caspian Sea
Mohammadreza Esfandiari, Ulrich Reza Kamalian, Mohammad Babaee Malekshah

Seismic Assessment of Suspended-Zipper Braced Frame (SZBF) in Coastal Steel Structures Equipped with ADAS-SMA Hybrid
Ahmad Hasanpoor Ghadikolaei , Heydar Dashti Naserabadi, Morteza Jamshidi

Integrated Probabilistic Tsunami Hazard and Spectral Energy Analysis of the Makran Subduction Zone: Deriving Hydrodynamic Design Envelopes for Critical Marine Infrastructure near the Strait of Hormuz
Mahmood Reza Akhavpour Jannat, Mohammad Hossein Kazemzadeh

Volume 11 | Issue 2 | MAR 2026
WWW.IJCOE.org info@ijcoe.org

International Journal of Coastal, Offshore and Environmental Engineering (IJCOE) Vol.11/Issue 2 / MAR 2026

International Journal of
Coastal, Offshore and
Environmental
Engineering
ISSN: 2251-6301
Volume 11 | Issue2 | MAR2026
IJCOE

International Journal of Coastal, Offshore & Environmental Engineering
Since 2015
ISSN: 2980-8721 (online)

In The Name of God

Message from the Editor-in-Chief

The IJCOE journal office was established in 2015,and its first issue was published in 2016. TheIJCOE covers a wide range of research in thefields of oceanography & ocean technology, aswell as marine industries & marine engineering.The editorial board of IJCOE consists of nearly130 of the greatest scientists and researchersfrom over 30 countries worldwide, and thejournal's review board comprises 1,000 membersfrom all five continents. The membership andapplication process for joining the editorial andreview boards of this journal is ongoing. IJCOE isa research-academic quarterly journal that haspublication and distribution permissions fromthe Press Organization and permission topublish scientific-research articles from theMinistry of Science, Research, and Technology(MSRT) with an "A" rating. It also holds a "Q1"rating from the ISC institute with an impactfactor (IF) of approximately 0.43 and isconsidered a "core journal" (prestigious andoutstanding journal). IJCOE is an open-accessjournal and allows the download and receipt ofaccepted articles in full text for free. It respectsand adheres to copyright and COPE regulations.The journal's office operates 24/7, providingservices to researchers. In addition to publishinga regular quarterly journal, IJCOE has 16 specialissues on specific topics in preparation. It alsoprovides conditions for publishing specializedbooks, references, and handbooks. Moreover, itis ready to cooperate with the secretariats ofreputable international conferences to publishtheir selected and outstanding articles. IJCOEevaluates, appraises, and publishes books,articles, and the scientific achievements andfindings of esteemed researchers and scientistsworldwide who are innovating and conductingin-depth research in the "important and strategicfield of the maritime technology & Oceanengineering." It welcomes any form of jointcooperation with universities, research institutes,and related research centers at the national,regional, and international levels, and extends ahand for collaboration.

Classification of Editorial Board in IJCOE

- Editor-in-Chief
- Director-in-Chief
- Deputy Editor
- Executive Managers
- English Text Editor
- Technical Editor
- International Editorial Board
- National Editorial Board
- Editorial Board Associate
- Editorial Board Assistant
- Guest Editorial Board
- Advisory Board
- Administrative Coordinator
- Honorary Board Member
- Methodology Advisor

Author Benefits

- Open Access
- Rapid Publication
- Thorough Peer-Review
- No Copyright Constraints
- Coverage by Leading Indexing Services
- Discounts On Article Processing Charges (APC)
- No Space Constraints, No restriction on the maximum length of the papers, number of figures or colors

INTERNATIONAL JOURNAL OF IJCOE COASTAL, OFFSHORE & ENVIRONMENTAL ENGINEERING

Aims of IJCOE

Hydrodynamics

Marine equipment

Structural mechanics

Ocean environmental predictions

Stochastic calculations Experimental

Automatic Control of Marine Systems

Scope of IJCOE

Marine Hazards

Ocean Acoustics

Naval Architecture

Ocean Engineering

Coastal Engineering

Marine Meteorology

Marine Earth Sciences

Underwater Technology

Marine Renewable Energy

Polar & Arctic Engineering

Marine Renewable Energy

Marine Geography & Geodesy

Marine Environmental Engineering

Automatic Control of Marine Systems

Hydro Physics & Physical Oceanography

Type of papers

- Case Studies
- Book Reviews
- Review Article
- Letters to the Editor
- Methodology Papers
- Editorials and Commentaries
- Response or Rejoinder Papers
- Perspective or Opinion Papers
- Conceptual or Theoretical Papers
- Meta-Analysis and Systematic Reviews
- Short Communications or Brief Reports
- Research Articles (Original Research Papers)

Scientific Research Journal

Ministry of Science, Research And Technology (MSRT)

Jurnal Ranking 2023: A

Ministry Of Science, Research And Technology (ISC)

Citation Impact 2022: 0.429

Quartile 2022 : Q1

Core Collection



IJCOE is a Member of



Cantact Us

Office 1 | Research Institute of Meteorology and Atmospheric Science

Address | Tehran, Shahid Kharrazi Highway, Pajoohesh Blvd, Research Institute of Meteorology and Atmospheric Science, Sand and Dust Storm International Research Center (SDS-IRC), No. 13, 1st floor.

Phone | +982144787652

Postal code | 13611-14977

website | www.rimac.ac.ir

Office 2 | Iranian National Institute for Oceanography and Atmospheric Science

Address | Tehran, Dr. Fatemi Gharbi St., Shahid Etemadzade St., No. 3, third floor.

Phone | +982166944873

Postal code | 13389 – 14118

website | www.inio.ac.ir

Email | Info@ijcoe.org

Website | www.ijcoe.org

Follow Us

www.ijcoe.org

INTERNATIONAL JOURNAL OF IJCOE COASTAL, OFFSHORE & ENVIRONMENTAL ENGINEERING

Volume & Issue:

Volume 11, Issue 2, MAR 2026

Number of Articles: 8

Content

Experimental and Numerical Study of Scour Beneath Two Pipelines in Tandem Due to Tidal Currents Darioush Hosseini , Habib Hakimzadeh	1
Hydrodynamic Effects of Cap Water Entry on Subsea Distribution Unit Suction Caisson Foundation Lowering Response Mehdi Shirani	12
Investigation of Microplastics and Heavy Metals contamination in Southwestern Caspian Sea Gammarus Sara Emami ,Mohammad Reza Rezaei , Mohammad Hossein Sayadi	26
Reliability Analysis of Berm Breakwaters based on the environmental data on the Northern coasts of Oman sea Pouya Zarbipour, Hassan Akbari, Ali SheykhBahai	38
Tidal Datum Transfer in Shallow Waters: A Comparison of Classical and Parametric Methods in the Northern Persian Gulf Hamed Esmaeil Nazari , Abbas Abedini,Bahman Tajfirooz	49
The impact of Rivers, Ports, and Coastal Sediment Transport on Sediment Distribution Along the Southern Shore of the Caspian Sea Mohammadreza Esfandiari, Ulrich Reza Kamalian, Mohammad Babaee Malekshah	58
Seismic Assessment of Suspended-Zipper Braced Frame (SZBF) in Coastal Steel Structures Equipped with ADAS-SMA Hybrid Damper Ahmad Hasanpoor Ghadikolaei , Heydar Dashti Naserabadi, Morteza Jamshidi	72
Integrated Probabilistic Tsunami Hazard and Spectral Energy Analysis of the Makran Subduction Zone: Deriving Hydrodynamic Design Envelopes for Critical Marine Infrastructure near the Strait of Hormuz Mahmood Reza Akbarpour Jannat, Mohammad Hossein Kazeminezhad	79

IJCOE
COASTAL, OFFSHORE & ENVIRONMENTAL ENGINEERING

INTERNATIONAL JOURNAL OF
COASTAL, OFFSHORE&ENVIRONMENTAL ENGINEERING IJCOE Vol.11/No. 2/Spring 2026 (1-11)

Available online at: www. Ijcoe.org

Experimental and numerical study of Scour beneath two Pipelines in tandem Due to Tidal Currents

Darioush Hosseini [1], Habib Hakimzadeh[2*]

[1]*Phd student, Faculty of Civil Engineering,Sahand University of Technology, Tabriz;d_hosseini@sut.ac.ir*
[2]*Professor, Faculty of Civil Engineering, Sahand University of Technology, Tabriz; hakimzadeh@sut.ac.ir*

ARTICLE INFO

Article History:
Received 11 Sep2025
Accepted 12 Feb 2025

Keywords:
Submarine Pipes
Tide
Sediment Transport
Laboratory Tests
Numerical Model

ABSTRACT

In industrial applications, multiple parallel pipelines are utilized to connect offshore platforms to coastal facilities. This configuration ensures uninterrupted operation of the coastal facilities in the event of damage to any individual pipeline. The flow and scour patterns around each pipeline are influenced by the factors such as the number of pipelines and their spacing from one to another. In this study, the impact of tidal currents on scouring beneath two identical pipelines placed in a tandem arrangement investigated using both experimental and numerical models. For this purpose, first, the hydrodynamic and sediment transport models based on Flow-3D are used to numerically simulate the local scour around the two tandem pipelines due to bidirectional tidal currents. Then, two series of experiments are carried out for the steady state and bidirectional flow conditions. The experimental results show that for tandem pipelines scour in clear water condition, the maximum scour depths under steady state flow condition exceeds than that caused by bidirectional flow. Further, the scour holes are highly dependent on the bidirectional flow velocity and tidal period as well as the gap between two pipes. When the gap between pipes is equal to one pipe diameter, the scouring depth is lower compared to closely conducted pipes. For this case, each pipe has a unique scour hole with limited dimensions. Finally, the numerical results have been compared with the corresponding experimental data and a relatively good agreement was achieved between them.

1. Introduction

Nowadays, with the increase in the demand for hydrocarbon resources found on the seabed, the use of parallel multiple pipelines for transporting oil, gas, and their derivations to refineries and end-users has become common. For the reasons such as economic analysis, risk reduction, and ensuring the continuity of fluid transfer during a periodic maintenance, installing two or more subsea pipelines is mainly preferred to a single pipeline. Additionally, many pipe-laying barges are capable of simultaneously deploying two pipelines. Regular monitoring conducted on the seabed of subsea pipelines indicates the formation of numerous scour holes along their length, leading to the creation of free spans. The gradual expansion of these free spans along the pipeline results in a significant increase in oscillatory loads, causing fatigue and the eventual rupture of the pipeline. Over the past few decades, numerous studies have been conducted on scour beneath single subsea pipelines caused by unidirectional flow, waves, and their combination (flow-wave interaction).

Research on local scour under pipelines has primarily been approached in two ways: (1) using physical models and laboratory tests, and (2) employing numerical models to solve mathematical equations related to flow dynamic and sediment transport.

In the past, a number of researchers, namely Kjeldsen et al., Leeuwestein, Bijker, Ibrahim, and Nalluri investigated local scour around a single pipeline under the influence of unidirectional flow in the clear water

and live bed conditions[1]. They concluded that the depth of scour caused by the flow was proportional to the pipe diameter, flow velocity, depth of flow, and the size of sediment particles.In a series of laboratory experiments on scour around subsea pipelines, Mao [1] discovered that the scour process comprises two distinct phases: tunnel scour in the initial stages and lee wake scour in the later stages of scour development [1]. Vanbeek analyzed the depth of scour beneath pipelines induced by a constant current [2]. Chiew introduced an empirical function linking the gap flow through the scour hole to the prevailing flow conditions [3]. The authors formulated empirical equations for prediction of the maximum scour depth beneath subsea pipelines. Sumer and Fredsøe extensively investigated scour initiation, the characteristics of equilibrium scour profiles, and the variables that impact them [1]. Furthermore, Cheng et al. performed an experimental study to explore local scour beneath a rigid pipeline. The scour was caused solely by waves and combined wave-current actions [4].

Then, Chao and Hennessy, Chiew, Li and Cheng [5], Hosseini et al. [6], and Sumer et al. [7] developed numerical models based on the potential flow theory to estimate scour profiles. Further, the numerical models that can describe accurately turbulent flows have been employed by Brørs [8], Li and Cheng , Liang et al., Fuhrman et al. [9], and Larsen et al. [10] to simulate the scour process. Also, Yeganeh et al. proposed a two-phase model to explore tunnel erosion beneath submarine pipelines subjected to unidirectional flow [11]. However, despite the possibility of pipelines being placed in a parallel setup, most research on local scour beneath subsea pipelines has predominantly focused on a single, isolated pipeline.

Several studies have been conducted to examine the scouring process beneath two parallel pipelines. Westerhorstmann et al. [12] investigated the impact of a gap (G) between tandem pipelines and found that when G/D=0.5, the scour depths beneath the two pipelines were smaller than those where G/D=1. Moreover, under combined wave and current flow conditions, the scour depths were reduced compared to those observed under steady current flows. Zhang et al. [13] conducted experiments on local scour beneath two identical pipelines arranged in tandem, considering various gap ratios under both live bed and clear water conditions. For clear water conditions, it was observed that when G/D<2, the equilibrium scour depth beneath the upstream pipeline was greater than that of the scour beneath the downstream pipeline, a trend that differs from what is seen in live bed conditions. Zhao et al. [14] explored the effect of the gap ratio between two pipelines on scour through extensive numerical simulations, with gap ratios ranging from 0.5 to 5. Their findings indicated that placing the two pipelines as close as possible would minimize scour depths under both clear water and live bed conditions. Zhao et al. also employed numerical methods to analyze the influence of gap ratio and the KC number on scour depth beneath the pipelines across a wide range of parameters. Li et al. [15] developed a 2D numerical model to study local scour beneath two tandem submarine pipelines under combined wave and current conditions.

Dan et al. employed the CFD–DEM method to simulate local scour around two tandem pipelines [16]. Their findings showed that when G/D≤2, the equilibrium scour depth beneath the upstream pipeline is slightly greater than thatwas under the downstream pipeline. Recently, Maddah et al. conducted an experimental research on scouring around submarine pipelines grouped together due to steady currents [17]. The authors found that while the width of the scour hole increased over time, the scour depth beneath both the downstream and upstream pipes was less than the maximum scour depth observed beneath a single pipe. As previously mentioned, several studies have focused on investigating into the scour phenomenon beneath two tandem pipelines under steady flow, with only one study examining the combined effects of wave and current. Nevertheless, this study presents a specialized investigation of the impact of tidal currents on scouring around tandem pipelines.

Tidal fluctuations continuously alter water levels in open seas, and the persistent and forceful currents produced by tides in bays, straits, and estuaries necessitate the study of phenomena associated with sediment transport, seabed level changes, and scouring around the structures situated in these areas. The behavior of the tide can be considered as a gravity wave that causes periodic changes in the sea level and flow direction. Also, the tidal current is a mostly horizontal bidirectional current that is the result of a tide.

In the Persian Gulf and the Strait of Hormuz, as well as its estuaries, there are multiple pipelines laid down on the sea bed. Significant local scours have been observed during surveys of these submarine pipelines in service. In those areas due to the continuity and dominance of currents caused by tides, it is necessary to investigate the phenomena related to scouring around the subsea parallel pipelines to be illuminated better than before.

More recently, Hosseini et al. [18] simulated scour below a single pipeline resulting from bidirectional currents using FLOW3D. In their numerical model application, they specifically focused on the flow characteristics in the Persian Gulf. Then, they utilized an experimental model to study the clear-water current conditions, taking into account parameters likes velocity, depth, and the number of tidal cycles required to reach the equilibrium stage. Thus, this research study aims to both experimentally and numerically investigate the scouring process around two submarine pipelines in tandem due to tidal currents and compare

the results with those obtained under steady currents for clear-water conditions.

Figure 1 depicts a schematic diagram illustrating the scouring beneath two tandem pipelines of equal diameter. The diameter of the pipeline and the distance between them are represented as D and G, respectively. Pipelines 1 and 2 refer to the upstream and downstream pipelines, respectively. The scour depth beneath the center lines of pipelines 1 and 2 are denoted as S_1 and S_2, respectively.

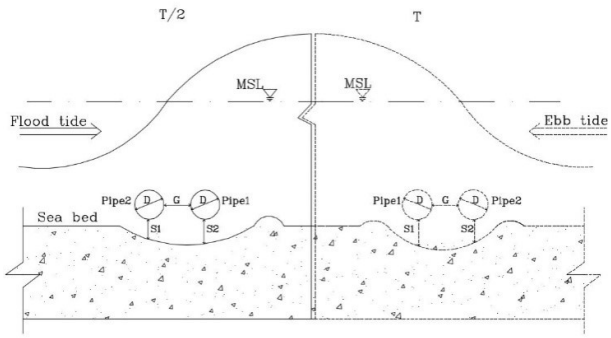

Figure 1. Sketch of scour below two pipelines due to tidal current.

2. Dimensional analysis

The equilibrium scour depth around a pipeline relies on (a) Hydraulic characteristics, (b) Physical properties of the fluid, (c) Geometric parameters, and (4) Sediment parameters. The parameters can be summarized as follows:

$S = f\ (g, \rho, \nu, U, h, T, D, G, _{50}, \sigma_g, \rho_s, B)$ (1)

Here, it may be assumed that the influence of viscosity and sediment non-uniformity are disregarded [19]. Also, uing the Buckingham Pi theorem, Eq. (1) can be condensed and expressed as follows:

$S/D = f\ (Fr, KC, Re, \theta, G/D)$ (2)

On the other hand Sumer and Fredsøe[20]found that the scour depth had a weak correlation with the pipeline's Reynolds number. Consequently, Eq. (2) was simplified as follows:

$S/D = f\ (Fr, KC, \theta, G/D)$ (3)

Then, the resultant equation indicates that the non-dimensional scour depth generally depends on the Froude number, the KC number, the Shields parameter (i.e., θ), and the relative gap between pipes.

3. Materials and methods

Figure 2 displays the experimental setup and dimensions of the flume. A bidirectional flume was constructed for this study at Hydraulics Research Laboratory of Sahand University of Technology. Its length, width and depth are 10m, 0.6m and 1m respectively. Two wired gates are positioned at each end of the flume, allowing control over the water depth. A pump is located beneath the right end of the flume, supplying water from tanks to the channel.The flow direction, velocity, and depth are precisely controlled and regulated using side valves and valves adjacent to the pump.

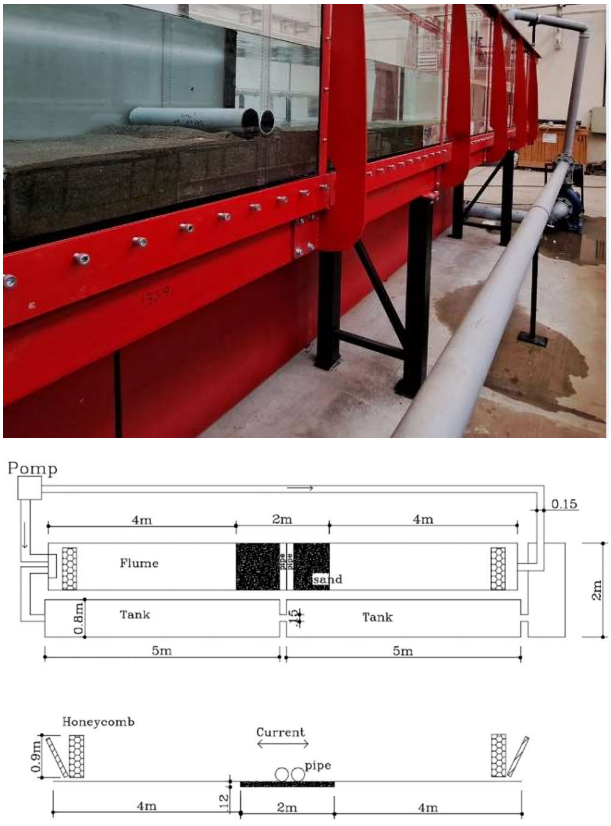

Figure 2: Experimental flume and Sketch of the tests set up.

4. Sediment properties and threshold of movement

The sediment properties used in this study are identical to those that have been used in Asrari et al [19].

For this study, two methods have been employed to ascertain the velocity equivalent to the threshold of movement, which are as follows:

First, sediment movement has been evaluated using the modified Shields diagram [20], based on the dimensionless shear stress parameter θ=0.031. Then, the average critical velocity value is determined using the Melville formula [21]:

$$\frac{U_c}{U_f} = 5.57 \log(5.53 \frac{h}{d_{50}}) \quad (4)$$

Here, *Uc* is the critical mean approach flow velocity for sediments movement and U_f signifies the frictional velocity on the bed. The sediments materials used for this research have a median diameter d_{50}=0.78 mm and h is flow depth.

$$\theta = \frac{U_f^2}{g(s-1)d_{50}} \quad (5)$$

Finally, the critical flow velocity corresponding to the threshold of movement (U_c) is calculated to be 35 cm/s.

In the experimental procedure, once sediment grains began to move, a water velocity meter was deployed to precisely measure the flow speed. The averaged recorded flow velocity was 32.3 cm/s. Therefore, with $U \leq U_c$, the dominance of clear water conditions is evident.

5. Model scale

In coastal modeling, inertia and gravity forces typically dominate, making it crucial to accurately scale the Froude number. The Froude number can significantly impact the scour process, as it affects the water surface profile and, consequently, the flow field around the pipeline. The studied area of this research is the striate of Hormuz in Persian Gulf. The tidal pattern along the Persian Gulf's near shore regions follows a semi-daily rhythm, with a period of approximately 12 hours. In this region, several submarine pipelines have been constructed and are currently operational. The physical model used for this study is a 1:30 scaled-down model of a main gas pipeline. Consequently, the corresponding parameters of the model, based on the measured parameters of the region, have been determined using the Froude law [22].Then, the tidal model periods corresponding to semi-daily (12 hours) is 2.2 hours and water depth is 25-30 cm. In addition, diameter of modeled pipe was 6 cm.

6. Simulation of tidal currents

A simplified approximation of tidal flow involves periodically reversing the direction of a flow with a constant depth-averaged velocity [21 and 22].To scale the flow velocities, the maximum peak velocity within the selected tidal signal has been matched to the flow intensities necessary to achieve clear-water conditions ($U<U_c$), considering the specific sediment properties involved. Figure 3 displays the time history of bidirectional currents velocities for the semi-daily tide. Then, a simplified symmetrical tidal signal was utilized in the laboratory. Each half cycle was divided into five time steps: two during acceleration, one at the peak, and two during deceleration, with a constant current velocity maintained at each time step.

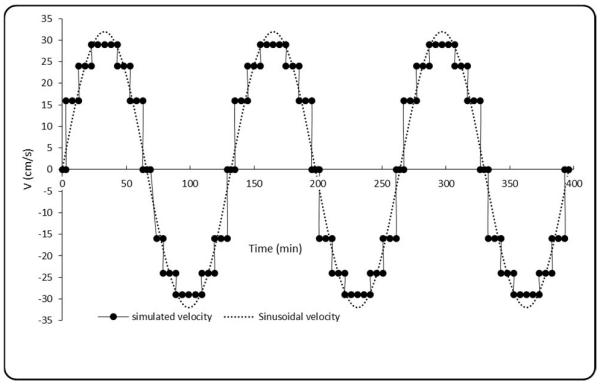

Figure 3: Time history of simulated tidal current velocity

7. Tests program

For examining the scouring caused by tidal flow beneath tandem pipelines with G/D =0.1 and comparing it with the scouring resulting from steady currents, two groups of experiments were conducted under both bidirectional and steady currents in clear water conditions. The first group (A) investigated bidirectional currents. The second one (B) concentrated on studying local scour beneath the pipelines exposed to steady currents. A summary of the experimental set and results are shown in Table 1.

Table 1: A summary of the scour tests conditions.

	Test No.	Cycles	G/D	h (cm)	S_1/D	S_2/D
A	TT1	3	0	25	0.33	0.32
	TT2	3	0	30	0.23	0.23
	TOT3	3	1	25	0.25	0.19
	TOT4	3	1	30	0.21	0.16
B	UTT5	-	0	25	0.36	0.29
	UTT6	-	0	30	0.27	0.23
	UTOT7	-	1	25	0.31	0.21
	UTOT8	-	1	30	0.23	0.13
	U9	-	∞	25	0.48	-
	U10	-	∞	30	0.37	-

8. Experimental results and discussion

The significant results will be analyzed to identify the underlying causes and to compare scour beneath tandem pipelines under both tidal and steady currents. Figures 4, present camera images depicting scour profiles at different time intervals for test no. TT1.

Based on the experimental results, the mechanism of the scouring process in the case of tandem pipes can be explained as follows: the initiation of scour is primarily associated with seepage flow within the bed. In the case of tandem pipes, the elongation of the flow path within the bed causes a delay in piping and subsequent scouring compared to a single pipe. When the pipes are closely positioned, they function nearly as a unified entity, resulting in simultaneous scouring beneath them, resembling the behavior observed with a single pipe. For the first half cycle under steady current conditions, the scour hole initially formed beneath the upstream pipe and then extended to underneath of the downstream pipe. Then, during the initial stages of scouring, the scour depth below the upstream pipe exceeded than that of the downstream pipe. However, over time, this difference decreased, and eventually, the scour depth below the downstream pipe became greater than that of the upstream pipe. Simultaneously, a sand dune is gradually formed downstream. In the second half cycle, however, when the flow direction changed, the above process is reversed and the scour profile becomes more symmetrical. This scenario continued in subsequent cycles until reaching to the equilibrium stage. It is worth noting that, in this scenario, the base

of the scour hole exhibits a wider dimension compared to that of a single pipe.

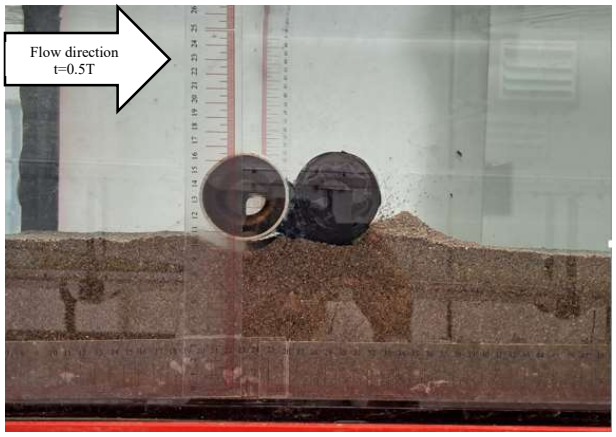

a: Firth half period (t=0.5 T)



b: Sixth half period (t=3 T)

Figure 4: Scouring profile at the end of the first half cycle and the sixth half cycle for tandem pipes, semi daily tidal currents

From the figures 4, it is evident that the second pipe creates a sheltering effect. This effect eliminates the formation of vortices, thereby reducing lee wake erosion and resulting in a narrower scour hole compared to that of a single pipe.

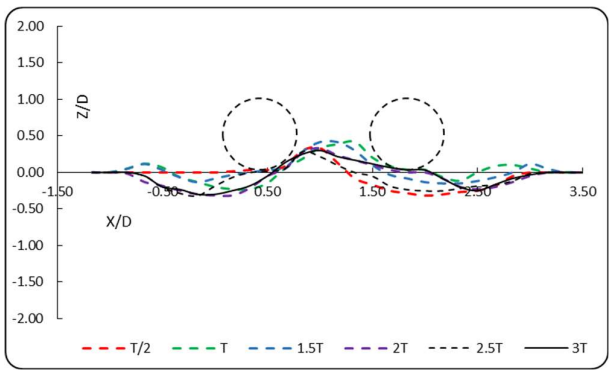

Figure 5: Scouring profile in six consecutive half-cycles of tidal flow (test no. TOT3)

When the G/D=1, the scouring pattern becomes more intricate (figure 5). In the first half cycle, during the flood direction from right to left, sediments removed from underneath of the first pipe (right one) accumulate near the second pipe (left one). Additionally, when the flow direction reverses during the ebb, sediments discharged from the second pipe partially fill the scour hole formed beneath the first pipe. This process continues in alternating cycles.

Figure 6 presents a comparison of the bed scouring profiles for parallel pipes under bidirectional flow conditions. Then, the profile of tandem pipes with G/D approximately equals to zero is contrasted with the scouring bed profile of parallel pipes under steady flow conditions. It is evident that the scour depth under steady flow exceeds the scour depth caused by bidirectional flow. Furthermore, when the G/D=1, the scouring depth is less compared to the cases where the pipes are placed closely together. In this scenario, each pipe forms a distinct scour hole with limited dimensions.

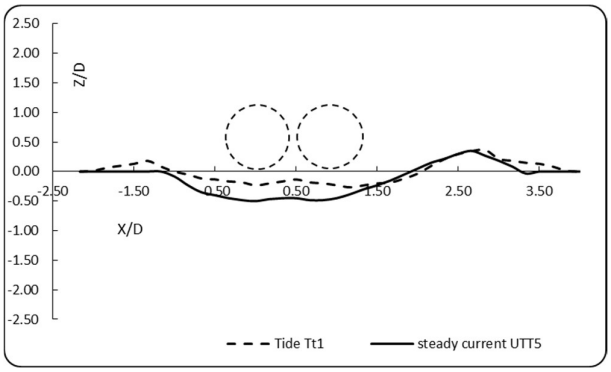

Figure 6: Bed profile under two tandem pipes due to the steady and tidal currents

Therefore, it may be concluded that for the case of two parallel pipelines, the flow dynamics and its interaction with the mobile bed exhibit greater complexity compared to a single pipeline. Depending on the gap between the two pipelines, the lee wake vortices generated by the upstream pipeline are carried downstream and may interact with the downstream pipeline, influencing its scour depth.

9. Numerical model

For this section, a numerical model application is presented using the Flow3D (v11.1) software. The model simulates various stages of the scour process caused by tidal flow beneath the single and parallel pipelines. These stages include the onset of scour, tunnel erosion, lee-wake erosion and scour development using sediment transport equations. The input data include flow velocities, water depth, pipe

diameter, and sediment characteristics. The outputs are flow field around the pipe (velocity, pressure) as well as the depth and width of the scour profile at the end of each tidal cycle. The scour phenomenon is a process that stems from the interaction between the pipeline, the erodible seabed, and the flow field. Therefore, analyzing such a phenomenon requires an understanding of two sets of equations: hydrodynamic equations and sediment transport equations. The hydrodynamic equations must be solved at first stage of every time step since sediment transport equations depend on the flow velocity components. Also, for the scour phenomenon, due to the existing a turbulent flow and vortices around the structure, turbulence models must be employed for numerical simulation.

10. Hydrodynamic Equations

The proposed numerical framework solves the incompressible unsteady Reynolds-averaged Navier-Stokes (URANS) equations utilizing the k-ε turbulence model [8]. The governing equations for the flow in Cartesian coordinate system include a continuity equation and fluid momentum equations:

$$\frac{\partial u_i}{\partial x_i} = 0 \tag{7}$$

$$\frac{\partial u_i}{\partial t} + u_j \frac{\partial u_i}{\partial x_j} = -\frac{1}{\rho_f}\frac{\partial p}{\partial x_i} + \upsilon \frac{\partial}{\partial x_j}\left(\frac{\partial u_i}{\partial x_j} + \frac{\partial u_j}{\partial x_i}\right) - \frac{\partial \overline{u_i' u_j'}}{\partial x_j} + \left(\frac{\rho_s}{\rho_f} - 1\right) cg\,\delta_{i3} \tag{8}$$

In the above equations, u_i represents the velocity components along the coordinate axes x_i, p is the pressure, and ρ is the fluid (water) density.

$$\overline{u_i' u_j'} = \upsilon_T \left(\frac{\partial u_i}{\partial x_j} + \frac{\partial u_j}{\partial x_i}\right) - \frac{2}{3}\delta_{ij} k \tag{9}$$

$$k = \frac{1}{2}\overline{u_k' u_k'} \tag{10}$$

To close the system of equations, the k–ε model is deployed for this model application. Then, the model includes two additional equations: one for k (turbulent kinetic energy) and the other for ε (rate of dissipation of turbulent energy).

$$\frac{\partial k}{\partial t} + u_j \frac{\partial k}{\partial x_j} = -\frac{\partial}{\partial x_j}\left(\frac{\upsilon_T}{\sigma_c} \cdot \frac{\partial k}{\partial x_j}\right) + P + G - \varepsilon \tag{11}$$

$$\frac{\partial \varepsilon}{\partial t} + u_j \frac{\partial \varepsilon}{\partial x_j} = -\frac{\partial}{\partial x_j}\left(\frac{\upsilon_T}{\sigma_c} \cdot \frac{\partial \varepsilon}{\partial x_j}\right) \tag{12}$$

$$+ \left(C_{\varepsilon 1} P - C_{\varepsilon 2} P + C_{\varepsilon 3} \max(0, G)\right)\frac{\varepsilon}{k} \tag{13}$$

$$\upsilon_T = \frac{C_\mu k^2}{\varepsilon}$$

In these equations, ν_T is the turbulent eddy viscosity, and k represents the turbulent kinetic energy. P is the production rate of turbulent kinetic energy k by shear velocity, and G is the production rate of k by gravity, defined as:

$$P = \upsilon_T \frac{\partial u_i}{\partial x_j}\left(\frac{\partial u_i}{\partial x_j} + \frac{\partial u_j}{\partial x_i}\right) \tag{14}$$

$$G = \left(\frac{\rho_s}{\rho_f} - 1\right) cg \frac{\upsilon_T}{\sigma_c}\frac{\partial c}{\partial x_3} \tag{15}$$

11. Sediment model

Utilizing a sediment model, researchers simulate the phenomenon of local scour beneath the pipeline. This model predicts sediment movement by estimating sediment erosion, advection, and deposition. The processes of entrainment, deposition, bed-load transport, and suspended load transport collectively define the process of sediment transport. Entrainment and deposition are described as conflicting processes regulating the overall exchange rate between settled and suspended sediments. When the bed shear stress surpasses the critical shear stress, grains on the seabed may be dislodged and become suspended.

11.1. Suspended load transport

The suspended load is determined by solving a turbulent-diffusion equation that is derived from the concentration continuity principle [23]

$$\frac{\partial c}{\partial t} + \left(u_j - w_s \delta_{j3}\right)\frac{\partial c}{\partial x_j} = -\frac{\partial \overline{c' u_j'}}{\partial x_j} \tag{16}$$

11.2. Bed load transport

The sediment transport rate as bed-load per unit width (considering the bed stability parameter θ and the median sediment grain diameter, d_{50}) is determined using the Nielsen equation as follows:

$$q_0 = 12\sqrt{g(\rho_s/\rho - 1)d^3}\,(\theta - \theta_{cr})\theta^{\frac{1}{2}} \tag{17}$$

The importance of using the Nielsen model lies in the fact that the results obtained from the numerical model show good agreement with experimental results. Furthermore, the numerical model converges in a shorter amount of time.

12. Boundary condition

-At the inlet and outlet boundaries, the conditions of specific velocity and outflow are applied periodically during successive half-cycles. Moreover, at the boundaries of both the inlet and outlet, the water elevations are held constant, assuming a hydrostatic pressure distribution.

-A symmetry boundary condition has been applied to the water surface

-For the sides (walls) and the channel be (Ymin, Ymax, and Zmin), solid boundaries were implemented as the boundary conditions. To evaluate the impact of these boundaries on flow, a widely recognized empirical

equation for the standard wall function is employed (Zhao et al., 2015).

$$\frac{U}{u_*} = \frac{1}{\mathcal{K}} \ln\left(\frac{30y}{k_s}\right) \quad (18)$$

Where k_s is the bed roughness, $\mathcal{K}$ is the von Karman constant and equals to 0.4 and y is the distance from the wall [19].

-No-slip boundary conditions are applied at the pipelines surfaces, indicating that the velocities at these boundaries are zero.

13. Numerical method

The FLOW3D software was used for the section of numerical simulation of this study. The Volume of Fluid (VOF) technique is employed to monitor free water surface. Further, the model incorporates the Fractional Area/Volume Obstacle Representation (FAVOR) approach to model the intricate geometric regions within fixed rectangular meshes.

In Flow-3D, a basic grid consisting of rectangular elements was utilized, offering the benefits of regularity to enhance numerical accuracy and ease of generation. Consequently, a series of simulations were performed using various mesh sizes, focusing on both the accuracy of the numerical solution and the quality of the input data. Prior to commencing any numerical analyses, it is imperative to carefully select an appropriate mesh size. The mesh size should be determined such that it adequately captures all the intricate details of the phenomenon being analyzed. During this discretization process, the dimensions of the channel (i.e., length, width, and depth) are considered to be 200, 60 and 30 cm in the x, y, and z directions, respectively. The finest mesh resolution surrounding the pipe is approximately 6 mm, ensuring that the value of y+ closely approximates 65 during computation. It is noted that a y+ value ranging from 30 to 100 is deemed suitable for the turbulence model.

14. Model validation

In this section, the numerical evaluations have been conducted using two methods to ensure the accuracy of the results. First, to validate the hydrodynamics of the numerical model, a comparison was made with the experimental results of Omrani et al. [23], see figure 7. Based on their findings, which were obtained for the flow separation around a pipe with a diameter of 6cm, the length of the downstream vortex was calculated to be 45 centimeters. For the current study, the vortex length was found to be 46.2 cm, showing good agreement between the numerical results of the present research and the experimental results.

In the second stage, the numerical results of scour development were compared with experimental results. For this purpose, the depth of scour obtained from the numerical model of a single pipe under steady flow was compared with two sets of results provided by previous published data (Table 2).

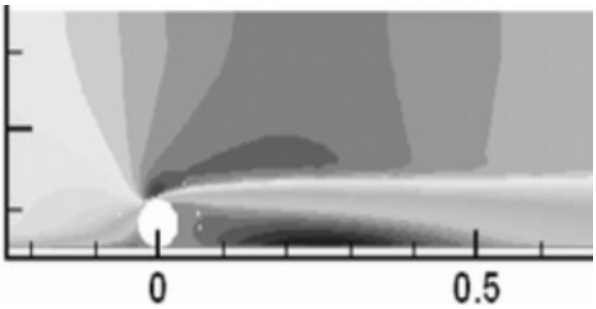

(7a):

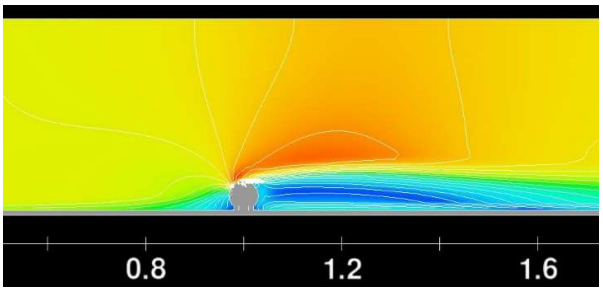

(7b):

Figure 7: Flow filed around pipe, a: Omrani et al. and b: this study.

It can be seen from table2 that the results of present numerical model compared to the results obtained from previous published data are in good agreements.

Table 2: Verification of the present numerical results for a single pipe.

Reference	Model type	D (cm)	S/D
Hosseine et al. [18]	Experimental	6	0.39
Asrari et al [26]	Numerical	6	0.42
This study	Numerical	6	0.43

15. Model applicable

The primary objective of this study is to explore the phenomenon of local scour and the factors that influence on it around two parallel pipelines. As indicated in table 2, the specific parameters are as follows: The diameter of the pipeline is D = 6 cm. The lengths of the sediment beds at the upstream and downstream are 15D, with the latter having a significant impact on the results of the numerical analyses. Furthermore, the flow depth equals to 5D and the depth of the sediment bed is equal to 10 cm. As mentioned in section 1, Hosseini et al. [18] conducted a number of simulations on the scour beneath pipelines arising from bidirectional currents using FLOW3D. The aim here is to juxtapose the results of the numerical simulations with those of the experimental study. To achieve this, the sediment characteristics and pipe diameter remain consistent in both methodologies. The Shields parameter θ is equal to 0.031 for both the experiment and simulation presented herein. This alignment, according to Larsen et al. [10], is acceptable as a non-dimensional comparison between the numerical simulation and the experiment. The

comparison is done in terms of S/D over the non-dimensional time T*, expressed as:

$$T^* = \frac{\sqrt{g(s-1)d_{50}^3}}{D^2}t \quad (19)$$

Where t is the physical time. It can be ensured that the non-dimensional scour developments are comparable between two different scales once the Shields parameter is kept the same.

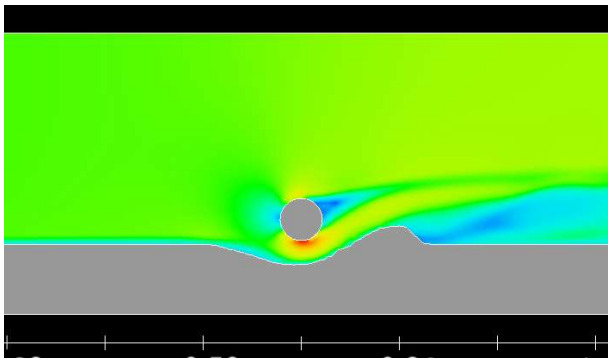

(8a) Single pipe

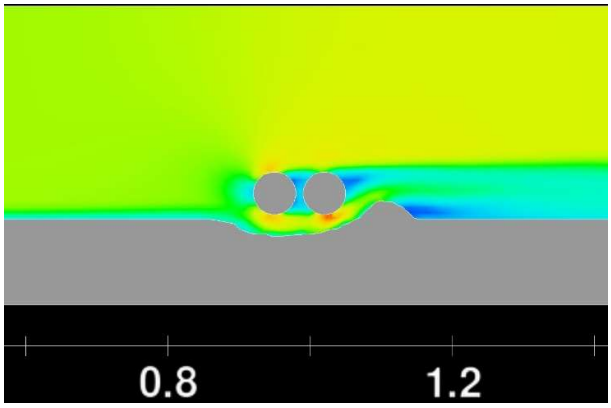

(8b)Tandem pipes G/D=0.1

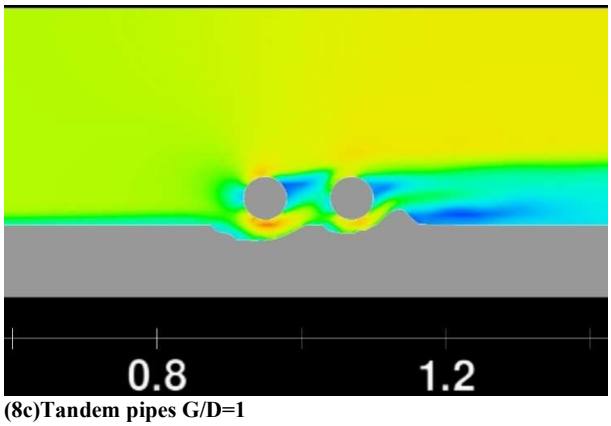

(8c)Tandem pipes G/D=1

Figure 8: Equilibrium scour profile beneath single pipe (a) and tandem pipes with (G/D=0.1 , 1) (b and c) due to steady current(T^*=14.4) .

In Figures 8, the equilibrium steady current-induced scour profiles for single and two parallel pipes with G/D= 0.1, 1 are compared (T*=14.4). As seen, the equilibrium scour depth for the single pipe is greater than that of the tandem pipelines.

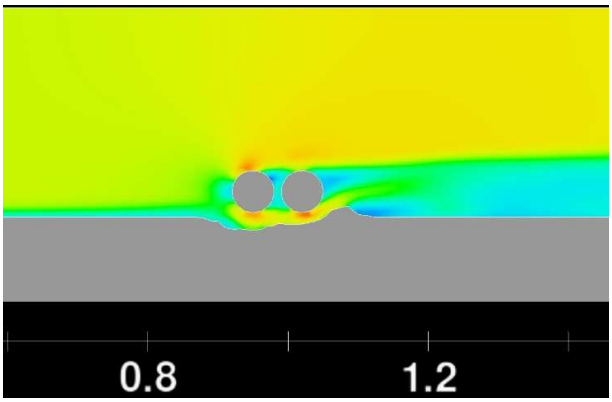

(9a) t=T/2

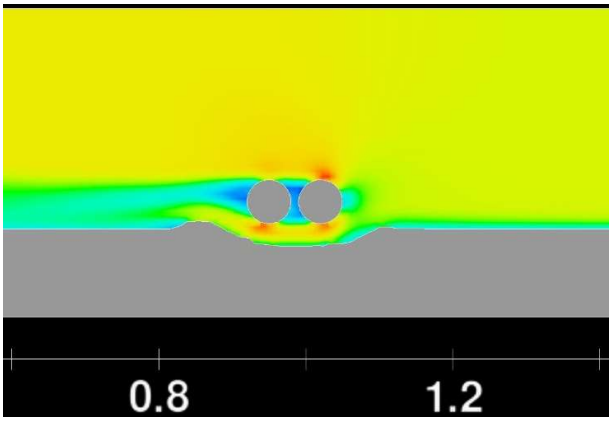

(9b) t=T

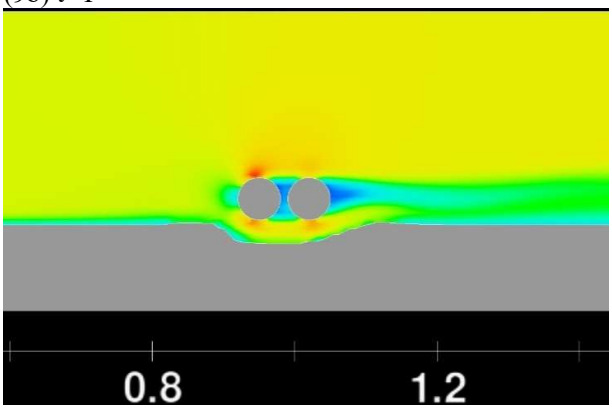

(9c) t=2.5T

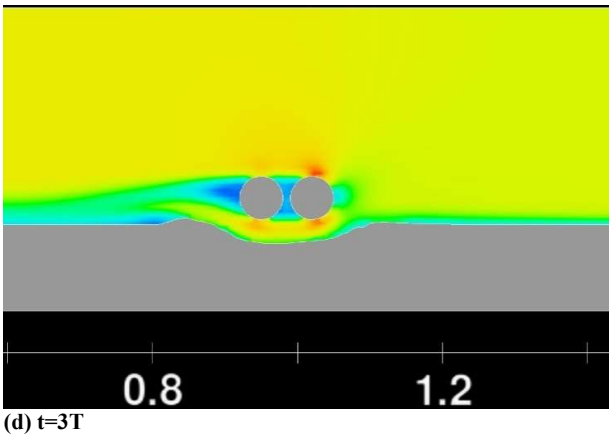

(d) t=3T

Figures 9: Scour profile change with time, calculated by the numerical model

Also under clear water conditions, it becomes evident that for $0 < G/D \leq 1$, the equilibrium scour depth of the upstream pipeline surpasses that of the downstream pipeline. In additions, the bed profiles of the sandy bed across three cycles for G=0.1, and $U/U_c = 0.9$, are depicted in figures 9.

As can be seen during the initial half cycle, the depth of the scour hole escalates rapidly over time. By the conclusion of the first half cycle, two scour holes appear beneath the pipes, with S_1 being larger than S_2 ($S_1 > S_2$), and a sandy dune forms downstream of pipe 2 (Figure 9a). In the subsequent half cycle, as the flow direction reverses, the scour hole beneath pipe2 gradually deeper. Meanwhile, S_1 decreases and another sandy dune arises behind pipe 1 concurrently, as shown in Figure 9b. For the third and fourth half cycles, the variations in the scour depth become notably small, but the width of scouring profile expands, leading to an enlargement of the scouring hole area. This phenomenon indicates the dominance of vortices throwing in the transverse progress of the scour profile, with the reversal of flow direction further intensifying the effect of eddies at this stage, resulting in an equilibrium scour profile with an almost symmetrical shape by the end of the sixth half cycle.

Finally, in table 3 the relative scour depths beneath two tandem pipelines, obtained from experimental data and numerical results for the tidal and unidirectional currents compared with each other.

Table 3: Comparison of the experimental data and numerical results

		Numrical model		Experimental model	
Flow regim	**G/D**	**S1/D**	**S2/D**	**S1/D**	**S2/D**
Tidal current	0	0.38	0.38	0.35	0.35
	1	0.24	0.22	0.27	0.25
Steady current	0	0.36	0.24	0.35	0.3
	1	0.37	0.22	0.33	0.23

As shown in table 3, there are some discrepancies between the two sets of results. However, the numerical results are relatively close to the experimental data and the maximum error is about 10%. The differences between the numerical results and the experimental data may partly be due to the reduced channel length in the computational domain, mesh size, the turbulence model and the bed load formula used in the numerical simulation. Further, some errors may occur in the experimental measurements.

16. Conclusions

This investigation examines the local scouring surrounding two parallel pipelines, scrutinized the phenomenon through the experimental and numerical investigations under clear water conditions with varying gap ratios. The key conclusions drawn include:

1. Unlike to the steady currents, for G/D<1, tidal currents result in a scour profile with two dunes at the upstream and downstream of the pipelines. The shape of the scour hole is nearly symmetrical and the slope is gentler in both directions.
2. In steady currents, as the distance between the two pipes increases from G/D= 0 to 1, the width of the scour hole expands. Also the scour depth decreases with increasing the G/D.
3. In tidal currents for G/D=1 by reversing direction of the flow in each half cycle, the scour hole under the second pipeline is periodically filled by the sediment removed beneath the upstream pipeline. Therefore it is an engineering achievement for scour protection of subsea multiple pipelines.
4. The scour depths beneath the pipelines exhibit a strong positive dependence on the magnitude of flow velocity and G/D. However, no scour is observed below the downstream pipeline when the flow velocity is smaller than $0.6U_c$.
5. The progression of the scour bed profile reveals through three distinct stages: the initiation of scour, scour development, and scour stabilization. During the onset of scour, a sand bar arises between the pipelines, with the size and position of the bar being linked to the initial velocity and G/D. Throughout the scour development, sediment particles transport is the most intense beneath the pipelines.
6. Across all scenarios (G/D = 0 - 1), the scour depth beneath both the downstream and upstream pipes remains lower than the maximum scour depth underneath the single pipeline.
7. For tandem pipelines, the scour depth under uniform flow conditions surpasses that induced by bidirectional flow. Moreover, when the gap between pipes equals the diameter of the pipe, the scour depth is lower compared to the pipes that are placed in close proximity to one another. In such instances, each pipe exhibits a distinct scour hole with constrained dimensions.

17. Acknowledgment

The authors express their gratitude to Dr. Reza Ghiassi, Associate Professor of Civil Engineering Faculty at the University of Tehran, for eagerly consulting the first author.

List of Symbols

B	channel width
d_{50}	median size of bed sediments
D	pipe diameter
Fr	Froude number
g	gravitational acceleration
G	distance between pipes
h	water depth
k	bed roughness
KC	Keulegan-Carpenter number
q_0	sediment transport rate as bed-load per unit width
Re	Reynolds number
s	specific gravity of the sediment

S	scour depth
t	time
T	tidal period
T^*	dimensionless time scale
u_f	frictional velocity on the bed
U_c	critical approach flow velocity
x; y	coordinates in stream-wise and lateral direction
z	vertical direction
θ	shields parameter
θ_{cr}	critical shields parameter
ρ	water density
ρ_s	density of sediment
ν	kinematic viscosity
σ_g	the geometric standard deviation of sediments

18. References

[1]Sumer B. M., Fredsøe J., (2002), The mechanics of scour in the marine environment. World Scientific, Vol. 17, pp 5-136. https://doi.org/10.1142/4942

[2] Vanbeek F.A., and Wind H.G., (1990), Numerical modelling of erosion and sedimentation around offshore pipelines. Coastal Eng. J., 14 pp 107-128. https://doi.org/10.1016/0378-3839(90)90013-M

[3] Chiew, Y.M., (1991). Prediction of maximum scour depth at submarine pipelines. J. Hydraulic Eng., 117(4), pp 452-466. https://doi.org/10.1061/(ASCE)0733-9429(1991)117:4(452)

[4] Cheng, N. S., Wei, M., Xu, P., Mao, R., (2020). Length scale for evaluating wave-induced pipeline scour. Ocean Eng. J., Vol. 218, 108153. https://doi.org/10.1016/j.oceaneng.2020.108153

[5]Li F., Cheng L., (1999), Numerical model for local scour under pipeline. J. Hydraul. Eng., Vol. 125, No. 4, pp 400-406. doi:10.1061/(ASCE)0733-9429(1999)125:4(400)

[6] Hosseini D., Hakimzadeh H., Ghiassi R., (2005), Numerical and Experimental Modeling of Scour around a Submarine Pipeline due to Currents. Proceedings of the Pipeline Division Specialty Conference, Houston, Texas, pp. 793-802.

[7] B.M. Sumer (2007) "Mathematical modelling of scour" Journal of Hydraulic Research Vol. 45, No. 6, pp. 723–735. doi:10.1080/00221686.2007.9521811

[8] Brors, B. (1999). Numerical modeling of flow and scour at pipelines. J. Hydraul. Eng., Vol. 125, No. 5, pp 511-525. https://doi.org/10.1061/(ASCE)0733-9429(1999)125:5(511)

[9] Fuhrman, D.R., Baykal, C., Sumer, B.M., Jacobsen, N.G., Fredsøe, J., 2014. Numerical simulation of wave-induced scour and backfilling processes beneath submarine pipelines. Coast Eng. 94, 10–22.https://doi.org/10.1016/j.coastaleng.2014.08.009

[10] Larsen, B.E., Fuhrman, D.R., Sumer, B.M., 2016. Simulation of wave-plus-current scourbeneath submarine pipelines. J. Waterway. Port, Coastal, and Ocean Engineering, 142(5), Article04016003.https://doi.org/10.1061/(ASCE)WW.1943-5460.0000338.

[11] Yeganeh-Bakhtiarya, A., Kazeminezhad M. H., Etemad-Shahidi, A., Baas J. H. , Cheng, L., (2016). Euler–Euler two-phase flow simulation of tunnel erosion beneath marine pipelines. Applied Ocean Research 33 (2011) 137–146.https://doi.org/10.1016/j.apor.2011.01.001

[12] Westerhorstmann, J.H., Machemehl, J.L., Jo, C.H., 1992. Effect of pipe spacing on marinepipeline scour. Proceeding Of The 2nd International Offshore and Polar Engineering Conference. San Francisco, June 14–19.

[13] Zhang, Q., Draper, S., Cheng, L., Zhao, M., An, H., 2017. Experimental study of localscour beneath two tandem pipelines in steady current. Coast Eng. J. 59, 1750002.DOI: 10.1142/S0578563417500024.

[14] Zhao, M., Vaidya, S., Zhang, Q., Cheng, L., 2015. Local scour around two pipelines in tandem in steady current. Coast Eng. 98, 1–15.http://dx.doi.org/10.1016/j.coastaleng.2015.01.001.

[15]Li A., Ong M., C., Fuhrman D. R., Larsen B. L., (2020).Numerical investigation of wave-plus-current induced scour beneath twosubmarine pipelines in tandem. Coastal Engineering 156 (2020) 103619. https://doi.org/10.1016/j.coastaleng.2019.103619.

[16] Dan H., Wen T., Liang S., Fen L., Xiangying J., Zheng D., (2019). Numerical simulation of local scour around two pipelines in tandem using CFD–DEM method.Applied Ocean Research 93 (2019) 101968.https://doi.org/10.1016/j.apor.2019.101968.

[17] Maddah S., Kolahdouzan F., Eftekhari A., Singh V. P., Afzalimehr H., (2021).Experimental investigation of scouring in groups of parallel pipelines. International Journal of Hydraulic Engineering 2021, 10(2): 27-34. DOI: 10.5923/j.ijhe.20211002.01.

[18] Hosseini D., Hakimzadeh H., Ghiassi R., (2023), Simulation of scour beneath a pipeline due to tidal currents. J. Marine Eng., Vol. 19, No. 39, pp. 1-11.doi: 10.61186/marineeng.19.39.1.

[19] Asrari, S., Hakimzadeh, H. and Kardan, N. (2021), Investigation on the local scour beneath piggyback pipelines under clear-water conditions. China Ocean Eng. J., Vol 35, No. 3, pp. 422-431. https://doi.org/10.1007/s13344-021-0039-7

[20] Van Rijn L. C., (2005). Principles of sedimentation and erosion engineering in rivers, estuaries and coastal seas. Aqua Publications.

[21] Schendela A., Hildebrandta A., Gosebergb N., Schlurmann T., (2018), Processes and evolution of scour around a monopile induced by tidal currents. Coastal Eng. J., Vol. 139, pp. 65–84.doi.org/10.1016/j.coastaleng.2018.05.004.

[22] Porter K. E., Simons R., Harris J. and Ferradosa T. F., (2012), Scour development in complex sediment beds., 33rd Coastal Eng. proceedings, Vol. 1, No. 33, Santander, Spain.

[23] Omrani S. and Hakimzadeh H., (2009). Numerical and experimental investigation of flow separation phenomenon around smi-buried pipelines due to steady currents" Journal of marine Eng.,Vol. 4, No. 8, pp 65-76. https://doi.org/ 20.1001.1.17357608.1387.4.8.6.5

INTERNATIONAL JOURNAL OF
COASTAL, OFFSHORE & ENVIRONMENTAL ENGINEERING IJCOE Vol.11/No. 2/Spring 2026 (12-25)

Available online at: www. Ijcoe.org

Hydrodynamic Effects of Cap Water Entry on Subsea Distribution Unit Suction Caisson Foundation Lowering Response

Mehdi Shirani[1]

[1] *Assistant Professor, Research Institute for Subsea Science and Technology, Isfahan University of Technology, Isfahan, Iran; mehdi.shirani@iut.ac.ir*

ARTICLE INFO

Article History:
Received 18 oct 2025
Accepted 18 Feb 2025

Keywords:
Subsea Distribution Unit (SDU)
Suction caisson
Offshore lowering
Operability
OrcaFlex

ABSTRACT

Lowering a suction-caisson-type subsea structure through the splash zone is a difficult modelling problem because the governing response is controlled by rapidly changing hydrodynamic conditions at free-surface crossing. This paper presents a time-domain OrcaFlex analysis of the lifting and lowering of a Subsea Distribution Unit (SDU) Suction Caisson foundation. The hydrodynamic representation combines a main hollow-body spar-buoy model with two auxiliary buoy corrections: one to account for the additional axial added mass that develops when the caisson cap crosses the free surface, and one to account for the inertia of the water entrapped within the structure after submergence. Environmental screening was performed in the time domain using deterministic regular waves over a matrix of wave heights, periods, and headings. The operability maps show that the splash-zone stage governs the operation. A dedicated case study for wave direction 0°, H = 0.5 m, and T = 6 s further demonstrates the sensitivity of the response to the auxiliary buoy modelling. Relative to the base model without the two auxiliary buoys, activating the entrapped-water buoy increases the peak crane-cable tension from about 680 kN to 779 kN, while activating both the entrapped-water and axial-added-mass buoys raises it to about 907 kN and produces the longest post-entry oscillations. The results confirm that realistic suction-caisson lowering analysis requires explicit treatment of both entrapped-water inertia and cap-entry axial added mass, because these mechanisms control the transient splash-zone response and the resulting operability limits.

1. Introduction

Subsea suction caisson installation is one of the most hydrodynamically sensitive operations in offshore oil and gas field development because the governing response often occurs during sea-surface crossing, when the structure transitions from an in-air body to a partially submerged, then fully submerged, body within a short time window [1-5]. In this stage, the payload is influenced simultaneously by vessel-motion transfer through the crane system, time-varying buoyancy, drag, free-surface effects, rapidly increasing added mass, and, for partially enclosed geometries, the inertia of water that becomes trapped inside the structure [1,2,4,5]. As a result, splash-zone lowering of suction-caisson-type bodies cannot be reliably assessed using a simplified, fully submerged representation alone [2,4,5].

In offshore oil and gas developments, a Subsea Distribution Unit (SDU) is a subsea-installed unit that supports the distribution and connection of production, control, and utility functions within the subsea system [6]. Depending on the field architecture, the unit may form part of a foundation-supported subsea arrangement that connects or supports associated subsea hardware on the seabed [6]. In the present study, the analysed SDU suction caisson foundation is treated as a foundation-supported subsea distribution unit with suction-caisson-type characteristics. From an installation perspective, it functions as a tall, partially enclosed tubular body

with a capped upper region and an internal cavity. These geometric features are crucial because they govern the hydrodynamic response during free-surface crossing and directly affect crane-cable tension, declination, and operability.

A substantial portion of the published literature on subsea installation has focused on splash-zone phenomena, as this stage is often associated with the most severe transient hydrodynamic response [1-5]. Review of work on subsea lifting modelling has shown that splash-zone crossing, the fully submerged stage, and the near-seabed stage are the main response windows of interest, while free-surface loading, transient hydrodynamics, and operability assessment remain challenging topics [1]. Studies on subsea templates, spool pieces, subsea trees, and other lowered structures have similarly shown that time-domain modelling is required when allowable sea states are governed by transient coupled response rather than by a single quasi-static load measure [2-4].

For suction-caisson-type structures, however, the modelling challenge is even more specific. When the caisson cap approaches and then hits the water surface, the body no longer behaves as a simple hollow tubular frame. Instead, the free-surface intersection can generate a rapid increase in axial added mass, while continued submergence may produce the inertia of water entrapped inside the caisson [5]. These mechanisms alter the vertical hydrodynamic inertia, influence the stability of structural motion, and can produce pronounced fluctuations in crane-cable motion during lowering [5]. Previous studies on suction-pile or suction-anchor lowering have highlighted the importance of proper splash-zone modelling, but there remains a practical need for engineering studies that translate these hydrodynamic effects into response-based operability criteria directly useful for offshore execution [5].

The present paper addresses this need by analysing the lifting and lowering of an SDU foundation using a staged time-domain OrcaFlex model. Particular attention is given to the hydrodynamic idealisation required to represent suction-caisson behaviour at sea-surface crossing [5]. The SDU foundation is modelled using a main hollow-body buoy representation supplemented by two local auxiliary buoy corrections: one for the additional axial added mass that develops when the upper cap crosses the free surface, and one for the inertia of the water entrapped inside the structure after cap submergence [5]. The main purpose of the paper is therefore not only to assess operability, but also to show why realistic suction-caisson lowering analysis requires explicit treatment of cap-entry hydrodynamics [5].

The objective of the study is to determine the governing installation stage of the SDU foundation and to quantify the influence of splash-zone hydrodynamics on crane-cable response. The novelty of the work lies in three main aspects. First, it focuses specifically on the lowering behaviour of a suction-caisson-type subsea foundation structure rather than on an open-frame subsea unit. Second, it develops a practical OrcaFlex [7] modelling strategy to represent both entrapped-water inertia and the additional axial added mass arising when the suction caisson cap intersects the free surface. Third, it demonstrates that the governing operability stage is the splash zone, where cap-water interaction destabilises the lowering response and increases crane-cable fluctuations, rather than the fully submerged lowering phase. The study is therefore intended to provide both a project-relevant assessment and a more general modelling framework for suction-caisson splash-zone analysis.

2. Description of the installation system

Figure 1 presents the analysed SDU foundation geometry together with the equivalent OrcaFlex idealisation used in the numerical model. Figure 1(a) shows an isometric view of the analysed SDU foundation, while Figure 1(b) shows the equivalent OrcaFlex model. In Figure 1(b), the auxiliary buoy “AxialAddedMassTopSeaSurface” is indicated in blue, and the auxiliary buoy “ExtraMassTrappedWater” is indicated in red.

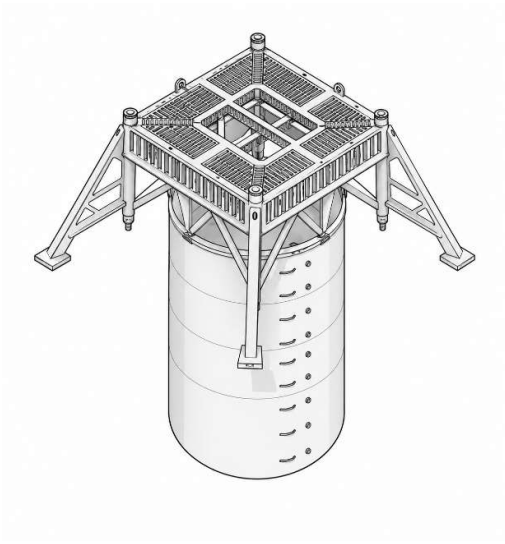

(a)

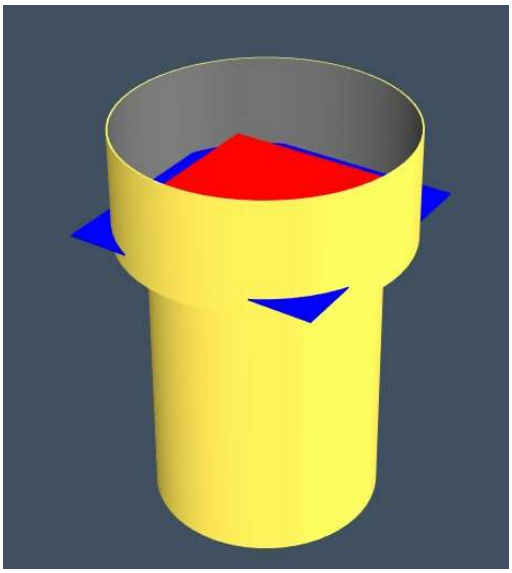

(b)

Figure 1- (a) Isometric view of the analysed SDU foundation; (b) equivalent OrcaFlex model, the auxiliary buoy "AxialAddedMassTopSeaSurface" is shown in blue, and the auxiliary buoy "ExtraMassTrappedWater" is shown in red.

The main properties adopted for the numerical model are summarised in Table 1.

Table 1- Main properties of the SDU foundation used in the numerical model.

Property	Value
Width	7.0 m
Height	12.5 m
Dry installation weight in air	68.878 t
Fully submerged weight	59.218 t
Buoyancy during lowering	8.954 t
Displaced volume in seawater (ρ = 1.025 t/m³)	8.736 m³
Centre of gravity, x	0.0 m
Centre of gravity, y	0.0 m
Centre of gravity, z	7.9 m
Ixx about the centre of mass	1500 t·m²
Iyy about the centre of mass	1500 t·m²
Izz about the centre of mass	1119.3 t·m²

3. Numerical methodology

3.1 OrcaFlex model formulation

The dynamic installation model was developed in OrcaFlex v11.6b using the time-domain approach. The vessel motions were introduced through imported response amplitude operators (RAOs) derived from third-party diffraction analysis. During lift-off from the cargo barge, non-axisymmetric two-body RAOs for the installation vessel and the barge were used. During lowering after barge departure, single-body RAOs for the installation vessel were used and treated as axisymmetric for operability assessment.

Figure 2 shows the OrcaFlex model set-up adopted for the two principal installation stages. Figure 2(a) illustrates the lifting model, while Figure 2(b) shows the lowering model after barge departure.

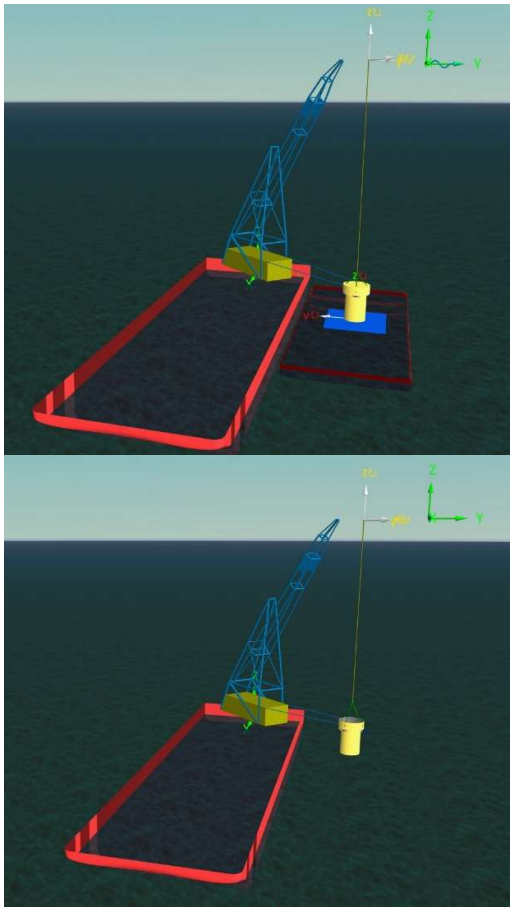

(a)

(b)

Figure 2- OrcaFlex model set-up for the analysed installation stages: (a) lifting model; (b) lowering model.

Figure 3 shows the axes directions and sign convention used in OrcaFlex for the vessel coordinate system.

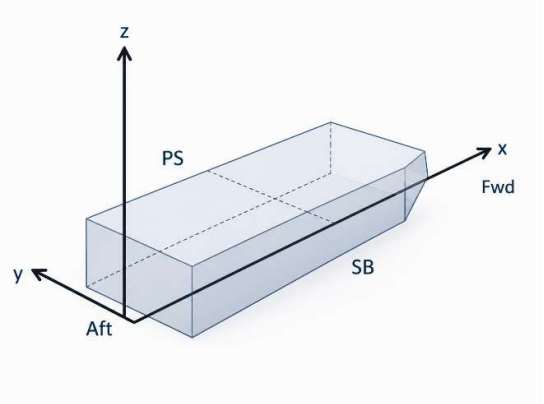

Figure 3- OrcaFlex axes in the vessel coordinate system.

3.2 Environmental conditions

The wave data used in the environmental screening are summarised in Table 2, which reports the wave height H, the associated wave

period T, and the analysed wave directions. Figure 4 shows the wave angle relative to the vessel.

The environmental screening analyses were carried out in the time domain using deterministic regular waves defined by wave direction, height, and period. In the OrcaFlex model, the regular-wave kinematics were represented using Dean stream-function wave theory with stream-function order 5. The regular-wave cases were used as the primary design-wave simulations for operability screening.

Table 2. Wave data used in the environmental screening.

Parameter	Unit	Value
H	m	0.25–2.0 with step 0.25
T	s	4.0–14.0 with step 1
Wave direction	degree	0–360 with step 22.5

Figure 4 illustrates the wave directions defined relative to the vessel, which are used throughout the hydrodynamic and operability assessments.

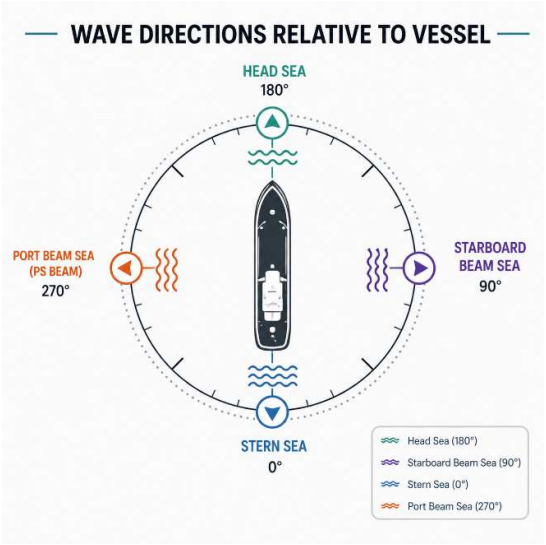

Figure 4- Wave directions relative to the vessel.

For the lift-off phase, where the installation vessel and cargo barge were modelled together, the motion input was based on the corresponding two-body RAOs. Because these RAOs are non-axisymmetric, operability for this phase was assessed for wave headings from 0° to 337.5° in 22.5° increments, giving 16 analysed directions. Combined with 8 wave-height cases and 11 wave-period cases, this produced a total of 1408 regular-wave load cases for the lift-off model.

For the lowering model, after the barge had departed, only the installation vessel remained in the simulation, and the motion input was based on single-body RAOs treated as axisymmetric. Accordingly, the directional range was reduced to 0° to 180°, which corresponds to 9 analysed headings with the same 22.5° increment. Using the same H and T ranges, therefore, yielded 792 regular-wave load cases for the lowering model.

Water depth was 154 m, and seawater density was taken as 1025 kg/m³. Current and marine growth were neglected in the present analysis, consistent with the adopted modelling basis.

3.3 Hydrodynamic coefficients

The adopted hydrodynamic values are summarised in Table 3. The added-mass coefficient taken from DNV guidance [8-9] was converted to the corresponding OrcaFlex Ca format.

Table 3- Calculated hydrodynamic coefficients adopted for the SDU foundation suction caisson model.

Geometry	Added Mass Normal	Added Mass Axial	Drag Normal	Drag Axial	Slamming coeff.	Reference
Tubular structures	1.0	N.A.	0.85	0.008	N.A.	DNV-RP-C205 [8] / DNV-RP-N103 [9]

3.4 Hydrodynamic representation of the SDU foundation

The hydrodynamic model of the SDU foundation was implemented using one main 6D spar buoy and two auxiliary 6D lumped buoys, Figure 2(b). The main spar buoy, denoted "SDU-FOUNDATION", represents the principal tubular geometry of the SDU foundation and carries the global structural mass, centre of gravity, rigid-body inertia, buoyancy variation, and the general drag response of the foundation during lifting, splash-zone crossing, and lowering.

For most of the splash-zone lowering operation, water inside the suction caisson can move axially in and out through the bottom opening, so the axial added-mass effect remains limited. However, once the top cap approaches and contacts the water surface, the water inside the caisson can no longer move freely. Instead, part of the internal water becomes constrained to move together with the structure in the vertical direction. As a result, both the effective axial added mass and the associated fluid inertia increase during free-surface crossing.

In addition to this increase in outer-body axial added mass, a further hydrodynamic effect develops after cap submergence: an internal body

of water becomes entrapped within the caisson cavity, contributing additional vertical inertia to the lowering system. To represent these mechanisms in OrcaFlex, the SDU foundation model was divided into three buoy objects: one spar buoy carrying the main physical and hydrodynamic properties of the structure, one lumped buoy representing the additional axial added mass that develops when the cap hits the sea surface, and one lumped buoy representing the entrapped water inside the suction caisson.
The conceptual arrangement of the three buoy objects used to represent the main suction caisson, the additional axial added mass, and the entrapped water is shown in Figure 5.

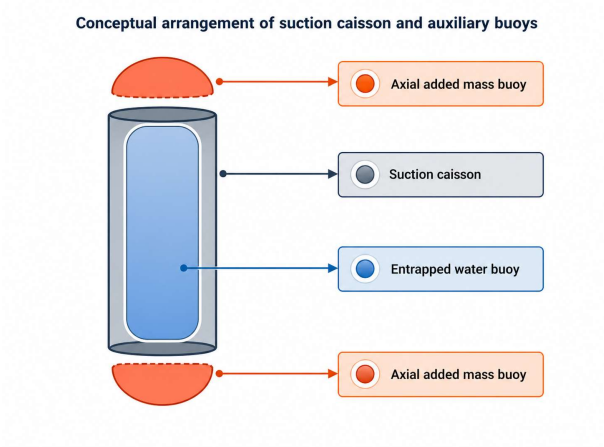

Figure 5- Conceptual sketch of the suction caisson model showing the auxiliary buoy arrangement used to represent axial added mass and entrapped water.

3.4.1 Additional axial added mass at sea-surface crossing

The purpose of this calculation is to estimate the additional vertical hydrodynamic inertia that develops when the top cap of the suction caisson crosses the water surface. At this stage, the structure no longer behaves like a simple slender body moving in open water. Instead, the presence of the cap and the vertical-sided caisson geometry cause the surrounding water to resist the vertical motion more strongly. In practical terms, this manifests as an increase in heave added mass, which must be included in the OrcaFlex model to realistically reproduce the splash-zone response.

For the analysed SDU suction caisson, the main geometric parameters are:

- Outer diameter, $OD = 7.0$ m
- Inner diameter, $ID = 6.96$ m
- Suction caisson height, $h = 9.5$ m

The seawater density is taken as:

$$\rho = 1025\ \text{kg/m}^3$$

Following the simplified DNV-RP-N103 [9] method for three-dimensional bodies with vertical sides, the first step is to evaluate the vertical-sides parameter:

$$\lambda = \frac{\sqrt{A_P}}{h + \sqrt{A_P}}$$

where A_P is the horizontal projected area of the caisson. For the present circular outer geometry,

$$A_P = \frac{\pi OD^2}{4} = \frac{\pi(7.00)^2}{4} = 38.4845\ \text{m}^2$$

and therefore

$$\sqrt{A_P} = 6.2036\ \text{m}$$

Substituting into the definition of λ,

$$\lambda = \frac{6.2036}{9.50 + 6.2036} = 0.3950$$

The parameter λ expresses the relative importance of the caisson plan area compared with its height and is used in the DNV method [9] to correct the heave added mass for a three-dimensional body with vertical sides.

The corresponding DNV [9] height-correction expression is:

$$A_{33} = \left[1 + \sqrt{\frac{1-\lambda^2}{2(1+\lambda^2)}}\right] A_{33o}$$

where:

- A_{33} is the corrected heave added mass of the outer body,
- A_{33} is the reference heave added mass for a flat circular disc.

Substituting $\lambda = 0.3950$,

$$\frac{A_{33}}{A_{33o}} = 1 + \sqrt{\frac{1 - 0.3950^2}{2(1 + 0.3950^2)}} = 1.6042$$

Hence,

$$A_{33.\text{outer}} = 1{,}6042\, A_{33o}$$

The reference added mass A_{33} is taken from the flat-disc expression in the DNV guidance [9]. Using the outer radius of the caisson,

$$a = \frac{OD}{2} = 3.50 \text{ m}$$

the reference disc added mass becomes:

$$A_{33o} = \frac{8}{3}\rho a^3$$

Thus,

$$A_{33} = \frac{8}{3}(1025)(3.50)^3 = 117{,}193 \text{ kg}$$

or

$$A_{33o} \approx 117.2 \text{ t}$$

Therefore, the corrected outer-body heave added mass is:

$$A_{33,\text{outer}} = 1.6042 \times 117{,}193 = 188{,}064 \text{ kg}$$

that is,

$$A_{33,\text{outer}} \approx 188.1 \text{ t}$$

This value represents the additional vertical added mass associated with the outer caisson body when the cap region interacts with the free surface. In the present modelling approach, this added mass is assigned to the auxiliary buoy "AxialAddedMassTopSeaSurface" in OrcaFlex.

Following the Orcina *F07 Suction Anchor Lowering* [10] modelling approach, the buoy is specified using:

- Hydrodynamic mass in Z: 188.1 t
- $C_a(z) = 1.0$

At this point, it is useful to clarify why both hydrodynamic mass and an inertia coefficient are specified. In OrcaFlex, the axial added-mass behaviour can be represented in terms of a coefficient relative to the displaced mass of the buoy. Since the hydrodynamic mass has already been determined from the DNV formula [9], the corresponding displaced-water-based inertia coefficient must be back-calculated so that the OrcaFlex buoy reproduces the same effective axial inertia.

This is done from:

$$C_m = 1 + \frac{\Delta}{A_{33,\text{outer}}}$$

where Δ is the displaced mass of water associated with the outer caisson volume:

$$\Delta = \rho A_P h$$

Substituting the present dimensions,

$$\Delta = 1025 \times \frac{\pi(7.00)^2}{4} \times 9.50 = 374{,}805 \text{ kg}$$

Hence,

$$C_m = 1 + \frac{374{,}805}{188{,}064} = 2.99$$

Therefore, for the buoy "AxialAddedMassTopSeaSurface",

$$C_m(z) \approx 2.99$$

In physical terms, this means that the buoy is calibrated so that its vertical dynamic response reproduces the solid-body-like axial added mass generated when the suction caisson cap crosses the sea surface. The procedure follows the Orcina modelling philosophy: first, determine the required axial hydrodynamic mass from theory; then, back-calculate the inertia coefficient so that the OrcaFlex buoy reproduces the same effective added-mass behaviour.

As a result, the buoy "AxialAddedMassTopSeaSurface" does not represent the global buoyancy of the whole SDU foundation. Instead, it is a local hydrodynamic correction introduced only to capture the extra axial inertia that becomes important during free-surface crossing.

3.4.2 Entrapped-water inertia after top-cap submergence

In addition to the outer-body axial added mass, a second hydrodynamic effect must be represented during lowering. Once the top cap of the suction caisson has passed below the water surface, water becomes trapped inside the caisson cavity and can no longer move freely as the structure continues to descend. This trapped internal water does not provide additional buoyancy in the usual sense, since the overall hydrostatic behaviour is already accounted for by the main SDU spar buoy. However, it does contribute inertia, since part of the internal water column is effectively forced to move together with the structure in the vertical direction.

For this reason, the trapped-water effect is represented separately in the OrcaFlex model by the auxiliary buoy "ExtraMassTrappedWater". The role of this buoy is not to represent geometry or hydrostatics, but only to add the correct vertical hydrodynamic mass associated with the internal water column after top-cap submergence.

The trapped-water volume is estimated from the internal cylindrical volume of the suction caisson:

$$V_{\text{trapped}} = \frac{\pi I D^2 h}{4}$$

where:

- $ID = 6.96$ mis the inner diameter of the suction caisson,
- $h = 9.5$ mis the caisson height,
- $\rho = 1025\ \text{kg/m}^3$is the seawater density.

Substituting the present dimensions,

$$V_{\text{trapped}} = \frac{\pi(6.96)^2(9.50)}{4} = 361.44\ \text{m}^3$$

The corresponding trapped-water mass is then:

$$M_{\text{trapped}} = \rho V_{\text{trapped}}$$

Hence,

$$M_{\text{trapped}} = 1025 \times 361.44 = 370{,}472\ \text{kg}$$

or, equivalently,

$$M_{\text{trapped}} \approx 370.5\ \text{t}$$

For modelling purposes, this value was rounded and entered in OrcaFlex as approximately:

$$M_{\text{trapped}} \approx 370\ \text{t}$$

in the vertical hydrodynamic mass term of the buoy "ExtraMassTrappedWater".

It is important to clarify the physical meaning of this modelling step. The buoy "ExtraMassTrappedWater" is introduced only to represent the inertial effect of the internal water column after submergence. It is not intended to introduce additional structural mass, additional hydrostatic volume, or additional drag loading. Those effects are already represented elsewhere in the model, primarily through the main spar buoy and the structural properties assigned to the SDU foundation.

For this reason, the buoy was configured to contribute only inertia. In practice, this was achieved by assigning:

- negligible geometric volume,
- hydrodynamic mass in Zequal to approximately 370 t,
- $C_a(z) = 1.0$,
- $C_m(z) = 0.0$,

while all remaining translational and rotational hydrodynamic coefficients were set to zero.

This choice ensures that the buoy does not create artificial buoyancy or drag forces. Instead, it acts purely as a lumped vertical inertia term that becomes active once the caisson top is submerged and the internal water is effectively carried with the structure.

From a physical point of view, this modelling assumption reflects the fact that the internal water column resists rapid changes in vertical motion. As a result, once the SDU enters the water and the upper cap passes below the free surface, the trapped water increases the system's effective vertical inertia. This can amplify the transient response during splash-zone crossing and influence both crane-cable tension and cable-angle behaviour.

3.4.3 Functional separation of the buoy objects

The use of three separate buoy objects in the OrcaFlex model is intentional and reflects that different parts of the SDU's hydrodynamic response are governed by distinct physical mechanisms.

The main spar buoy, denoted "SDU-FOUNDATION", represents the global geometry and hydrostatic behaviour of the subsea structure. It carries the principal structural mass, centre of gravity, rigid-body inertia, buoyancy variation, and the general drag response of the SDU foundation during lifting, splash-zone crossing, and lowering. In other words, this buoy is the main hydrodynamic representation of the foundation structure as a whole.

However, the main spar buoy alone is not sufficient to reproduce the two localised hydrodynamic effects that become important when the suction caisson cap approaches and passes through the free surface: the additional axial added mass generated at sea-surface crossing, and the inertia of the water trapped inside the caisson after the top cap has submerged. For this reason, two auxiliary buoy objects were introduced.

The first auxiliary buoy, "AxialAddedMassTopSeaSurface", represents the additional vertical added mass associated with free-surface crossing. Its purpose is to account for the increased resistance of the surrounding water to vertical motion when the upper cap of the caisson interacts with the sea surface. This buoy is therefore a local hydrodynamic correction for axial inertia and is not intended to represent the overall buoyancy of the structure.

The second auxiliary buoy, "ExtraMassTrappedWater", represents the vertical inertia of the internal water column once the cap has submerged and water has become trapped in the caisson cavity. This buoy likewise acts only as an inertial correction and does not represent additional hydrostatic volume or additional structural weight.

This functional separation is important because it avoids double-counting. The main spar buoy already reproduces the SDU's global displaced volume and hydrostatic response. If the auxiliary buoy objects were also allowed to contribute normal buoyancy in the same way, the model would artificially overestimate the hydrodynamic forces. By assigning the auxiliary buoys only the specific inertial functions required, the model preserves the correct global buoyancy while still capturing the local splash-zone physics.

Accordingly, the modelling roles of the three buoy objects may be summarised as follows: "SDU-FOUNDATION" represents the global structural and hydrostatic response of the SDU foundation; "AxialAddedMassTopSeaSurface" provides a local correction for the additional axial added mass at cap-entry/free-surface crossing; and "ExtraMassTrappedWater" provides a local correction for the inertia of the entrapped internal water after top-cap submergence. This modelling strategy provides a practical balance between physical realism and numerical simplicity. The overall SDU foundation response is governed by the main spar buoy, while the two auxiliary buoys are used only to introduce the specific splash-zone hydrodynamic effects that would otherwise be underrepresented.

3.5 Installation stages and model configuration

The analysed offshore operation was represented through two sequential numerical models. In the

first model, the SDU foundation was positioned on the cargo barge and lifted by the installation vessel. Both the installation vessel and the barge were included in the numerical model because their relative motions directly influence crane-cable tension, clearance behaviour, and contact response. In the second model, the barge was removed, and the installation vessel continued lowering the SDU foundation from the suspended condition to the seabed.

In the lift-off model, the first 300 s of simulation time were used for wave build-up. The SDU foundation then remained seated on the barge for 600 s under fully developed environmental loading. Thereafter, it was lifted 3 m above the deck and held in the air for an additional 600 s. In the lowering model, the SDU foundation was first held in the air after barge departure, then the outreach was reduced, the structure was lowered into the water, the tugger lines were released, and the SDU foundation was lowered to the seabed.

For interpretation and post-processing, the overall operation was reported in three operational windows: (i) Lifting Off the Deck; (ii) Splash Zone, from the time the bottom of the SDU foundation was 1 m above the sea surface until the top of the structure was 1 m below the surface; and (iii) Lowering, from that point until seabed landing.

4 Acceptance criteria and post-processing

Operability was assessed using the following criteria: crane-cable DAF ≤ 2.0; absolute off-lead angle $\leq 2.0°$, and absolute side-lead angle $\leq 2.0°$.

For each load case, the maximum response within the relevant time window was extracted and used to derive limiting sea-state tables and operability plots. Post-processing focused on crane-cable tension, DAF, off-lead angle, and side-lead angle for the Lifting Off the Deck, Splash Zone, and Lowering windows.

5 Results and discussion

5.1 Overall operability trends

The operability assessment shows a clear hierarchy among the three analysed installation stages. Figures 6–8 allow the limiting significant wave height to be compared directly as a function of wave direction and peak period for the three principal operational windows: Lifting Off the Deck, Splash Zone, and Lowering. The splash-zone phase governs the overall operation, the lift-off phase is a secondary but still sensitive stage, and the fully submerged lowering stage is less restrictive overall.

A consistent pattern is visible across Figures 6–8. For both lift-off and fully submerged lowering, the DAF-based envelopes are comparatively permissive and, in many regions, reach the upper screened limit of $H = 2.0$ m, whereas the off-lead and side-lead criteria impose the main restrictions. In the splash zone, by contrast, the weather window narrows because short-period cases are already limited by DAF, and a broad band of intermediate periods is further constrained by the lead-angle response. The governing weather window is therefore defined by the combined action of free-surface-entry hydrodynamics and crane-wire angular demand rather than by dynamic amplification alone.

5.2 Lifting off the deck

The lift-off-stage operability results are summarised in Figure 6. Figure 6(a) presents the crane-cable dynamic amplification factor (DAF), Figure 6(b) presents the absolute off-lead angle, and Figure 6(c) presents the absolute side-lead angle. The DAF plot is comparatively permissive: for most headings and periods, the limiting sea state remains in the range of about 1.5–2.0 m, and many cases reach the upper screened limit of 2.0 m. Only local reductions are observed, mainly around intermediate periods near 8–10 s.

The angle-based criteria are more restrictive. Figures 6(b) and 6(c) show that both off-lead and side-lead reduce the allowable H over several oblique headings, particularly around intermediate periods near 10–12 s, where some cases fall below 1.0 m, and isolated cells fail even at the minimum screened sea state. The off-lead response is slightly more restrictive than the side-lead response in several sectors, but both criteria are materially tighter than the DAF criterion. These results show that lift-off is operationally important and requires careful planning, yet it does not define the narrowest overall weather window for the analysed SDU foundation installation.

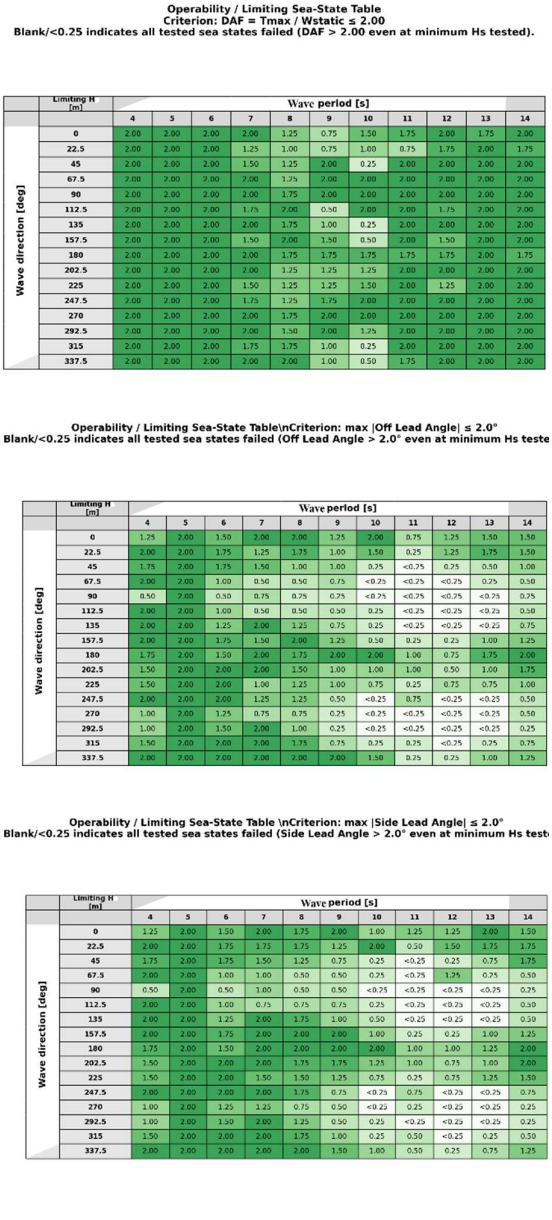

Figure 6- Operability plots for Lifting Off the Deck: (a) crane-cable dynamic amplification factor (DAF), with an acceptance limit of DAF ≤ 2.0; (b) absolute off-lead angle, with an acceptance limit of |off-lead| ≤ 2.0°; (c) absolute side-lead angle, with an acceptance limit of |side-lead| ≤ 2.0°.

5.3 Splash-zone response

The splash-zone operability results are presented in Figure 7. Figure 7(a) presents the crane-cable dynamic amplification factor (DAF), Figure 7(b) presents the absolute off-lead angle, and Figure 7(c) presents the absolute side-lead angle. The splash-zone phase is the governing stage of the operation.

Figure 7(a) shows that DAF is already restrictive at short periods. At $T = 4–5$ *s*, the limiting sea state is commonly only about 0.25–0.75 *m*, and the DAF window broadens only gradually as the period increases. Figures 7(b) and 7(c) show that the lead-angle criteria impose additional restrictions across a broader intermediate-period band, especially around $T = 9–11$ *s*, where many headings are limited to about 0.25–1.0 *m* and several cells approach failure at the minimum screened sea state. Off-lead and side-lead, therefore, remain critical even where the DAF window has partially recovered.

The key point is that the splash-zone phase governs not because it produces the largest DAF everywhere, but because it yields the narrowest combined operability envelope when all criteria are considered together. This behaviour is fully consistent with the adopted hydrodynamic model, in which sea-surface crossing activates both the additional axial added-mass term represented by the AxialAddedMassTopSeaSurface buoy and the entrapped-water inertia represented by the ExtraMassTrappedWater buoy. Accordingly, the splash-zone phase is governed by free-surface-entry hydrodynamics rather than by simple hook-load amplification. This is a defining characteristic of suction-caisson-type structures and is central to understanding why the SDU foundation suction caisson differs from more open-frame subsea structures.

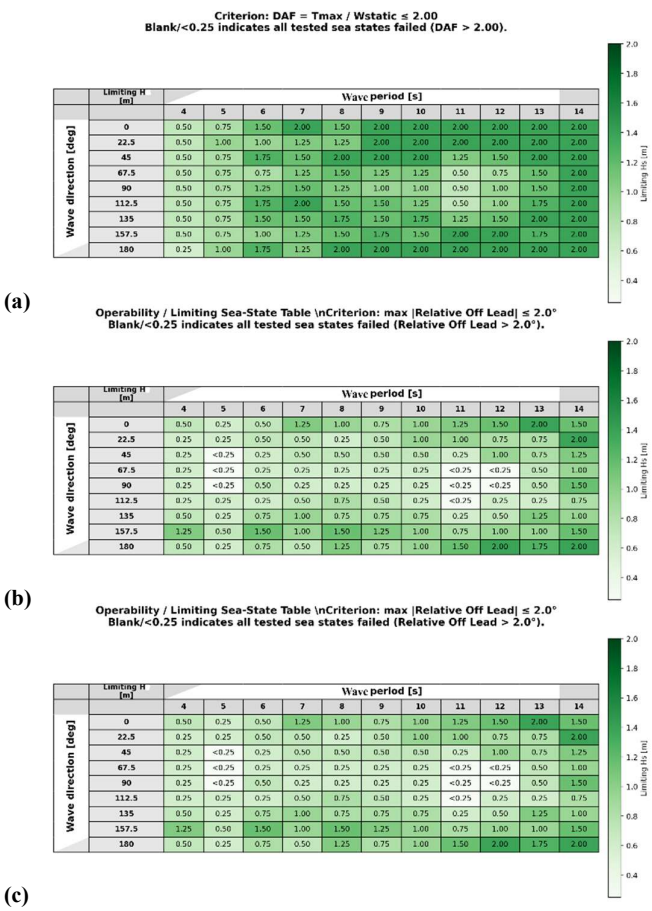

Figure 7- Operability plots for Splash Zone: (a) crane-cable dynamic amplification factor (DAF), with an acceptance limit of DAF ≤ 2.0; (b) absolute off-lead angle, with an acceptance limit of |off-lead| ≤ 2.0°; (c) absolute side-lead angle, with an acceptance limit of |side-lead| ≤ 2.0°.

5.4 Lowering below the splash zone

The operability results for the lowering stage are shown in Figure 8. Figure 8(a) presents the crane-cable dynamic amplification factor (DAF), Figure 8(b) presents the absolute off-lead angle, and Figure 8(c) presents the absolute side-lead angle. Once the SDU foundation is fully submerged, the response becomes more stable overall than in the splash zone.

Figure 8(a) shows that the DAF window broadens again after full submergence. For much of the investigated period range, especially from about 6 s upward, the limiting sea state is between about 1.5 and 2.0 m, and many cases reach the upper screened limit of 2.0 m. Figures 8(b) and 8(c) indicate that off-lead and side-lead still constrain selected combinations of period and heading, particularly around intermediate periods, but the most restrictive regions are less extensive than in the splash zone, and long-period conditions are generally more operable. The lowering response, therefore, remains angle-sensitive in some sectors, yet it does not define the governing weather window.

These results indicate that once the SDU foundation is fully submerged, the transient free-surface-crossing mechanisms become less important and hydrodynamic damping becomes more effective. The lowering phase is therefore more stable and more operable overall than the splash-zone phase.

Criterion: DAF = Tmax / Wstatic ≤ 2.00
Blank/<0.25 indicates all tested sea states failed (DAF > 2.00).

Wave direction [deg]	Limiting H [m]	Wave period [s]										
		4	5	6	7	8	9	10	11	12	13	14
	0	0.75	1.75	2.00	2.00	2.00	2.00	2.00	2.00	2.00	2.00	2.00
	22.5	1.25	1.75	2.00	2.00	1.75	2.00	2.00	2.00	2.00	2.00	2.00
	45	1.50	2.00	2.00	2.00	2.00	2.00	1.75	0.75	1.00	2.00	2.00
	67.5	0.75	1.75	2.00	1.75	1.50	1.50	1.00	0.25	0.50	1.50	2.00
	90	1.50	1.50	2.00	1.25	2.00	1.75	1.00	0.25	0.25	1.25	2.00
	112.5	1.25	2.00	2.00	1.50	1.75	1.75	1.75	0.25	0.50	1.50	2.00
	135	1.00	2.00	2.00	2.00	2.00	1.75	2.00	1.50	0.75	2.00	2.00
	157.5	1.25	2.00	2.00	2.00	2.00	2.00	2.00	2.00	1.50	1.75	2.00
	180	1.25	1.75	2.00	2.00	2.00	2.00	2.00	2.00	2.00	2.00	2.00

(a)

Operability / Limiting Sea-State Table \nCriterion: max |Off Lead Angle| ≤ 2.0°
Blank/<0.25 indicates all tested sea states failed (Off Lead Angle > 2.0°).

Wave direction [deg]	Limiting H [m]	Wave period [s]										
		4	5	6	7	8	9	10	11	12	13	14
	0	1.75	2.00	2.00	1.75	1.00	0.75	0.75	1.25	2.00	2.00	2.00
	22.5	1.25	1.25	0.75	0.75	0.75	0.50	0.50	1.50	2.00	2.00	2.00
	45	2.00	0.75	0.50	0.75	0.50	0.50	0.50	0.25	1.25	2.00	2.00
	67.5	1.25	0.50	0.50	0.50	0.50	0.50	0.25	<0.25	0.50	1.25	2.00
	90	1.50	0.50	0.75	0.50	0.50	0.25	0.25	<0.25	0.25	0.75	1.75
	112.5	1.25	1.00	0.50	0.75	1.00	0.50	0.25	<0.25	0.50	1.00	1.50
	135	1.25	1.50	1.00	2.00	0.75	1.00	0.25	0.75	0.75	2.00	1.75
	157.5	1.25	1.50	2.00	2.00	2.00	1.25	0.75	0.75	2.00	1.75	2.00
	180	1.50	1.25	2.00	1.75	2.00	1.00	1.00	1.25	2.00	2.00	2.00

(b)

Operability / Limiting Sea-State Table\nCriterion: max |Side Lead Angle| ≤ 2.0°
Blank/<0.25 indicates all tested sea states failed (Side Lead Angle > 2.0°).

Wave direction [deg]	Limiting H [m]	Wave period [s]										
		4	5	6	7	8	9	10	11	12	13	14
	0	1.75	1.50	0.50	1.00	0.50	0.25	0.50	1.25	2.00	2.00	2.00
	22.5	1.25	2.00	1.00	0.75	0.50	0.75	0.75	1.50	2.00	2.00	2.00
	45	2.00	1.25	1.75	2.00	2.00	1.00	0.75	0.25	1.25	2.00	2.00
	67.5	1.50	1.50	2.00	1.50	0.50	1.00	0.25	<0.25	0.75	1.50	2.00
	90	1.75	1.25	2.00	0.75	1.50	1.25	0.50	<0.25	0.25	1.25	2.00
	112.5	1.25	1.00	1.75	1.25	0.50	0.25	0.25	<0.25	0.50	1.00	2.00
	135	1.25	1.50	0.50	0.50	0.50	0.25	0.25	0.50	1.00	1.75	2.00
	157.5	1.25	0.50	0.50	0.50	0.50	0.25	0.25	1.00	1.50	1.75	2.00
	180	1.50	1.25	0.75	0.50	0.50	0.50	0.50	1.00	2.00	2.00	2.00

(c)

Figure 8- Operability plots for Lowering: (a) crane-cable dynamic amplification factor (DAF), with an acceptance limit of DAF ≤ 2.0; (b) absolute off-lead angle, with an acceptance limit of |off-lead| ≤ 2.0°; (c) absolute side-lead angle, with an acceptance limit of |side-lead| ≤ 2.0°.

5.5 Case study on the influence of axial added mass and entrapped-water modelling

To illustrate the effect of the auxiliary hydrodynamic buoys on the predicted lowering response, a dedicated case study was conducted under a single regular-wave condition with a wave direction of 0°, a significant wave height H = 0.5 m, and a peak period T = 6 s. The objective of this comparison was to isolate the influence of the two local hydrodynamic corrections introduced at sea-surface crossing, namely the entrapped-water buoy and the axial-added-mass buoy.

Three model variants were considered: (i) a base hollow-body model in which the lowering simulation was run without the two auxiliary buoys representing axial added mass and entrapped-water inertia; (ii) an entrapped-water model in which the lowering simulation was repeated with the ExtraMassTrappedWater buoy activated while the axial-added-mass buoy remained inactive; and (iii) a full sea-surface-crossing model in which the lowering simulation was run with both auxiliary buoys activated, namely ExtraMassTrappedWater and AxialAddedMassTopSeaSurface.

The comparison was based on crane-cable tension and crane-cable declination during the lowering stage. This case study was introduced to show how progressively refining the hydrodynamic idealisation affects the predicted response as the

SDU foundation passes through the free-surface and continues into the submerged-lowering stage. In this way, the relative contribution of entrapped-water inertia alone can be distinguished from the combined effect of entrapped-water inertia and the additional axial added mass that develops when the upper cap crosses the sea surface.

Figure 9 compares the crane-cable tension and crane-cable declination time histories for the three modelling cases. The base model without the two auxiliary buoys shows only a modest transient response when the structure crosses the free surface. The effective tension decreases smoothly from the pre-entry level and then settles at a lower post-entry level with comparatively limited oscillation. When the entrapped-water buoy is activated, a markedly stronger transient develops at about t = 1900 s, with a clear tension overshoot followed by a decaying oscillatory response. When both the entrapped-water buoy and the axial-added-mass buoy are activated, the transient becomes strongest, and the post-entry oscillations persist for the longest duration.

The difference is particularly clear in the tension histories. Over the interval 0–3000 s, the base model varies between approximately 572 and 680 kN. With only the entrapped-water buoy, the peak tension increases to about 779 kN, and the minimum drops to about 486 kN. With both auxiliary buoys activated, the peak rises further to about 907 kN, and the minimum decreases to about 419 kN. The declination histories remain close to 180° in all three cases, but the post-entry oscillations become denser and more persistent when the auxiliary buoy modelling is activated, especially in the full model with both buoy corrections. The case study, therefore, shows that the inclusion of entrapped-water inertia and axial added mass most strongly affects the lowering response through transient fluctuations in crane-cable tension associated with sea-surface crossing.

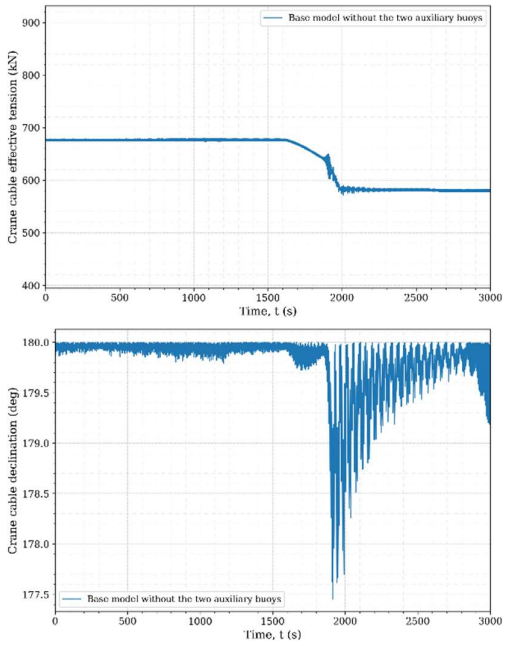

(a)

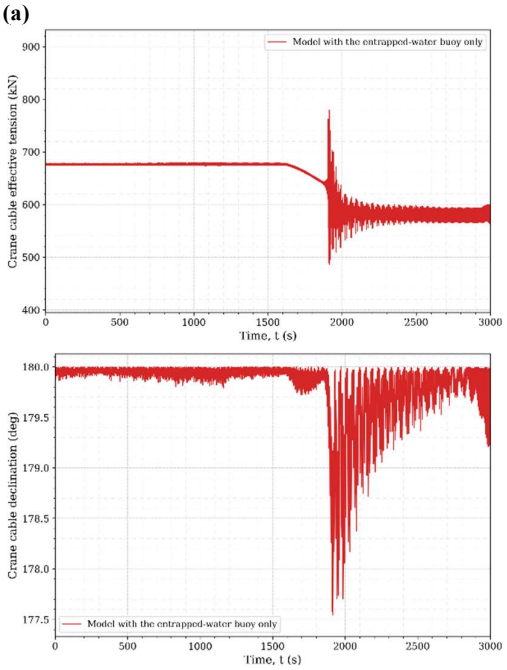

(b)

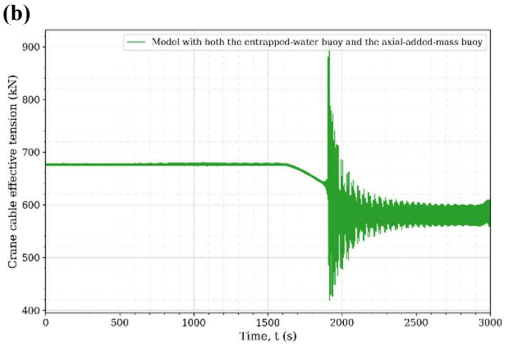

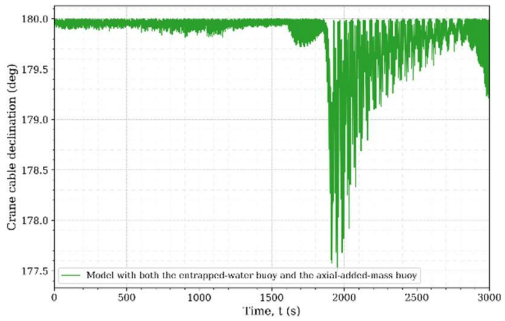

(c)

Figure 9- Case-study comparison of crane-cable response during lowering for wave direction 0°, H = 0.5 m, and T = 6 s, for (a) the base model without the two auxiliary buoys, (b) the model with the entrapped-water buoy only, and (c) the model with both the entrapped-water buoy and the axial-added-mass buoy. The figure includes both crane-cable tension and crane-cable declination time histories for the three modelling cases.

This case-study comparison provides a direct numerical demonstration of the modelling philosophy adopted in the present paper. The base hollow-body representation captures the global lowering behaviour of the SDU foundation, but it cannot fully reproduce the local hydrodynamic inertia effects associated with top-cap submergence. Adding the entrapped-water buoy introduces the inertia of the internal water column after submergence, whereas activating both auxiliary buoys provides the most complete representation of the free-surface-crossing physics used in the present study. The resulting increase in transient crane-cable tension and the longer decay of post-entry oscillations provide a practical measure of the importance of these modelling refinements in SDU foundation lowering analysis.

5.6 Comparative interpretation with PLET-type structures

The present SDU suction caisson foundation results are particularly instructive when compared with previously analysed open-frame subsea structures, such as Pipe Line End Terminal (PLET) foundations. In PLET-type structures, the governing installation stage may occur during lift-off from the barge, where the coupled vessel–wire–payload response in air produces the strongest restrictions. In the present SDU foundation case, however, the governing stage shifts to splash-zone entry.

This contrast shows that the governing installation stage is not universal but depends on structural topology and hydrodynamic mechanism. Open-frame structures are more strongly controlled by pre-submergence lifting dynamics, whereas suction-caisson-type structures may be governed by sea-surface crossing because the geometry activates additional axial added mass and entrapped-water inertia. Installation operability is therefore structure-dependent and cannot be generalised across subsea asset types.

6. Conclusions

A comprehensive time-domain OrcaFlex analysis was carried out to assess the operability of installing an SDU foundation lifted by a vessel from a cargo barge, lowered through the splash zone, and landed on the seabed at 154 m water depth. The study combined staged operational modelling, imported vessel-motion RAOs, and a hydrodynamic idealisation of the SDU foundation that explicitly represented the additional axial added mass and entrapped-water inertia associated with top-cap sea-surface crossing.

The results establish a clear hierarchy among the analysed installation stages. Lift-off is sensitive, but its DAF-based operability remains comparatively permissive; the main restrictions arise from off-lead and side-lead angles at selected headings and during intermediate periods. The splash-zone phase governs the overall operation and defines the narrowest operability envelope, as short-period cases are already limited by DAF, whereas a broader intermediate-period band is constrained by the angular response. After full submergence, the DAF window broadens again, and the lowering phase becomes more operable overall, although selected angle-governed combinations remain restrictive.

The case study confirms the physical importance of the auxiliary buoy modelling. Relative to the base model without the two auxiliary buoys, activating the entrapped-water buoy increases the peak crane-cable tension from about 680 kN to 779 kN, while activating both the entrapped-water buoy and the axial-added-mass buoy raises it to about 907 kN and produces the longest post-entry oscillations. The declination response remains close to 180° in all cases, but the persistence of the post-entry oscillations increases when the auxiliary hydrodynamic corrections are activated. The governing response is therefore controlled not simply by mean load level, but by the transient

amplification generated when the caisson cap crosses the water surface.

The present study, therefore, shows that the governing installation stage is geometry-dependent. For the analysed SDU suction caisson foundation, splash-zone entry governs operability. This contrasts with more open-frame subsea structures, for which the most restrictive response may occur during pre-submergence lift-off. Accordingly, installation operability should not be generalised across structure types without accounting for the underlying hydrodynamic mechanism.

The developed methodology and resulting operability envelopes provide a practical basis for offshore planning, weather window definition, and phase-specific execution control for SDU foundation installation. The analysis also offers a useful framework for future comparative studies of subsea lifting operations involving different structural topologies and different governing hydrodynamic mechanisms.

7. References

1. de Andrade EM, Barral M, Cueva M, Fernandes AC. A review on the modeling of subsea lifting operations. Ocean Eng. 2023;271:113680.
2. Jia D, Agrawal M. Fluid-structure interaction: lowering subsea structure/equipment in splash zone during installation. In: Proceedings of the Offshore Technology Conference; 2014; Houston, TX. Houston (TX): Offshore Technology Conference; 2014.
3. Li Y, Zhao H, Xu N, et al. Study of the installation process of the subsea tree passed through the splash zone. Energies. 2020;13(5):1014.
4. Amer AM, Metrikine A, Gao Z. Dynamic analysis of splash-zone crossing operation for a subsea template. Sustain Mar Struct. 2022;4(2):19-40.
5. Gordon RB, Grytoyr G, Dhaigude M. Modeling suction pile lowering through the splash zone. In: Proceedings of the ASME 32nd International Conference on Ocean, Offshore and Arctic Engineering (OMAE2013); 2013; Nantes, France. New York (NY): ASME; 2013.
6. Yasseri SF, Bahai H. Availability assessment of subsea distribution systems at the architectural level. Ocean Eng. 2018;153:399-411.
7. Orcina Ltd. OrcaFlex. Version 11.6b [computer software]. Ulverston (UK): Orcina Ltd.
8. DNV-RP-C205: Environmental conditions and environmental loads. Recommended practice. Høvik (Norway): DNV.
9. DNV-RP-N103: Modelling and analysis of marine operations. Recommended practice. Høvik (Norway): DNV; 2017. Amended 2021.
10. Orcina Ltd. F07 suction anchor lowering. OrcaFlex example documentation. Ulverston (UK): Orcina Ltd. Available from Orcina example files/documentation.

INTERNATIONAL JOURNAL OF
COASTAL, OFFSHORE & ENVIRONMENTAL ENGINEERING IJCOE Vol.11/No. 2/Spring 2026 (26-37)

Available online at: www. Ijcoe.org

Investigation of microplastics and heavy metals contamination in southwestern Caspian Sea Gammarus

Sara Emami[1], Mohammad Reza Rezaei[2*], Mohammad Hossein Sayadi[3]

[1] Graduated Student, Department of Environmental Engineering, Faculty of Natural Resources and Environment, University of Birjand, Birjand, Iran; saraemami7545@yahoo.com
[2] Associate professor, Department of Environmental Engineering, Faculty of Natural Resources and Environment, University of Birjand, Birjand, Iran; mrrezaei@birjand.ac.ir*
[3] Associate professor, Faculty of Natural Resources and Environment, Shahid Bahonar University of Kerman, Kerman, Iran; mh_sayadi@uk.ac.ir.*

ARTICLE INFO

Article History:
Received 10 Sep2025
Accepted 30 Dec2025

Keywords:
Gilan province
Microplastic polymers
Copper
Chromium
Public waste

ABSTRACT

Plastic is considered the main component of waste and sometimes accumulates on beaches. The studied stations are located in the coastal areas, approximately 35 km long in the Caspian Sea in Gilan province, Iran. This study aims to quantitatively and qualitatively investigate the presence of microplastics and their combined impact with heavy metals in the environment (water and sediment) as well as in aquatic organisms (specifically Gammarus) within the southwestern area of the Caspian Sea. The results of this research have shown that the highest average concentration of microplastics was found in the water environment samples from the 4th station (13400±658 pieces per liter), while the lowest average concentrations were recorded in the first and fifth stations (5200±370) and (5600±357) pieces per liter, respectively. Microplastics in the form of purple fragments in the size of 0.5 to 1 mm with a magnification of 40 are the most abundant. Heavy metals, notably copper and chromium, have been identified in Gammarus specimens. Additionally, polymers were detected in both water and Gammarus samples, potentially originating from fishing nets and general waste in the area. The presence of microplastics in study stations has increased the concentration of heavy metals in Gammarus and the water environment. The ANOVA test also showed that there is a direct and significant relationship at the 1% level between the concentration of heavy metals and microplastics. These results indicate the mutual and important synergistic effects between microplastics and heavy metals on the marine environment of the Caspian region.

1. Introduction

As population growth, urbanization, and society's well-being, increase environmental concerns, health, and hygiene has become more prominent. The recent growth of industrial activities and non-compliance with environmental requirements resulted in the entry of a significant volume of emerging pollutants, including plastic and pharmaceuticals, into the environment [1]. Their stabilization and bioaccumulation properties make these pollutants a significant danger. Plastics are responsible for the majority of waste in water and marine environments. The problems related to microplastics in water are of global concern cause for aquatic animals through ingestion. In addition, microplastics, which are carriers of heavy metals and organic substances, are strengthened when they enter the food chain and can have unpredictable effects on aquatic life and humans [2,3]. Types of plastics are macroplastics, microplastics and nanoplastics. Macroplastics are particles larger than 5 mm. Microplastics are small particles that are less than 5 millimeters in size, and they are usually made by degradation of plastics in the marine environment by ultraviolet rays and wave power. Nanoplastics are a subgroup of microplastics that have a nanometer size range, usually less than 1 micron in diameter. These nanoparticles can come from a variety of sources, including microplastics that have been broken down into smaller particles, nanoplastic fibers released from synthetic textiles, or intentionally engineered nanoparticles that are used in products such as personal care items or as additives in industrial processes [4].

Microplastics are classified into primary and secondary groups. The primary type of products is designed to be used for commercial, transportation, medical, pharmaceutical, cosmetics, paint, and agricultural purposes. Secondary microplastics are produced when macroplastics break down during continuous weathering and sunlight in marine environments, and they come in many sizes, shapes, colors, and polymer types [5]. Various types of plastic pollution in the seas and oceans have been extensively studied in the past few years, when plastic pollution was negligible until the 1970s [6]. Marine animals are affected by microplastics' small size and high dispersion as they enter their food chain [2]. Every year, thousands of aquatic animals, such as whales, dolphins, turtles, and sea birds, are suffocated [7]. Fish, birds, and marine mammals have experienced negative effects such as inflammation, decreased energy reserves, and decreased feeding after ingestion of microplastics [8]. Gammarus is used as a sample for studying marine water pollution due to its high sensitivity to chemical and physical changes in the environment, its widespread presence in various marine and freshwater habitats, its important role in the marine food chain, and its ease of collection and study [9]. These organisms act as effective bioindicators because of their ability to accumulate various pollutants, including heavy metals and microplastics, and their impacts on other marine species [10]. Additionally, the research background on Gammarus allows researchers to compare and analyze their findings with previous studies, making them a valuable tool for assessing the health of marine ecosystems [11, 12]. In the aquatic environment, microplastics, which are considered an inert carbon flux, are known to carry heavy metals and have diverse interactions [13, 14]. However, these interactions, particularly the mechanisms that drive them, pose risks to living organisms. Heavy metals have a variety of effects on living organisms, such as chromium, which is believed to be carcinogenic and toxic to aquatic organisms, animals, and humans. Pollutants entering aquatic environments are mostly deposited by various flows, such as surface runoff, wastewater treatment plants, and storms . The high population density in the southwestern parts of the Caspian Sea in Gilan province (Talesh coast) has resulted in harm to marine organisms. Microplastic particles, which are small and have a similarity to natural food, are intentionally or accidentally swallowed by a fish. Since fish is a protein source for humans, this contamination is a result of toxicological effects. The safety of seafood can be compromised by microplastics [16]. The impact of sea pollutants on endocrine glands can be disruptive, and microplastic surfaces can carry harmful compounds. Toxic effects affect marine organisms at different nutritional levels when accumulated in biological tissues. Immune and reproductive responses are just some of the effects that vary depending on the sensitivity of species and ocean currents, as well as the overlap of marine organisms [17]. Consumption of some heavy metals such as zinc and copper in low doses is beneficial for the physiological functions of the human body [18]. According to the European Union, the maximum tolerance of lead, cadmium and mercury metals in edible fish tissue is 0.3, 0.05-0.30 and 1.00-0.5 mg/kg [19]. However, toxic heavy metals at high doses harm the diversity of Gammarus and ecosystems, as well as ultimately harm human health by transferring through the food chain [20,11,12]. Studying the interactions between heavy metals and microplastics in Gammarus of the Caspian Sea is crucial because these organisms play a key role in the marine food chain and act as sensitive bioindicators of environmental changes. Gammarus can accumulate various pollutants, including heavy metals and microplastics, in their bodies, and examining these accumulations can reveal how these pollutants simultaneously affect marine life. Understanding the combined effects of these pollutants on Gammarus can aid in developing strategies for pollution management and reduction, help protect biodiversity in the Caspian Sea, and safeguard human health. Therefore, the aim of this research is investigated the quantitatively and qualitatively microplastics and the synergistic effect with heavy metals in the environment (water and sediment) and Gammarus of the southwestern Caspian Sea.

2. Materials and methods

2.1. Study area and sampling stations

In the winter of 2023, the samples of Gammarus and the surrounding environment of Gammarus (water and sediment which is sandy) from 5 stations of the southwestern shores of the Caspian Sea were taken. The sites selection was according to different land uses 1- landfill station (37° 50' 30.30"N; 48° 58' 17.00"E) 2- Gisoom recreational beach area (37°40' 53.30"N; 49° 2' 48.70"E) 3- Before the power plant (37° 39' 26.70" N; 49° 4' 24.50" E) 4- Surroundings of the Paresar power plant (37° 38' 25.40" N; 49° 5' 44.70"E) 5-The Shafarood River (37° 35' 39.90"N; 49° 9' 41.00"E), respectively. The location of the sampling stations is shown in Figure 1.

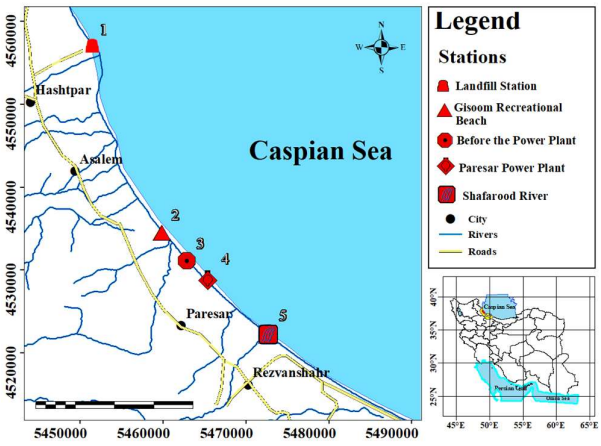

Figure 1. Location map of the sampling stations

The studied stations have been selected based on field observations and land use as the possible source of pollution. The station number one is considered a source of pollution due to the large amount of leachate emitted from landfill site due to the slope of the area towards the Caspian Sea. In addition, due to the winds direct that pass over this place, it causes pollution to be transferred through the air to the sea. The pollutants in these places are plastics in different sizes and categories, and heavy metals (such as copper, lead, cadmium, and zinc) [21, 22]. In the stations number 2 and 5 in the Gisoom area and around the Shafarood river, due to the lack of sufficient legal regulations, improper collection of garbage and its long-term accumulation in the place and its distribution due to the wind, in addition to the lack of educational activities and increasing the awareness of travelers to collect garbage causes to be a source of the pollution. The lack of appropriate forces to collect garbage from certain places on time has led to an increase in pollution in these areas. By swimming in seawater and public showers in coastal areas, cosmetics like sunscreens that contain microplastics are transported to the sea. The quantity of smoking on beaches is significant. Even though cigarette butts are considered normal waste, they are considered dangerous waste due to their exposure to various pollutants [23,24]. According to a research, cigarettes contain a considerable concentration of lead, cadmium, chromium, zinc, copper, and nickel. The long persistence of cigarette butts in the environment leads to an increase in the release of heavy metals, which is considered a source of beach pollution [25]. Station number 3 is located prior to the power plant while station number 4 is situated next to it. It has been proven in many studies that power plants introduce different types of heavy metals into the environment based on their type. The health of living organisms can be significantly impacted by the contamination of heavy metals in groundwater by power plants [26]. According to this study, the seasonal concentration of heavy metals was higher for aluminum, arsenic, lead, iron and manganese exceeded acceptable levels of national and international agencies and even exceeded US standards, affecting the pediatric population more than adults. In addition, high levels of toxic metals were observed during the post-monsoon season, although human activities are not without influence on the amount of these pollutants [27].

2.2. Collection of Gammarus and surrounding environment samples and digestion to measure heavy metals

Gammaros samples were collected from beach sand using a 1.180 mm sieve and 16 meshes, with 5 repetitions for each studied station. The number of Gammarus in each half-hour attempt at each station was recorded as 58, 125, 26, 32, and 16 cases in the stations, respectively. After initial washing with seawater, the samples were moved from the sieve into special containers, and then the containers containing the samples were placed in ice pack and transported to the laboratory [23]. After ensuring the identification of the species [28], the samples were first washed with distilled water and then about 15 g of Gammarus were placed at 105°C for 24 hours to dry. After evaluating the dry weight based on reaching a constant weight, the samples were pounded in a mortar and homogenized. In the next step, 1g of each sample was weighed using a digital scale with an accuracy of 0.0001g and 10 mL of concentrated nitric acid along with 2 mL of hydrogen peroxide were added to it. Then the samples were placed on the digestion reactor for acid digestion for 3 hours at a temperature of 95 degrees Celsius and then the digestion solution was filtered through a 0.45 m nitrocellulose filter and prepared for heavy metals reading [29]. After filtering, the samples of the environment around the gammarus were poured into 15 mL beakers with station labels. Then, five milliliters of concentrated nitric acid (HNO_3, Merck, Germany) was added and each sample was placed on a sand bath at 150°C for 4 to 5 hours or until they were slowly digested. After cooling with deionized water, the samples were brought to a volume of 10 mL, then filtered through 0.45 µm filter paper (nitrocellulose). The concentration of heavy metals in the tissue of gammarus and the surrounding environment of gammarus was measured with a graphite furnace atomic absorption device (ContrAA 700, Analytik Jena AG, Germany).

2.3. Identify Gammarus species in the study area

Gammarus refers to a genus of small shrimp-like crustaceans commonly found in freshwater environments such as rivers, lakes, and streams. These organisms, also known as amphipods or freshwater shrimp, are integral components of aquatic ecosystems, serving as both herbivores and insectivores. They play a crucial role in the food web by consuming algae, plant matter, and decaying organic material, thereby providing a food source for various aquatic predators.

At each station, three samples were collected using a dredge sampler, fixed in 5% formalin, and transferred to the laboratory. Several keys to the Gammarus were used to identify these species [30, 31] to the species level. After laboratory operations, four species of Gammarus are present, including *Gammarus lacustris, Gammarus duebeni, Gammarus tigrinus,* and *Gammarus pulex*. These species contribute significantly to the ecosystem as scavengers, aiding in the recycling of nutrients by feeding on organic matter. They are also important prey for numerous fish and invertebrates, and their abundance and diversity serve as indicators of the Caspian Sea's ecosystem health.

2.4. Determining the presence and type of microplastics in the tissue of Gammarus

The collected Gammarus were washed with distilled water and dried on a heater at a temperature of 50 degrees Celsius and ground in a mortar. In order to determine the presence and type of microplastics, 0.05 grams of each powdered sample was separated and used for micro FTIR analysis. For quick and direct identification of plastic polymers, it was achieved by comparing the resulting spectra with existing reference spectra [11].

2.5. Determining the frequency, shape, color, size and type of microplastics in the environment around Gammarus

The samples were taken from five study stations with five points per station, and then mixed to create a composite sample for each station. The resulting samples were sieved through a stainless steel sieve and stored in glass bottles. Then 100 mL of it was mixed with 10 mL of H2O2 at room temperature for 48 hours. The samples were subjected to a glass microfiber filter (1.2 mm) after being passed through it. An optical microscope, such as the Olympus BX41, was used to determine the amount, pattern, hue, and size of microplastics. To count microplastics in seawater, 5 mL of water sample collected from the beach was checked as one drop on a slide by repeating 5 drops under a microscope with 40x magnification and the number, color, shape and size of microplastics were recorded. To ensure that the glass bottles are free of microplastics, a control sample was run alongside the studied samples.

2.6. Determination of salinity, pH and temperature of the studied stations

Before implementing the laboratory protocols in sampling, the physico-chemical characteristics of the water environment and the habitat of the Gammarus were measured. pH values range from 7.20 to 7.66 (mean 7.42± 0.278), with electrical conductivity (EC) ranging from 13.51 to 19.12 mS/cm (mean 16.61± 3.13), and temperature ranges from 10 to 15ºC (average 12.5± 3.53).

2.7. Statistical analysis

SPSS version 23 software was used for data analysis and the Shapiro-Wilk test was used to check the normality of the data. Also, Excel software was used to perform the necessary calculations and draw graphs. In this research, in order to investigate the effects of different uses as well as the synergistic effects of microplastics with heavy metals were studied. The existence of a significant difference in the level of 1% concentration of heavy metals and microplastics between Gammarus samples and water environment in different stations. One-way ANOVA analysis of variance LSD test was used.

3. Results and discussion

In this study, 25 water samples were collected in the 100mL bottles, with 5 repetitions conducted at 5 stations. Given that most of these stations are directly exposed to various pollutants, the results showed varying levels of microplastics and heavy metals (Tables 1 and 2).

The highest average number of microplastics was found in the water environment samples from the 4th station (13400±658 pieces per liter), while the lowest average concentrations were recorded in the first and fifth stations (5200±370) and (5600±357) pieces per liter, respectively. The highest average abundance of Gammarus (measured over half an hour) was observed at the 2nd station with 125 individuals, while the lowest frequency was recorded at the 5th station with 16 individuals (Table ١).

In the water, the highest concentration of copper was observed at the first station, measuring 0.0088 mg/L, while in Gammarus specimens, the fourth station showed the highest concentration at 0.589 mg/kg. Conversely, the lowest copper concentration in water was recorded at the fourth station, measuring 0.0017 mg/L, while in Gammarus, the lowest concentration was observed at the first station, measuring 0.3747 mg/kg. Regarding chromium, the highest concentration in water was detected at the fifth station, observing 0.0897 mg/L, whereas in Gammarus, the fourth station exhibited the highest concentration at 0.233 mg/kg. Conversely, the lowest chromium concentration in water was found at the fourth station, measuring 0.839 mg/L, while in Gammarus, the third station showed the lowest concentration at 0.1113 mg/kg. In terms of lead, the highest concentration in water was recorded at the fifth station, measuring 0.1476 mg/L, while in Gammarus, the second station exhibited the highest concentration at 0.1459 mg/kg. Conversely, the lowest lead concentration in water was observed at the fourth station, measuring 0.022 mg/L, while in Gammarus, the third station showed the lowest concentration at 0.0604 mg/kg(Table 2) .

This distribution pattern indicates that Gammarus populations are likely influenced by both the availability of suitable habitats and the levels of

Table ١: Frequency of counted microplastics and average abundance of Gammarus separately for each station in the study area

Stations	1	2	3	4	5
Microplastics in Water samples (pieces per liter)	5200±370	11000 ±458	9400±482	13400±658	5600±357
Average numbers of Gammarus	58±9	125±16	26±5	32± 5	16±3

pollution, with higher pollution levels potentially reducing their abundance [32, 33].

The results of statistical analysis between salinity, pH and temperature of the studied stations and heavy metal concentration and microplastics studied parameters showed that there is no significant difference between them (Pvalue≥0.05). The statistical analysis shows that there is a significant difference in the concentration of heavy metals in all stations between Water and Gammarus samples at the level of 1%. In addition, the ANOVA test showed that there is a positive and significant relationship at the 1% level between the abundance of microplastics and the mean concentration of heavy metals (Cu, Cr and Pb) in Gammarus. Therefore, it could be concluded that microplastics act as carriers of heavy metals and cause more accumulation of heavy metals. It can act as a carrier of heavy metals and cause more accumulation of heavy metals in the environments where they are present [14, 35]. Following a thorough analysis, it was determined that the uptake of heavy metals by naturally-aged microplastics primarily depended on the presence of oxygen-containing functional groups, such as carboxyl and hydroxyl groups, present on the organic film. Additionally, the assessment of Zeta potential and pH effects indicated that electrostatic interactions predominantly governed the process of heavy metal uptake [36, 37].

The highest frequency recorded according to the color of the particles in water samples is related to purple, followed by green, and the lowest value is related to blue and red, which was seen in 1% of all stations (Figure 2). The color of microplastics will have an effect on their properties, so that Chen and colleagues investigated the effects of four colored microplastics (MPs) on Scenedesmus obliquus algal growth and Daphnia magna feeding ability. Initially, algal growth increased due to hormesis stimulation, followed by a decrease at higher MP concentrations [34]. Green MPs showed the lowest inhibition effect, resembling algae, while white MPs significantly inhibited growth, likely due to ethanol presence. Turbulence reduced growth differences but induced slight oxidative stress. Daphnids seemingly couldn't distinguish colored MPs from algae, but ingestion increased when MPs reached 40% of algal cells, possibly due to widened filtering gapes. However, agglomeration led to settling, ending the phenomenon by the third day. Overall, the study underscores the importance of considering MP color in (eco)toxicological studies due to its potential to alter effects [34]. The differential effects observed with various colors of MPs indicate that color can influence the extent of their impact on aquatic organisms. For example, the lesser inhibitory effect of green MPs on algal growth suggests that MPs resembling natural food sources might be less harmful, while those with significant additives can have more pronounced toxic effects [34, 38].

Table ٢: Mean and standard deviation of heavy metal concentration in water (mg/L) and Gammarus (mg/kg) by each station in the study area

Samples	Station1		Station2		Station3		Station4		Station5	
	Gammarus	water	Gammarus	water	Gammarus	water	Gammarus	water	Gammarus	water
Cu	0.38 ±0.09	0.008± 0.002	0.54± 0.13	0.002± 0.00	0.42± 0.1	0.002 ±0.00	0.6± 0.15	0.0017 ±0.00	0.48± 0.12	0.006± 0.001
Cr	0.22± 0.05	0.08± 0.02	0.11± 0.027	0.08 ±0.02	0.23 ±0.05	0.08 ±0.02	0.23 ±0.05	0.08 ±0.02	0.12 ±0.03	0.09± 0.02
Pb	0.10 ±0.02	0.07± 0.017	0.08± 0.02	0.07± 0.017	0.06± 0.01	0.12 ±0.03	0.11 ±0.02	0.02± 0.005	0.14± 0.03	0.14 ±0.03
P value	0.001≤		0.001≤		0.001≤		0.001≤		0.001≤	

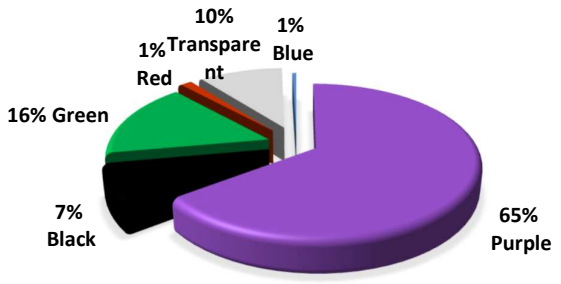

Figure 2: The abundance percentage of microplastics particles in water samples based on color in the studied stations

The highest frequency of microplastics less than 0.5 mm was observed in the second station, followed by the fourth station. For microplastics sized between 0.5 and 1, the highest frequency was recorded in the first station. In the size range of 1 to 1.5, the second station exhibited the highest frequency, while for microplastics sized between 1.5 and 2, the fifth station showed the highest frequency. Similarly, in the size range of 2 to 2.5, the highest frequency was again recorded at the fifth station. Notably, the highest frequency of particles in the size range of 0.5 to 1 was observed with 38 particles (Figure 3) [39]. Tsiaras and colleagues examined the abundance and properties of microplastics (MPs) in sea surface water samples from four coastal areas of the Mediterranean Sea. Using hydrodynamic/particle drift models; it explored MP variability, considering sources like wastewater and river runoff. The Gabes Gulf had the highest MPs abundance, followed by the Ligurian Sea, Saronikos Gulf, and Gulf of Lion. The model generally replicated observed MP levels, though overestimating smaller MPs in the Saronikos Gulf. Biofouling-induced sinking reduced smaller MP quantities offshore, while larger ones could travel further. Wave drift and advection from non-local sources, especially in the Gulfs of Lion and Gabes, affected larger MPs more. Modeling insights provide a better understanding of MP dynamics and guide environmental management to mitigate plastic pollution in the Mediterranean Sea [40]. These differences in the abundance of microplastics across various sizes and locations highlight the importance of more precise and comprehensive studies on the sources, pathways, and behaviors of microplastics in marine environments [41]. Additionally, there is a need to improve predictive models and gain a better understanding of the physical and biological processes that influence the distribution of microplastics. For example, sinking due to biofouling is a key factor in reducing the abundance of smaller particles, while larger particles can be transported over longer distances due to the effects of wave drift and advection from non-local sources [42]. Therefore, these findings can aid in the improvement of environmental management and policy-making. Increasing awareness of pollution sources and identifying high-risk areas can lead to more targeted actions to reduce microplastic pollution in marine environments [43]. In particular, further investigation into the long-term impacts of microplastics on marine ecosystems and human health remains a research priority.

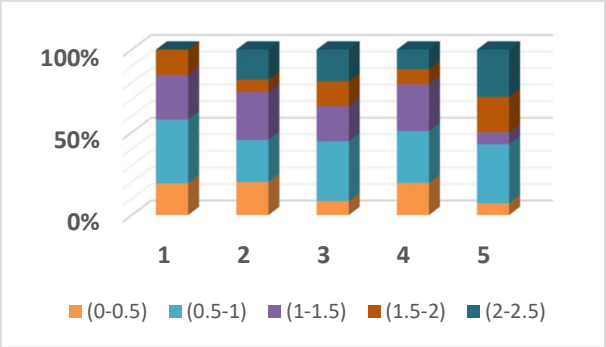

Figure 3. Percentage distribution of microplastic particle size frequency in millimeters at different stations

Fig. 4 presents the shape of microplastics in the study area. In the survey, the highest frequency of different forms of microplastic particles is related to fragment with 74 particles in the first station, pellet with 41 particles in the fifth station, line with 12 particles in the third station, and fiber with 8 particles in the third station. Fig. 5 presents the percentage distribution of microplastic form frequency. Microplaspic particles were abundantly found in beach sediments across four study sites in Virginia and North Carolina. These particles were mainly in two forms: fragments and fibers. Notably, fibers were the predominant form, making up about 93.91% ± 4.74% of the microplastic particles, with the rest being fragments [44].

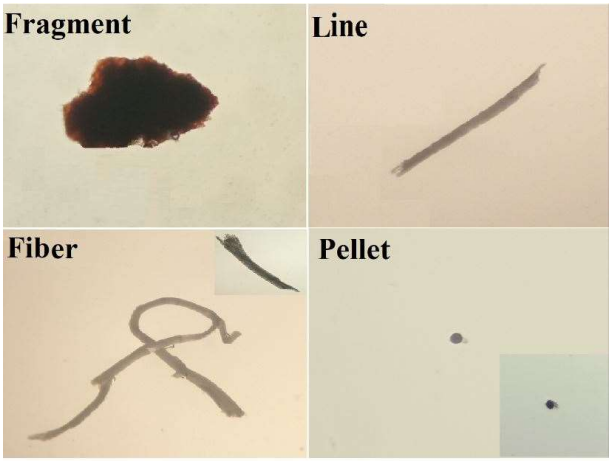

Figure. 4. presents the shape of microplastics in the southwestern Caspian Sea environment

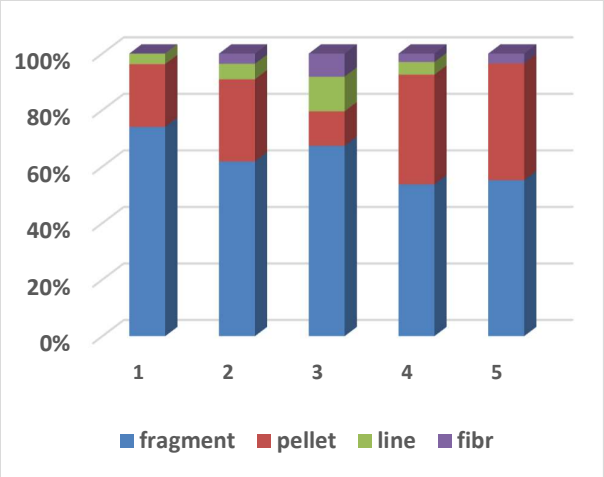

Figure 5. Percentage distribution of microplastics form frequency at different stations

The variation in the abundance and forms of microplastics across different stations highlights the influence of local environmental factors and sources of pollution. For example, the high number of fragments at station one may be due to localized sources of plastic waste and physical degradation processes. Similarly, the predominance of pellets at station five could be attributed to industrial activities or shipping routes in the vicinity [45, 46, 47].

The results underscore the need for detailed and comprehensive studies to understand the sources, pathways, and behaviors of microplastics in marine environments. Improving predictive models and understanding the physical and biological processes affecting microplastic distribution is essential [48]. For instance, biofouling-induced sinking significantly reduces the abundance of smaller particles, whereas larger particles can travel greater distances due to wave drift and advection from non-local sources [40].

As Fig. 6 shows, the results obtained from the FTIR spectrum showed the presence of polyethylene MPs in the analyzed samples. The change in FTIR peaks in the wave number range of 717, 1600, 1680 and 2928 (cm-1) indicated the presence of polyethylene MP [[49]. The methyl-CH_3 group corresponds to the absorption peaks at 2950, 2900, and 1350 (cm^{-1}), while the methylene-CH_2 group corresponds to the absorption peaks at 2800, 2850, and 1450 (cm^{-1}) [50]. Therefore, the detection of polypropylene microplastics occurs. The presence of polystyrene fibers in the sample is confirmed by the characteristics of polystyrene absorption peaks. The peaks were determined as follows: 1767 cm^{-1}, 1404 cm^{-1} (aromatic ring), 1295 cm^{-1} and 1014 cm^{-1} (carboxylic), ester or anhydride, 1092 cm-1 and 1014 cm-1, 971 cm^{-1} (C-C), 872 cm^{-1} (five substituted H in benzene), 847 cm^{-1} (two adjacent H in benzene) and 724 cm^{-1} (heterocyclic aromatics).

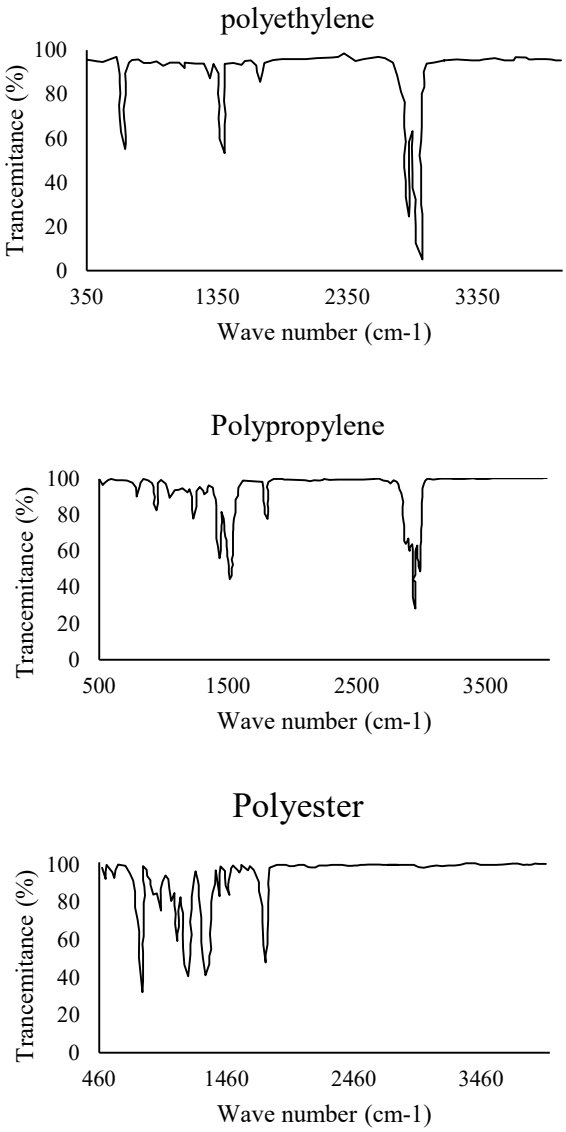

Figure 6: FT-IR spectrum of polyethylene (PE), polypropylene (PP) and polyester (PS) microplastics extracted from the Caspian Sea coasts

Marine microplastic pollution has profound economic and social ramifications, threatening natural resources, disrupting fishing and marine industries, impacting coastal tourism, and jeopardizing public health [51]. Economically, it reduces fishermen's income and the fishing industry's revenue, diminishes earnings from coastal tourism due to aesthetically degraded and unsafe beaches, and escalates healthcare costs as contaminated seafood enters the human food chain, posing serious health risks [52]. Socially, microplastic pollution leads to a decline in aquatic life diversity, affecting ecosystem stability and the cultural, recreational, and economic activities tied to these ecosystems [53, 54, 55]. It also restricts access to clean water resources for communities relying on marine and coastal waters for drinking, cooking, and sanitation [56]. Addressing this pressing issue requires the

implementation of effective measures and policies to reduce plastic usage and improve waste management, alongside promoting public awareness and fostering collective action to safeguard marine environments.

4. Conclusions

Regarding the mutual effects of microplastics abundance on heavy metals concentration in Gammarus, the results show that the presence of microplastics has led to an increase in the concentration of heavy metals in Gammarus and the aquatic environment. Statistical analysis also shows that there is a significant direct relationship at the 1% level between the microplastics abundance with the heavy metals concentration in Gammarus. In general, this research shows that the presence of microplastics in the environment can lead to changes in the composition and concentration of heavy metals in aquatic environments, which may have negative effects on the environment and human health. These findings can aid in enhancing environmental management and policy-making. Raising awareness about pollution sources and identifying high-risk areas can lead to more targeted actions to reduce microplastic pollution in marine environments. Furthermore, investigating the long-term impacts of microplastics on marine ecosystems and human health remains a crucial research priority.

5. References

[1] Johnson, C., & Bell, S. J. (2023). Linking emerging contaminants to production and consumption practices. Wiley Interdisciplinary Reviews: Water, 10(1), e1615. doi.org/10.1002/wat2.1615

[2] Al Mamun, A., Prasetya, T. A. E., Dewi, I. R., & Ahmad, M. (2023). Microplastics in human food chains: Food becoming a threat to health safety. Science of The Total Environment, 858, 159834. DOI: 10.1016/j.scitotenv.2022.159834

[3] Ziani, K., Ioniță-Mîndrican, C. B., Mititelu, M., Neacșu, S. M., Negrei, C., Moroșan, E., ... & Preda, O. T. (2023). Microplastics: a real global threat for environment and food safety: a state of the art review. Nutrients, 15(3), 617. DOI: 10.3390/nu15030617

[4] Berenstein, G., Córdoba, P., Díaz, Y. B., González, N., Ponce, M. B., & Montserrat, J. M. (2024). Macro, meso, micro and nanoplastics in horticultural soils in Argentina: Abundance, size distribution and fragmentation mechanism. Science of The Total Environment, 906, 167672. https://doi.org/10.1016/j.scitotenv.2023.167672

[5] Muthulakshmi, L., Mohan, S., & Tatarchuk, T. (2023). Microplastics in water: Types, detection, and removal strategies. Environmental Science and Pollution Research, 30(36), 84933-84948. doi.org/10.1007/s11356-023-28460-6

[6] Torres, F. G., & De-la-Torre, G. E. (2021). Historical microplastic records in marine sediments: current progress and methodological evaluation. Regional Studies in Marine Science, 46, 101868. doi.org/10.1016/j.rsma.2021.101868

[7] Choudhury, M., Sharma, A., Pervez, A., Upadhyay, P., & Dutta, J. (2022). Growing menace of microplastics in and around the coastal ecosystem. Coastal Ecosystems: Environmental importance, current challenges and conservation measures, 117-137. https://doi.org/10.1016/j.jclepro.2023.139941

[8] Courtene-Jones, W., Clark, N. J., Fischer, A. C., Smith, N. S., & Thompson, R. C. (2022). Ingestion of microplastics by marine animals. Plastics and the Ocean: Origin, Characterization, Fate, and Impacts, 349-366. Doi:10.1002/9781119768432.ch12

[9] Macneil, C., Dick, J. T., & Elwood, R. W. (1999). The dynamics of predation on Gammarus spp.(Crustacea: Amphipoda). Biological Reviews, 74(4), 375-395. https://doi.org/10.1017/S0006323199005368

[10] Al Maleki, J. S., Hussien, N. A., Tantawy, E. M., Khattab, Y., & Mohammadein, A. (2021). Terrestrial biota as bioindicators for microplastics and potentially toxic elements. Coatings, 11(10), 1152. https://doi.org/10.3390/coatings11101152

[11] Mateos-Cárdenas, A., Scott, D. T., Seitmaganbetova, G., van Pelt Frank, N. A. M., & AK, J. M. (2019). Polyethylene microplastics adhere to Lemna minor (L.), yet have no effects on plant growth or feeding by Gammarus duebeni (Lillj.). Science of the Total Environment, 689, 413-421. doi.org/10.1016/j.scitotenv.2019.06.359

[12] Mateos-Cárdenas, A., O'Halloran, J., van Pelt, F. N., & Jansen, M. A. (2020). Rapid fragmentation of microplastics by the freshwater amphipod Gammarus duebeni (Lillj.). Scientific reports, 10(1), 12799. https://doi.org/10.1038/s41598-020-69635-2

[13] Zeidi, A., Sayadi, M. H., Rezaei, M. R., Banaee, M., Gholamhosseini, A., Pastorino, P., ... & Faggio, C. (2023). Single and combined effects of CuSO4 and polyethylene microplastics on biochemical endpoints and physiological impacts on the narrow-clawed

crayfish Pontastacus leptodactylus. Chemosphere, 345, 140478. doi.org/10.1016/j.chemosphere.2023.140478

[14] Mozafarjalali, M., Hamidian, A. H., & Sayadi, M. H. (2023). Microplastics as carriers of iron and copper nanoparticles in aqueous solution. Chemosphere, 324, 138332. doi.org/10.1016/j.chemosphere.2023.138332

[15] Bakr, A. R., Fu, G. Y., & Hedeen, D. (2020). Water quality impacts of bridge stormwater runoff from scupper drains on receiving waters: A review. Science of the Total Environment, 726, 138068. https://doi.org/10.1016/j.scitotenv.2020.138068

[16] De-la-Torre, G. E. (2020). Microplastics: an emerging threat to food security and human health. Journal of food science and technology, 57(5), 1601-1608. doi: 10.1007/s13197-019-04138-1

[17] Baag, S., & Mandal, S. (2022). Combined effects of ocean warming and acidification on marine fish and shellfish: A molecule to ecosystem perspective. Science of the Total Environment, 802, 149807. https://doi.org/10.1016/j.scitotenv.2021.149807

[18] Sayadi, M. H., Pavlaki, M. D., Martins, R., Mansouri, B., Tyler, C. R., Kharkan, J., & Shekari, H. (2021). Bioaccumulation and toxicokinetics of zinc oxide nanoparticles (ZnO NPs) co-exposed with graphene nanosheets (GNs) in the blackfish (Capoeta fusca). Chemosphere, 269, 128689. doi.org/10.1016/j.chemosphere.2020.128689

[19] Bai, Z., Wang, N., & Wang, M. (2021). Effects of microplastics on marine copepods. Ecotoxicology and Environmental Safety, 217, 112243. https://doi.org/10.1016/j.ecoenv.2021.112243

[20] Trombetta, T., Vidussi, F., Roques, C., Scotti, M., & Mostajir, B. (2020). Marine microbial food web networks during phytoplankton bloom and non-bloom periods: Warming favors smaller organism interactions and intensifies trophic cascade. Frontiers in microbiology, 11, 502336. https://doi.org/10.3389/fmicb.2020.502336

[21] Natesan, U., Vaikunth, R., Kumar, P., Ruthra, R., & Srinivasalu, S. (2021). Spatial distribution of microplastic concentration around landfill sites and its potential risk on groundwater. Chemosphere, 277, 130263. doi.org/10.1016/j.chemosphere.2021.130263

[22] Sayadi, M. H., Rezaei, M. R., & Rezaei, A. (2015). Sediment toxicity and ecological risk of trace metals from streams surrounding a municipal solid waste landfill. Bulletin of environmental contamination and toxicology, 94, 559-563. DOI: 10.1007/s00128-015-1518-4

[23] Downs, C. A., Cruz, O. T., & Remengesau Jr, T. E. (2022). Sunscreen pollution and tourism governance: Science and innovation are necessary for biodiversity conservation and sustainable tourism. Aquatic Conservation: Marine and Freshwater Ecosystems, 32(5), 896-906. https://doi.org/10.1002/aqc.3791

[24] Downs, C. A., Diaz-Cruz, M. S., White, W. T., Rice, M., Jim, L., Punihaole, C., ... & Bagshaw, J. (2022b). Beach showers as sources of contamination for sunscreen pollution in marine protected areas and areas of intensive beach tourism in Hawaii, USA. Journal of hazardous materials, 438, 129546. DOI: 10.1016/j.jhazmat.2022.129546

[25] Farzadkia, M., Sedeh, M. S., Ghasemi, A., Alinejad, N., Kazemi, M. S., Jafarzadeh, N., & Torkashvand, J. (2022). Estimation of the heavy metals released from cigarette butts to beaches and urban environments. Journal of Hazardous Materials, 425, 127969. DOI: 10.1016/j.jhazmat.2021.127969

[26] Yadav, V. K., Gacem, A., Choudhary, N., Rai, A., Kumar, P., Yadav, K. K., ... & Islam, S. (2022). Status of coal-based thermal power plants, coal fly ash production, utilization in India and their emerging applications. Minerals, 12(12), 1503. DOI: 10.3390/min12121503

[27] Vig, N., Ravindra, K., & Mor, S. (2023). Heavy metal pollution assessment of groundwater and associated health risks around coal thermal power plant, Punjab, India. International Journal of Environmental Science and Technology, 20(6), 6259-6274. doi.org/10.1007/s13762-022-04284-8

[28] Birshtein YA and Romanova NN (1968) Order Amphipoda. In: Birshtein YA, Vinogradov LG, Kondakov NN, Astakhova MS and Romanova NN (eds) Atlas of Invertebrates of the Caspian Sea, pp 241–289. Pishchevaya Promyshlennost, Moscow

[29] Kharkan, J., Sayadi, M., Hajiani, M., Rezaei, M., Savabieasfahani, M. (2023). Toxicity of nickel oxide nanoparticles in Capoeta fusca, using bioaccumulation, depuration, and histopathological changes, Global Journal of Environmental Science and Management, 9(3), pp. 427-444. doi.org/10.22034/gjesm.2023.03.05

[30] Karaman, G.S., Pinkster, S. (1977). Freshwater Gammarus species from Europe, North Africa and adjacent regions of Asia (Crustacea - Amphipoda) part

I. Gammarus pulex-group and related species. Bijdragen Tot De Dierkunde 47, 1–97.

[31] Stock, J.H., Mirzajani, A.R., Vonk, R., Naderi, S., Kiabi, B. 1998. Limnic and brackish water Amphipoda from Iran. Beaufortia 48, 173–234.

[32] Kunz, P. Y., Kienle, C., & Gerhardt, A. (2010). Gammarus spp. in aquatic ecotoxicology and water quality assessment: toward integrated multilevel tests. Reviews of Environmental Contamination and Toxicology Volume 205, 1-76. https://doi.org/10.1007/978-1-4419-5623-1_1

[33] Lalouette, A., Degli Esposti, D., Colomb, C., Garnero, L., Quéau, H., Recoura-Massaquant, R., & Chaumot, A. (2024). Chronic metal contamination shapes the size structure of Gammarus fossarum populations in French headwater rivers. Ecotoxicology, 1-14. https://doi.org/10.1007/s10646-024-02777-5

[34] Chen, Q., Li, Y., & Li, B. (2020). Is color a matter of concern during microplastic exposure to Scenedesmus obliquus and Daphnia magna?. Journal of hazardous materials, 383, 121224. https://doi.org/10.1016/j.jhazmat.2019.121224

[35] Godoy, V., Blázquez, G., Calero, M., Quesada, L., & Martín-Lara, M. A. (2019). The potential of microplastics as carriers of metals. Environmental Pollution, 255, 113363. https://doi.org/10.1016/j.envpol.2019.113363

[36] Fu, Q., Tan, X., Ye, S., Ma, L., Gu, Y., Zhang, P., ... & Tang, Y. (2021). Mechanism analysis of heavy metal lead captured by natural-aged microplastics. Chemosphere, 270, 128624. https://doi.org/10.1016/j.chemosphere.2020.128624

[37] Jia, H., Wu, D., Yu, Y., Han, S., Sun, L., & Li, M. (2022). Impact of microplastics on bioaccumulation of heavy metals in rape (Brassica napus L.). Chemosphere, 288, 132576. doi.org/10.1016/j.chemosphere.2021.132576

[38] Lan, D., He, H., Song, X., & Ma, Y. (2024). Effects of food quantity on the ingestion and egestion of MPs with different colors by Daphnia magna. Aquatic Toxicology, 106976. https://doi.org/10.1016/j.aquatox.2024.106976

[39] Rasta, M., Rahimibashar, M. R., Ershad, A., Jafroudi, H. T., & Kouhbane, S. T. (2021). Characteristics and seasonal distribution of microplastics in the surface waters of southwest coast of the Caspian Sea (Guilan Province, Iran). Bulletin of Environmental Contamination and Toxicology, 107(4), 671-676. doi.org/10.1007/s00128-021-03268-7

[40] Tsiaras, K., Costa, E., Morgana, S., Gambardella, C., Piazza, V., Faimali, M., ... & Garaventa, F. (2022). Microplastics in the Mediterranean: variability from observations and model analysis. Frontiers in Marine Science, 9, 784937. https://doi.org/10.3389/fmars.2022.784937

[41] Waldschläger, K., Lechthaler, S., Stauch, G., & Schüttrumpf, H. (2020). The way of microplastic through the environment–Application of the source-pathway-receptor model. Science of the Total Environment, 713, 136584. https://doi.org/10.1016/j.scitotenv.2020.136584

[42] Onink, V., Jongedijk, C. E., Hoffman, M. J., van Sebille, E., & Laufkötter, C. (2021). Global simulations of marine plastic transport show plastic trapping in coastal zones. Environmental Research Letters, 16(6), 064053. https://doi.org/10.1088/1748-9326/abecbd

[43] Sangkham, S., Faikhaw, O., Munkong, N., Sakunkoo, P., Arunlertaree, C., Chavali, M., ... & Tiwari, A. (2022). A review on microplastics and nanoplastics in the environment: Their occurrence, exposure routes, toxic studies, and potential effects on human health. Marine pollution bulletin, 181, 113832. https://doi.org/10.1016/j.marpolbul.2022.113832

[44] Dodson, G. Z., Shotorban, A. K., Hatcher, P. G., Waggoner, D. C., Ghosal, S., & Noffke, N. (2020). Microplastic fragment and fiber contamination of beach sediments from selected sites in Virginia and North Carolina, USA. Marine Pollution Bulletin, 151, 110869. doi.org/10.1016/j.marpolbul.2019.110869

[45] Wang, C., Zhao, J., & Xing, B. (2021). Environmental source, fate, and toxicity of microplastics. Journal of hazardous materials, 407, 124357. https://doi.org/10.1016/j.jhazmat.2020.124357

[46] Karlsson, T. M., Arneborg, L., Broström, G., Almroth, B. C., Gipperth, L., & Hassellöv, M. (2018). The unaccountability case of plastic pellet pollution. Marine pollution bulletin, 129(1), 52-60. https://doi.org/10.1016/j.marpolbul.2018.01.041

[47] Gorman, D., Moreira, F. T., Turra, A., Fontenelle, F. R., Combi, T., Bícego, M. C., & de Castro Martins, C. (2019). Organic contamination of beached plastic pellets in the South Atlantic: Risk assessments can benefit by considering spatial gradients. Chemosphere, 223, 608-615. https://doi.org/10.1016/j.chemosphere.2019.02.094

[48] Sheela, A. M., Manimekalai, B., & Dhinagaran, G. (2022). Review on the distribution of microplastics in the oceans and its impacts: Need for modeling-based approach to investigate the transport and risk of microplastic pollution. Environmental Engineering Research, 27(4). https://doi.org/10.4491/eer.2021.243

[49] Daniel, D. B., Ashraf, P. M., Thomas, S. N., & Thomson, K. T. (2021). Microplastics in the edible tissues of shellfishes sold for human consumption. Chemosphere, 264, 128554. doi.org/10.1016/j.chemosphere.2020.128554

[50] Husin, M. R., Arsad, A., Suradi, S. S., Alothman, O., Ngadi, N., & Kamaruddin, M. J. (2017). Fourier transforms infrared spectroscopy and X-ray diffraction investigation of recycled polypropylene/polyaniline blends. Chemical Engineering Transactions, 56, 1015-1020. https://doi.org/10.3303/CET1756170

[51] Rahman, M. N., Shozib, S. H., Akter, M. Y., Islam, A. R. M. T., Islam, M. S., Sohel, M. S., ... & Malafaia, G. (2023). Microplastic as an invisible threat to the coral reefs: sources, toxicity mechanisms, policy intervention, and the way forward. Journal of Hazardous Materials, 454, 131522. https://doi.org/10.1016/j.jhazmat.2023.131522

[52] Kurniawan, T. A., Mohyuddin, A., Othman, M. H. D., Goh, H. H., Zhang, D., Anouzla, A., ... & Pasaribu, B. (2024). Beyond surface: Unveiling ecological and economic ramifications of microplastic pollution in the oceans. Water Environment Research, 96(7), e11070. https://doi.org/10.1002/wer.11070

[53] Chaudhry, A. K., & Sachdeva, P. (2021). Microplastics' origin, distribution, and rising hazard to aquatic organisms and human health: Socio-economic insinuations and management solutions. Regional Studies in Marine Science, 48, 102018. https://doi.org/10.1016/j.rsma.2021.102018

[54] Yose, P., Thondhlana, G., & Fraser, G. (2023). Conceptualizing the socio-cultural impacts of marine plastic pollution on human well-being–a perspective. Marine Pollution Bulletin, 194, 115285. https://doi.org/10.1016/j.marpolbul.2023.115285

[55] Hosseini, R., Sayadi, M. H., Aazami, J., & Savabieasfehani, M. (2020). Accumulation and distribution of microplastics in the sediment and coastal water samples of Chabahar Bay in the Oman Sea, Iran. Marine pollution bulletin, 160, 111682. doi.org/10.1016/j.marpolbul.2020.111682

[56] Onyena, A. P., Aniche, D. C., Ogbolu, B. O., Rakib, M. R. J., Uddin, J., & Walker, T. R. (2021). Governance strategies for mitigating microplastic pollution in the marine environment: a review. Microplastics 2022 (1): 15–46. https://doi.org/10.3390/microplastics1010003

INTERNATIONAL JOURNAL OF
COASTAL, OFFSHORE & ENVIRONMENTAL ENGINEERING IJCOE Vol.11/No. 2/Spring 2026 (38-48)

Available online at: www. Ijcoe.org

Reliability Analysis of Berm Breakwaters Based on the Environmental Data on the Northern Coasts of Oman Sea

Pouya Zarbipour[1], Hassan Akbari[2*], Ali Sheikhbahaei[3, 4]

[1] *Department of Civil and Environmental Engineering, Tarbiat Modares University, Tehran, Iran, Pouyazarbipor@modares.ac.ir*
[2*] *Department of Civil and Environmental Engineering, Tarbiat Modares University, Tehran, Iran, Akbari.h@modares.ac.ir*
[3] *PhD Candidate University of Hormozgan, Department of Non-Living Atmospheric and Marine Science, Faculty of Marine Science and Technology, University of Hormozgan, Bandar Abbas, Iran*
[4] *Iranian National Institute for Oceanography and Atomospheric science(INIO), Tehran, Iran*
Ali.Sheikhbahaei@inio.ac.ir

ARTICLE INFO

Article History:
Received 16Jan 2025
Accepted 28 Aug 2025
Available online 20Apr 2026

Keywords:
Reliability Analysis
MCS
Berm Breakwaters
Copula Dependency
Probability of failure

ABSTRACT

Berm Breakwaters (BB) are reshaping coastal structures which can be classified as Hardly, Partly, and Fully Reshaping (HR, PR, and FR) breakwaters based on their stability. This study evaluates the reliability of different berm breakwaters using environmental data from the Iran's southern coast region. The D-Vine structure was identified as the most suitable for analyzing dependencies between input variables. Two failure modes, wave overtopping and berm recession were used to assess reliability through current deterministic design methods. The findings show that dependencies between input variables generally had a minor impact on the calculated probability of failure (Pf). However, ignoring these dependencies can lead to underestimated designs, especially when wave height and water level strongly correlate. The study also found that the current deterministic design criteria for berm breakwaters are more conservative compared to conventional rubble mound breakwaters. This is due to the additional berm width based on Dn50. Among different berm breakwater types, HR breakwaters, with larger armor units and smaller berm recessions, had the lowest berm failure probability. In contrast, the overtopping Pf values is almost the same for all the BB types. The results of this study shows the importance of including dependencies between input variables and paying attention to the required safety margin in reliability design of berm breakwaters based on conventional methods.

1. Introduction

One of the most important coastal structures for shielding harbor areas from waves is a berm breakwater (BB). The idea of Berm Breakwaters was first presented more than 40 years ago in order to improve the use of rock in the conventional rubble mound breakwaters. The provided berm in these breakwaters keeps changing shape in response to wave attacks until it stabilizes. Typically, the final stable profile resembles an S-shaped curve. Compared to traditional breakwaters, this idea enables the use of smaller armor stones within a wider berm [1]. The berm breakwaters are usually classified based on their reshaping state. Many studies were performed in the last years to investigate the stability and hydraulic performance of berm breakwaters such as [2], [3], [4], [5], [6], [7], [8], [9], [10], [11], [12], [13], [14], [15], [16], [17], [18], [19], [20], [21]. The stability number (H0) for damage prediction was first proposed by [22]. [23] added the wave period and presented a new stability number (H_0T_0) as part of their ongoing research. [24] discovered in another experimental study that $H_0\sqrt{T_0}$ is more capable of presenting the berm damage parameter S_d for HR breakwaters than H_0T_0. [9] and later [2] examined the cumulative effect of prior storms on the final berm recession and proposed a modified stability number ($H_0\sqrt{T_0}$) based on wave energy, taking into account the greater influence of wave height than the wave period. Research is still being done to determine the best stability number to use when presenting the BB behavior. However, the probabilistic response of berm

breakwaters at the design point under different uncertainties has not been examined in any of the earlier studies.

Usually, the type of berm breakwater determines berm recession. Based on the dimensionless variables H_0T_0 and H_0, the PIANC guideline [25] classified berm breakwaters for the first time in 2003 into three groups: statically stable non-reshaped, statically stable reshaped, and dynamically stable reshaped berm breakwaters. Later, [16] introduced new classifications as Hardly reshaping (HR), Partly reshaping (PR), and Fully reshaping (FR) types, modifying this one based on their final reshaping against design wave (100 years in their definition). FR breakwaters that have considerable recession are classified as mass-armored berm breakwaters (PR-MA), while HR breakwaters with a limited recession are also known as Icelandic-type berm breakwaters (HR-IC). Both mass-armored (PR-MA) and Icelandic-type (PR-IC) berm breakwaters are susceptible to partial reshaping. The design of coastal and marine structures is fraught with uncertainty. Simple deterministic methods are typically preferred by designers, but they don't reveal anything about the probability of failure. Moreover, it is unclear—and occasionally disregarded—how safety factors are used in the current deterministic codes for coastal structures. Nearly all design formulas for coastal structures are derived using central fitting to test data, according to [26], [49]. As a result, these semi-empirical equations did not model any uncertainty, and the only safety margin that is presented is the chosen return period. However, in order to account for a safety margin, characteristic loads and resistance values—typically with one fractile distance to the mean values—are frequently used in structural codes.

Few studies have been conducted for the fully probabilistic design of coastal structures, especially breakwaters, in contrast to the structural field. A new Bayesian formula for predicting the force acting on caisson breakwaters was presented by [27], [28], who also conducted a reliability analysis on these structures without taking environmental parameter dependencies into account. One of the elements affecting how applied loads are distributed is the correlation between input parameters. For instance, the design of breakwater crest elevation may be influenced by the close correlation between wave height and water level [29], [30], [31], which may change the probability of breakwater failures. A study on a rubble mound breakwater using different copula dependency structures was recently carried out by [32]. According to their findings, the independent, Gaussian, and two-variable Gumbel structures had lower construction costs than the D-Vine structure by 9.32%, 5.7%, and 3.12%, respectively. In addition, [33] suggested a novel probabilistic method for designing desalination outfall systems close to coastlines with the required safety levels, taking into account a correlation between environmental data. They demonstrated how dependency structures have a major impact on failure probability. Compared to coastal structures, offshore structures have a longer history of reliability analysis using dependency structures. For example, [34] compared the results of multiple pairs of copula families between wave height, period, and wind speed in order to examine the impact of copula dependency structures on offshore platform design. Their findings demonstrated that the best fits for these data sets were given by Gaussian and Gumbel copulas. As an additional illustration, [35] used independent, Gaussian, and D-Vine copula dependency structures to examine the probability of structural failure of an offshore platform on Canada's east coast. Furthermore, [36] used a mixed copula structure to examine the structural reliability evaluation of an offshore platform and showed that the dependency structure can significantly impact reliability analysis.

As was mentioned in the paragraphs above, no specific research was done to evaluate the dependability of berm breakwaters with various reshaping classifications. This study examines the effects of various parameters in an attempt to fill this gap. Following the results obtained in section 5 of this paper, the effects of the breakwater stability number and dependency structures on the results are discussed for this purpose. Before that, Section 2 reports the study region along with the statistical features and interdependencies among environmental data. Following that, section 3 discusses the deterministic design criteria, and section 4 introduces the reliability method concept and the used limit state functions.

2. Input data and Dependency modeling

2.1 Study area and Environmental data

The region under investigation is situated along the Oman Sea on Iran's southern coast (Figure 1). With a maximum depth nearly 13.7 meters in relation to the site Chart Datum (CD), this breakwater safeguards one of Iran's most significant harbors. In this region, monsoon waves predominate, and the regional wave rose shows that most of the waves come from the south. According to research by [37], the combination of higher frequency waves during non-monsoon times and large waves during the southwest monsoon is what causes the multi-peaked wave spectra in this area. Some researchers have examined the dominant wave systems and provided appropriate wave spectra for this region based on the wave measurements that are currently available [38], [39].



Figure 1. Locations of the study area in Iran.

Following the study by [32], the environmental data (Hs, Tp, and WL) recorded with a capture rate of 99% over 22 years, from January 1994 to December 2015, are used in this study. In contrast to their study, this one looks into the probability of failure against design conditions (with a 100-year return period). The Chabahar buoy provided the Hs and Tp data for this data set [38], while the IOC station measurements, whose dependability and quality were confirmed by earlier research, provided the WL data combining tidal levels and storm surges [40], [41], [42].

2.2 Dependency Structures

Copulas are effective tools for modeling how variables depend on one another. They make it possible to separate dependency structures from marginal distributions and to generate joint probability distribution functions. This separation provides flexibility in the modeling process and is especially helpful when working with intricate and unusual patterns. The relationship between copula functions and marginal distributions is shown in Figure 2.

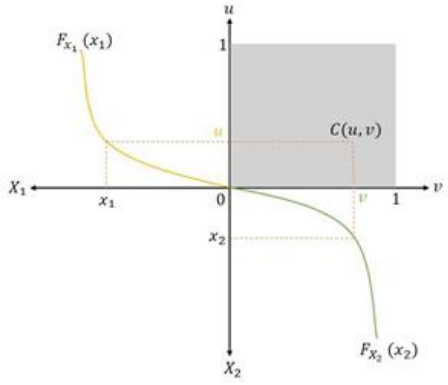

Figure 2. Relationship between bivariate marginal distributions and copula functions [43].

A multivariate cumulative distribution function with uniform edges on a super plane $[0,1]^M$ is called an M-dimensional copula.

$$F_X(x_1, x_2, \dots, x_M) = C(F_{X_1}(x_1), F_{X_2}(x_2), \dots, F_{X_M}(x_M)) \quad (1)$$

$X = (X_1, X_2, \dots, X_M)$ indicates an m-dimensional random sequential marginal distribution functions $F_{X_1}, F_{X_2}, \dots, F_{X_M}$, and C is the copula. This allows us to express the joint distribution function using a copula.

Despite their popularity due to their ease of use, Gaussian copulas assume that marginal distributions follow a Gaussian pattern and have limitations when it comes to modeling tail dependencies [44]. Other copula families can be used to solve this problem. As an example, the coastal engineering field has made extensive use of the hierarchical and nested Archimedean copulas as well as Vine copulas [45].

In this study, four dependency structures have been studied in accordance with [32] and Copula modeling was done using MvCAT and Python's pyvinecopulib package. Independent variables, Gaussian copula for all variable pairs, bivariate Gumbel copula for the Hs-Tp pair, and D-Vine copula for all variable pairs are examples of these dependency structures.

3. Deterministic design Criteria

As mentioned in the previous paragraphs, the stability number Ns was used to define three types of berm breakwaters, including HR, PR, and FR. HR breakwaters typically have less berm recession and higher required armor weights than other types. Three designed sections that are compatible with HR, PR, and FR berm breakwaters have been taken into consideration in this study, in accordance with the previously mentioned classification. Fig. 3 shows a schematic view of the variables and the berm breakwater section.

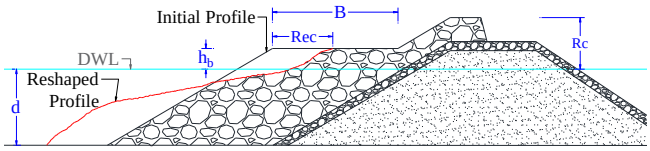

Figure 3. A schematic view of the variables and the berm breakwater section

3.1 Berm geometry: (B and hb)

As a crucial geometrical parameter, berm width should be sufficiently large to resist design waves and the resulting recession. As a result, the berm recession and the required safety factor determine its value. The introduction of a formula for predicting the berm recession has been attempted numerous times in the literature, including by [2], [3], [4], [5], [6], [7], [8], [9], [10], [11], [12], [13], [14], [15], [16], [17], [18], [19], [20], [21]. Numerous formulas based on various variables and presumptions have been proposed by these studies. While other formulas might include other variables such as berm level, wave period, water depth, and so forth, the formula put forth by [16], for instance, solely depends on H_0. A new berm classification and design methodology was presented by [16], who based it solely on H_0 as the most critical berm recession parameter.

Despite neglecting other factors, they ultimately came to the conclusion that berm recession is significantly

influenced by other factors like berm level, seaside slope, toe depth, and cumulative recession. As a result, they applied positive or negative scores to represent the impact of these parameters. This study evaluates the berm recession in a deterministic design or when defining the limit state functions using a new proposed formula by [11]. Genetic programming and fitting to a wide range of parameters were used to derive this equation. A researcher can examine the uncertainties of various variables on the berm breakwater performance by using this equation in the reliability framework because it contains a large number of geometrical and environmental parameters. Therefore, it is applied in this study to predict berm recession under various hydrodynamic and geometrical circumstances.

The required berm width can be designed with a safety margin once the berm recession under design wave conditions has been determined. However, according to (Van der Meer and Sigurdarson, 2016), this value should be verified using the minimum permitted berm width, which is $B_{min} = \max(3D_{n50}, Rec + 1D_{n50})$. The literature suggests limited design recommendations about the safety margin value. [25] made a well-known suggestion that restricts the residual berm width following reshaping to $4D_{n50}$ for the ultimate limit state. Since Rec is the berm recession under the design wave, the required berm width should be at least $B_{Pianc} = Rec + 4D_{n50}$. (Van der Meer and Sigurdarson, 2016) provided the alternative suggestion, which was based on the breakwater type and resiliency level. According to Table 1, they suggested that the minimum berm width be $B_{VS} = Rec/P\%$, where P is the desired resiliency. Based to their definition, a structure's resilience is its ability to recover back from or withstand design waves. They stated that an HR breakwater is more resilient than the other two types and proposed a resiliency value based on the classification of berm breakwaters.

Table 1. The proposed resiliency values for berm design [25]

BB Category	Ns	P%	B/Rec
HR	1.5-2.0	10–20	5-10
PR	2.0-2.5	20–40	2.5-5.0
FR	2.5-3.0	≤70	1.4-2.5

as a result, the recommended berm width for HR breakwaters is (5~10) Rec, whereas for FR type, it is (1.4~2.5) Rec. The required berm width would be more in FR than in HR because the recession in FR breakwaters is more than in HR. Finally, because resilience (P%) can increase the cost of the Berm breakwater, (Van der Meer and Sigurdarson, 2016) recommended that the resilience should be selected based on the required safety level by the designer.

The berm level can be a little above the design water level or much higher, as discussed by [16]. A minimum berm level of $h_b=0.6H_{sD}$ above DWL was also recommended by them. According to (Van der Meer and Sigurdarson, 2016), the minimum berm level should not be less than MHWS+dW, where dW varies between 0.5 and 1.5 m depending on the annual wave characteristics.

3.2 Crest Freeboard height: (Rc)

The crest elevation is one of the geometrical parameters that affects the overtopping rate and hydraulic response of berm breakwaters, in addition to the berm geometry. In other words , the value of Rc is determined for each permitted overtopping. The design overtopping rate q_{Do} (one standard deviation higher than the mean overtopping ($\overline{q_o}$), which will be used later for the definition of the overtopping limit state function), was proposed in the Eurotop manual as follows based on the research conducted by (Van der Meer et al., 2018):

$$q_{Do} = 0.1035 \times exp\left[-\left(1.35\frac{R_c}{H_{m0}\gamma_{BB}\gamma_\beta}\right)^{1.3}\right] \times \sqrt{gH_{m0}^3} \qquad (2)$$

where, especially in deep waters, the spectral wave height, H_{m0}, is close to the value of Hs. The height of the crest above the design water level is known as the crest freeboard height (Rc). When S_m is the wave steepness, the influence factor for a berm is γ_{BB}, which is $\gamma_{BB}=0.68-4.1S_m-0.05\ B/H_{m0}$ for HR and PR berm breakwaters and $\gamma_{BB}=0.7-8.2S_m$ for FR breakwaters. Finally, since most of waves come from the south side, the effect coefficient of the wave angle, γ_β, is one. The allowed overtopping value, q_{all}, is depends generally by the breakwater's required performance under design and annual waves.

3.3 Other geometrical parameters

Table 6 shows the values and design criteria taken into consideration for the other parameters. The thickness of the armor layer (ha), filter layer (u), and crest width (Cw) can be calculated after the armor diameter is determined as Dn50. The height of the filter layer above the core materials (hf) depends on the require freeboard and is calculated as $hf = Rc + DWL - hc - ha$. Finally, as shown in the table, the height of the core layer (hc) is chosen to provide a minimum safe working level for construction activities.

Table 2. The geometrical parameters criteria in the berm breakwater

Geometrical parameters	Considered design criteria
ha	$2\ D_{n50}$
u	$0.8\ D_{n50}$
C_w	$4\ D_{n50}$
hc	$d0+WL_{1y}+0.6Hs_{1y}$

4. Reliability Analysis and Limit State Functions

Limit state functions should first be defined for each failure mode *i* in order to conduct reliability analysis and failure probability investigation. $G_i = R_i - S_i$ is the limit state function that shows the structural resistance minus the load effect on the structure. This definition states that when the structure response surpasses its resistance, or when G_i becomes negative, the structure fails. A several of reliability methods can then be used to determine the probability of failure after introducing the R and S as probable variables. The probability of failure $P_{fi} = P(G_i \leq 0)$ is calculated in this study using the Monte Carlo simulation method. It is calculated as $P_{fi} = N_f/N_t$, where N_t is the total number of samples and N_f is the number of samples with $G_i \leq 0$. When the calculated Pf is less than the target or accepted probability of failure, the design is accepted.

The mechanism through which the structure or one of its elements occurs is indicated by the failure mode [47]. Limit state functions can be used to assess the various types of failures that berm breakwaters can undergo. These include overtopping, breakwater core settlement, bed soil settlement instability, and—above all—the failure of the berm breakwater width. The damage brought on by the berm breakwater core settling is not considered critical given the properties of the berm breakwater and the soil at the study site; as a result, it has not been included in the analysis of this study. Finally, this study examined two failure mechanisms as independent limit state functions, denoted by G_i, where $i = B, O$ represents failure resulting from excessive berm recession and failure resulting from excessive overtopping, respectively. The following sections provide a more thorough introduction to these functions.

4.1 Failure due to berm recession

This type of failure occurs when environmental loads cause the berm recession (Rec) to be exceeds than the allowed berm recession or structure resistance. As discussed in the previous sections, the formula presented by [11] is used in this study to evaluate the Rec (as the load S in the limit state function). According to (Van der Meer and Sigurdarson, 2016), the remaining berm width must be at least equal to $1D_{n50}$ so as for the structure resistance R, also known as the allowed berm recession, to be defined. Stated differently, when the predicted recession against probabilistic variables exceeds (B - $1D_{n50}$), berm failure occurs place. The limit state function for berm failure, as described above, would be:

$$\begin{aligned} G_B &= [B - 1D_{n50}] \\ &- C_R \left[\left(0.02067 \left(H_0 \sqrt{T_{0P}} \right)^{1.971} \left(\frac{d}{D_{n50}} \right)^{-0.1087} Ln \left(\frac{N}{3000} \right. \right. \right. \\ &\left. \times \frac{d}{D_{n50}} \right) + 21133 \left(H_0 \sqrt{T_{0P}} \right)^{2.094} \left(\frac{h_b}{H_s} \right) \left(\frac{d}{D_{n50}} \right) \\ &\times \left(Ln(f_g) \right)^{7.187 f_g} - 81.74 \times 10^{-5} \\ &\left. \left. \times 1.378^{\left(\frac{h_b}{H_s} \right)} \left(H_0 \sqrt{T_{0P}} \right)^3 \left(\frac{N}{3000} \right) \left(\frac{h_b}{H_s} \right)^2 - 1.245 \right) \times D_{n50} \right] \end{aligned} \quad (3)$$

There are some uncertainties resulting from the prediction formulas for wave overtopping and berm recession in addition to the uncertainties of the environmental variables that show up in the S parameter. This uncertainty is actually represented by C_R in this equation. [11] proposed a distribution around the mean value of berm recession as Eq.(3). According to their findings, the variable C_R's mean and coefficient of variation (CoV) are chosen for this study to be 1.0 and 0.1, respectively.

4.2 Failure due to wave Overtopping

The second failure mode this study addresses is failure mode on by overtopping. According to the guidelines proposed by Eurotop 2018, the overtopping discharge is calculated [46]. It should be noted that the distribution of overtopping discharge is assessed in this section using the mean and standard deviation of the overtopping rates. In section 5.3, however, the design overtopping formula (one standard deviation higher the mean values) was used for the deterministic design. The following definition of the corresponding limit state function to the overtopping failure is based on the discussions above:

$$G_O = q_{all} - \left(C_{O1} \times exp \left[- \left(C_{O2} \frac{R_c}{H_{m0} \gamma_{BB} \gamma_\beta} \right)^{1.3} \right] \times \sqrt{g H_{m0}^3} \right) \quad (4)$$

The overtopping rate is utilized in this equation, and its distribution around a mean value is controlled by the coefficients C_{O1} and C_{O2}. According to Eurotp 2018, these coefficients have respective mean values of 0.09 and 1.5, as well as coefficients of variance of 0.0135 and 0.15. The other parameters are the same to those that are included in Eq.(4). To create a design condition with a safety factor, the C_{O1} and C_{O2} coefficients were actually changed to constant values (one standard deviation from the mean) in that equation ($C_{O1+1\sigma} = 0.1035$, $C_{O2-1\sigma} = 1.35$).

5. Results and discussions

5.1 Design environmental data

The wave height time series and the histogram plot for environmental variable pairs appear in Fig. 4.

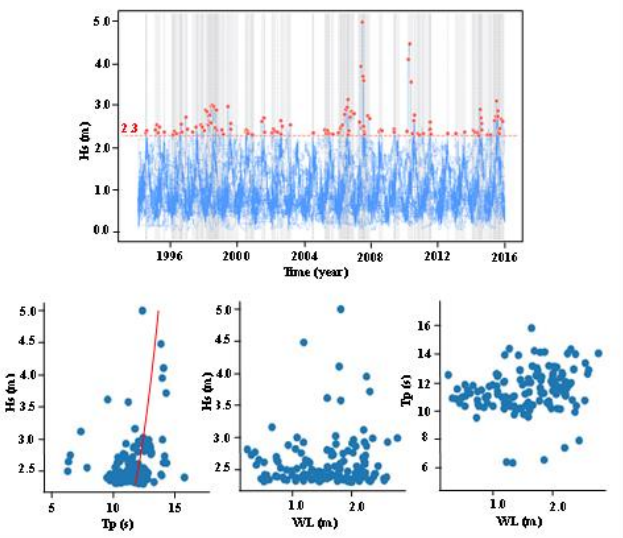

Figure 4. Histogram plot for pairs of environmental variables

In order to calculate the design values with a specific return period, as well as evaluate the dependencies between the variables, these data were utilized in this study. Finding a threshold that distinguishes large waves from those presenting the characteristics of design waves is the first step in both of these analyses. Following that, design events can be estimated as discussed in the paragraphs that follow, and section 3.2 can be used to calculate the dependency structure between the variables. The threshold wave height of 2.3 was threshold by [32] using two mean residual life and parameter stability techniques on the same data set in order to identify the waves with design characteristics.

Using the same method, the design wave with 100 years of return periods was found to be H_{sD}=5.03 m by fitting the Weibull distribution to the chosen waves that were higher than 2.3 m. According to [48], Figure 4 shows a solid red line that represents the relationship between the mean wave height and peak wave period, which is $Tp=10.1Hs^{0.19}$. T_{pD}=13.6 s would be the mean value of the design wave period based on this relationship. The deterministic design of the berm breakwater was based on this design wave. However, in order to account for the uncertainties in a reliability design, a distribution function around these mean values is required. The normal distribution was chosen for the DWL variable and the Lognormal distribution for the H_{sD} and T_{pD} variables based on the measurements. The coincident design WL is an important variable in addition to the design wave height and period. The predicted berm recession and wave overtopping rate are impacted by changes in the values of the crest freeboard (Rc) and the berm level (hb), which are both dependent on the DWL value. A reliability design takes consideration of the uncertainties surrounding the mean design values (H_{sD}, T_{pD}, and DWL). For calculating the design values separately, wave parameters (Hs, Tp) and water level (WL) can be examined separately. For example, in the area under research, a design wave with H_{sD}=5.03m and T_{pD}=13.6m occurs once every 100 years. The maximum water level, however, is 3.04 meters every 100 years. The correct combination of (or jointed) mean design values for any desired return period is up for discussion, though. Whether or not these maximum events occur at the same period every 100 years is the question. The joint distribution of the variables in the region determines a response to this question. In general, it is expected that the return period corresponding with a concurrent situation will exceed 100 years. A common practice for initial or traditional design purposes is to make conservative assumptions that take into consideration all of the maximum values at once. For example, assuming that design waves are jointed with DWL= MHWS+storm surge. The storm surge for the 1-year and 50-year return periods was 0.21m and 0.57m, respectively, and the MSL (Mean Sea Level) and MHWS (Mean High Water Spring) elevations in the studied area are 1.55m and 2.47m with respect to the site CD. Such an assumption results in a DWL of 3.04m based on these values. If a joint probability analysis (JPA) were conducted, this value would be less.

Table 3 shows the jointed and not-jointed design variables that have been modified for the annual and 100-year return periods. H_{sD}=5.03m, T_{pD}=13.6s, and DWL=2.59m are the mean values of the joint design variables that were used to design the berm breakwater in this study. Therefore, the jointed design water depth would be d=16.3m based on the still water depth at the location of the berm breakwater under study (d0=13.7 m, CD). The table shows the water depth and annual wave parameters in addition to the chosen 100-year design period. The top level of the core layer and the minimum height of the berm level will also be determined by the design using these values.

Table 3. Design wave parameters in the area based on the performed JPA

Return period (years)	Hs_y (m)	Tp_y (s)	Jointed WL_y (m)	Not jointed WL_y (m)
Annual: 1	2.23	11.67	1.64	2.68
Design: 100	5.03	13.6	2.59	3.04

As previously mentioned, the breakwater is situated on the northern coasts of the Oman Gulf, where the design water depth is d=d0+DWL. The mean value of DWL is 2.59 meters, and d0 is 13.7 meters in respect to CD. Table 4 shows environmental variables

along with their distribution functions. Actually, these variables cause uncertainty in the outcomes. The uncertainty in H_{sD} is corresponding to a coefficient of variation of approximately 5 to 20 percent, as per [26]. The small sample size, measurement errors, hindcast model errors, etc., may all contribute to this uncertainty. According to the measurement type, the suggested CoV (Coefficient of Variation) for the design peak wave period T_{pD} falls within the same range. As shown in Table 4, a CoV of 0.15 is chosen for both wave height and period in this investigation. Storm surges and tidal levels consists DWL, but tidal uncertainty is lower than storm surge uncertainty. As a result, the literature recommended that the CoV of storm surge and tide elevation be between 0.1-0.25 and 0.001-0.07, respectively [26]. To study for the uncertainties in both surface water level and seabed variations, a CoV value of 0.2 is chosen for DWL in this investigation. In addition, all of the variables' distributions and standard deviations are selected to have a physical basis in accordance with the characteristics of the field under study and the materials at available. Since $N = Ts/Tm$, the number of waves is affected by storm duration Ts.

Table 4. Environmental variables and their distribution

Variable index	Variables	Distribution	Mean	CoV	Unit
5	H_{sD}	Lognormal	5.03	0.15	m
6	T_{pD}	Lognormal	13.6	0.15	s
7	ρs	Normal	2450	0.02	kg/m^3
8	ρw	Normal	1025	0.01	kg/m^3
9	DWL*	Normal	2.59	0.2	m
10	Ts	Triangular	9	1/3 (s.d.=3)	hr
11	fg	Normal	1.5	0.05	-

The seabed depth in respect to CD is indicated by the water depth, d=d0+DWL, where d0 is a constant value.

5.2 Goodness of fit for dependency structures

Four dependency structures are considered in this study: D-Vine, Gaussian, Gumbel, and independent copula. Figure 5 shows the performance of these structures compared to the measurements. The Log-Likelihood and Akaike Information Criteria (AIC) indexes are also computed in evaluating the fit's the suitability for these structures. The results showed that the D-Vine copula best fit the AIC index of -22.93 and the total Logik index of 13.47. Then, with total Logik values of 8.93 and 7.71 and AIC values of -13.86 and -9.43, respectively, the Gumbel and Gaussian copulas offer the best fits in turn. As anticipated, the independent condition produces the worst fit. As anticipated, since the same input data were used, the results were the same to those reported by [32]. The D-Vine copula is chosen as the base dependency structure based on the results.

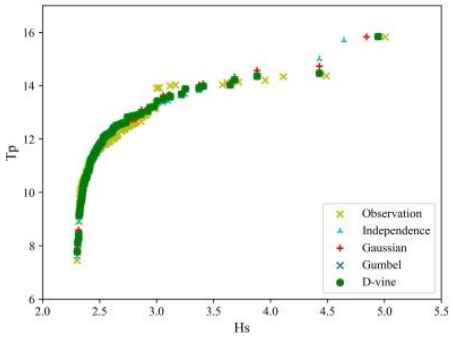

a) Pair *Hs-Tp*

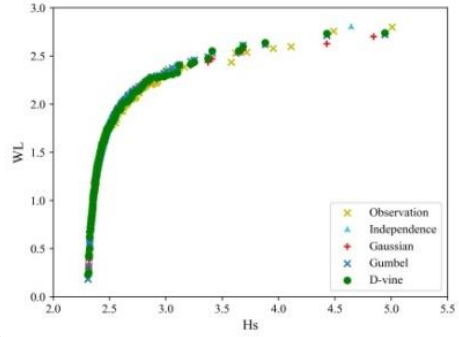

b) Pair *Hs-WL*

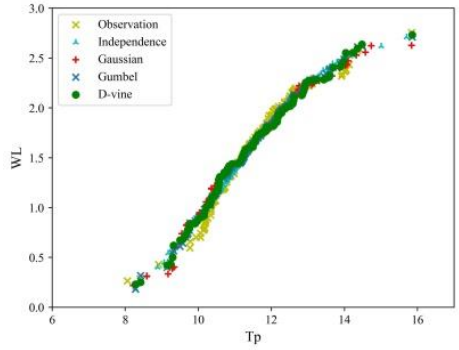

c) Pair *WL-Tp*

Figure 5. Comparison between the observations and the dependency model predictions for the pairs of environmental variables

5.3 Deterministic design of sections

Table 5 shows the required berm width based on the two above references.

Table 5. The values of design parameters in the deterministic design

Design parameters	Berm Breakwater Category		
	HR	**PR**	**FR**
Ns	1.85	2.25	2.75
hb (m)	3	3	3
Rc (m)	6.55	6.29	6.96
B (m)	12	13.8	17
Rec	4.19	7.41	11.73
Rec+4Dn50	12	13.8	17
Rec/P%	21~42	19~37	17~29

According to the table, the recommended berm width by [16] generally much larger (by a maximum of 2 to 4 times for HR type) than the values proposed by [25]. This could be because of the particulars of the area under study. The berm width is taken into consideration in accordance with PIANC's recommendations based on these values and the built berm breakwater in this area. In general, a more

conservative structure with less failures is probability by a wider berm. Although being helpful in deterministic design, design recommendations don't tell us anything about the structure's probabilistic performance.

In addition to the berm width, Eq.(3) indicates that the berm level (hb) affects the berm recession and the stability of the breakwater. According to previous studies, a higher berm generally dissipates more wave energy and results in less berm recession. Given that dw is 1.0 meters above MHWS, a minimum value of hb=0.9 is used in this research. The values reported in Table 5 can be derived from these values and the corresponding wave and water levels in Table 3.

5.4 Reliability analysis of the designed sections

The Pf of the berm width designed using the deterministic recommendations generally less than the Pf resulting from excessive overtopping discharge, as shown in Table 6. A safety margin is causes for the berm width by adding an extra width of 4Dn50 to the predicted mean value of the berm recession (Table 5), and for the overtopping limit state by applying an overtopping prediction based on a formula that is one fractile higher than the mean value (Eq.(4)). Table 6 shows that a safe HR breakwater with 3.88E-02 Pf was designed by applying a safety margin of $4D_{n50}$, while a FR breakwater designed using the same criterion had a Pf of 2.13E-01. In addition to the HR breakwater's smaller berm recession, the larger armor units (D_{n50}) are the cause. On one hand, the structure response (recession) was reduced, and on the other hand, the resistance (R) has been excessively raised. Compared to the other types, these two factors provided a more reliable HR breakwater. However, the calculated Pf for the overtopping limit state is almost the same for all of the HR, PR, and FR breakwater types as shown in the table due to the fractile concept was used for the deterministic design of the breakwater crest elevations.

It should be noted that the Pf values for berm recession (in Table 6) would be less if a wider berm were applied according to (Van der Meer and Sigurdarson, 2016) recommendation based on the resiliency factor (P%). Similarly, if the remaining berm width was considered smaller than $4D_{n50}$, the *Pf* would be increased.

Applying different limit state functions, design criteria, breakwater types, and other areas with varying environmental uncertainties can alter the results presented above. For example, the required armor weights are typically determined using the predicted mean values without a safety margin in the deterministic design of conventional rubble mound breakwaters. As a result, the *Pf* determined for the berm breakwaters would be less than their corresponding *Pf*. In other words, based to existing deterministic criteria, a designed berm breakwater is typically more dependable than a designed conventional breakwater. In conclusion, a probabilistic design provides information about the probability of failure, while a deterministic design does not. Furthermore, in the case of probabilistic design, it is possible to introduce different target Pf values for different failure mechanisms. Designers can use it to investigate the reliability index of an existing structure, design a new structure based on the desired probability of failure, and account for all the uncertainties.

The results shows that the effect of dependency structures on the calculated Pf is much less than the effect of the types of the berm breakwater. However, the independent condition results in smaller Pf values in general for both the recession and overtopping failure modes. It means that neglecting the correlations between input variables leads to underestimated designed sections and it is necessary to include the dependency structures for a safe design.

Table 6. Probability of failure for the deterministic designed sections

Failure	Dependency Structures	HR	PR	FR
		Pf	Pf	Pf
Berm recession	Gumbel	3.73E-02	1.14E-01	2.12E-01
	Gaussian	3.47E-02	1.14E-01	2.15E-01
	D-Vine	3.88E-02	1.16E-01	2.13E-01
	Independent	2.58E-02	9.85E-02	1.99E-01
Wave Overtopping	Gumbel	3.03E-01	3.09E-01	2.76E-01
	Gaussian	3.05E-01	3.11E-01	2.77E-01
	D-Vine	3.04E-01	3.09E-01	2.80E-01
	Independent	2.94E-01	3.00E-01	2.57E-01

6. Conclusions

By focusing on a berm breakwater on Iran's southern coast, this study examines the reliability of different berm breakwaters. The measurements in this region were used to extract the environmental data. The D-Vine structure was determined to be the most appropriate one based on the statistical indicators after different dependency structures between the input variables were studied to identify their importance on the results. Reliability of these structures was calculated following the design of different berm breakwater types using the deterministic methods currently in use. Two failure modes, such as wave overtopping and berm recession, were used for this. Dependency structures and the effects on different breakwater types were considered. Based on the results, the main conclusions are outlined below.

• In order assist designers achieve adequate berm widths that align with the required probability of failure, two deterministic design concepts were presented in this paper. While the second concept introduces a resiliency factor, the first concept involves a predetermined number extra armor units. In general, the proposed design values by Van der Meer

and Sigurdarson, 2016 is much more conservative than using extra armor units as PIANC's recommendations.

• Because HR breakwaters have larger armor units and smaller berm recessions than the other two types, they have a lower probability of berm failure among the other types of berm breakwaters. However, the Pf for overtopping failure mode is almost the same for all types of berm beakwaters. In addition, the Pf due to overtopping failure mode is generally less than the pf values for berm recession criterion.

• In the studied area, dependency structures between the input variables had a generally insignificant impact on the calculated Pf values. Neglecting the dependencies, however, can result in an underestimated design for regions where wave height and water level have a strong positive correlation. This is especially true for the breakwater crest elevation, which depends on the water level and wave height that coincide. In addition, among the various dependency structures examined, the D-Vine structure turned out to be the most accurate. For both limit state functions, the independent assumption was associated to the maximum error. This result emphasizes how crucial it is to consider variable dependencies into account in specific situations in order to ensure accurate and reliable breakwater designs.

• The results show that, compared to conventional rubble mound breakwaters, the current criteria for the deterministic design of berm breakwaters are notably conservative. The primary cause of this result is the use of an additional berm width as a function of Dn50.

8. References

[1] J. Juhl and O. J. Jensen, "Berm breakwater structures: Features of berm breakwaters and practical experience," in *Proceedings Second Workshop MAST2, Imperial College, 6 October 1995 (Paper)*, Imperial College, 1995.

[2] H. Akbari, A. A. Karami Matin, and M. Shafieefar, "The effect of sequential storms on the performance of homogeneous berm breakwaters," *Coastal Engineering*, vol. 175, p. 104141, 2022, doi: https://doi.org/10.1016/j.coastaleng.2022.104141.

[3] T. L. Andersen, M. N. Moghim, and H. F. Burcharth, "Revised recession of reshaping berm breakwaters," *Coastal Engineering*, p. 2, 2014.

[4] T. L. Andersen and H. F. Burcharth, "A new formula for front slope recession of berm breakwaters," *Coastal engineering*, vol. 57, no. 4, pp. 359–374, 2010.

[5] T. G. Andersen and O. Bondarenko, "Reflecting on the VPIN dispute," *Journal of Financial Markets*, vol. 17, pp. 53–64, 2014, doi: https://doi.org/10.1016/j.finmar.2013.08.002.

[6] K. R. Hall and J. S. Kao, "A study of the stability of dynamically stable breakwaters," *Canadian Journal of Civil Engineering*, vol. 18, no. 6, pp. 916–925, Dec. 1991, doi: 10.1139/l91-113.

[7] T. Lykke Andersen, "Hydraulic Response of Rubble Mound Breakwaters: scale effects-berm breakwaters," Aalborg University, 2006.

[8] M. N. Moghim and F. Alizadeh, "Hydraulic stability of reshaping berm breakwaters using the wave momentum flux parameter," *Coastal Engineering*, vol. 83, pp. 56–64, 2014, doi: https://doi.org/10.1016/j.coastaleng.2013.10.008.

[9] M. N. Moghim, M. Shafieefar, A. Tørum, and V. Chegini, "A new formula for the sea state and structural parameters influencing the stability of homogeneous reshaping berm breakwaters," *Coastal Engineering*, vol. 58, no. 8, pp. 706–721, 2011, doi: https://doi.org/10.1016/j.coastaleng.2011.03.006.

[10] A. Sadat Hosseini and M. Shafieefar, "Estimation of Reshaped Profile of Berm Breakwaters Using Experimental Data," *International Journal of Maritime Technology*, vol. 2, pp. 55–65, 2014.

[11] A. Sadat Hosseini, A. Kabiri, A. H. Gandomi, and M. Shafieefar, "Genetic programming for the prediction of berm breakwaters recession," *Ocean Engineering*, vol. 279, p. 114465, 2023, doi: https://doi.org/10.1016/j.oceaneng.2023.114465.

[12] M. R. Shekari and M. Shafieefar, "An experimental study on the reshaping of berm breakwaters under irregular wave attacks," *Applied Ocean Research*, vol. 42, pp. 16–23, 2013, doi: https://doi.org/10.1016/j.apor.2013.03.007.

[13] M. Shafieefar and M. R. Shekari, "An experimental study on the parameterization of reshaped seaward profile of berm breakwaters," *Coastal Engineering*, vol. 91, pp. 123–139, 2014, doi: https://doi.org/10.1016/j.coastaleng.2014.05.009.

[14] M. Shafieefar, M. R. Shekari, and B. Hofland, "Influence of toe berm geometry on stability of reshaping berm breakwaters," *Coastal Engineering*, vol. 157, p. 103636, 2020, doi: https://doi.org/10.1016/j.coastaleng.2020.103636.

[15] M. R. Shekari and M. Shafieefar, "An experimental study on the reshaping of berm breakwaters under irregular wave attacks,"

Applied ocean research, vol. 42, pp. 16–23, 2013.

[16] J. Van der Meer and S. Sigurdarson, *Design and construction of berm breakwaters*, vol. 40. World scientific, 2016.

[17] S. Sigurdarson, J. van der Meer, H. Burcharth, and J. Sørensen, *Optimum Safety Levels and Design Rules for the Icelandic-type Berm Breakwater*. 2007. doi: 10.1142/9789814282024_0005.

[18] S. Sigurdarson, J. W. van der Meer, A. T?rum, and R. Tomasicchio, "BERM RECESSION OF THE ICELANDIC-TYPE BERM BREAKWATER," in *Coastal Engineering 2008*, World Scientific Publishing Company, 2009, pp. 3311–3323. doi: doi:10.1142/9789814277426_0274.

[19] A. Tørum, "On the Stability of Berm Breakwaters in Shallow and Deep Water," in *Coastal Engineering 1998*, 1998, pp. 1435–1448. doi: 10.1061/9780784404119.106.

[20] A. Tørum, S. R. Krogh, and S. Fjeld, "Berm breakwaters: Stone breaking strength," *J Waterw Port Coast Ocean Eng*, vol. 128, no. 4, pp. 163–172, 2002.

[21] A. Tørum, F. Kuhnen, and A. Menze, "On berm breakwaters. Stability, scour, overtopping," *Coastal Engineering*, vol. 49, no. 3, pp. 209–238, 2003, doi: https://doi.org/10.1016/S0378-3839(03)00062-0.

[22] J. W. Van der Meer and K. W. Pilarczyk, "Stability of rubble mound slopes under random wave attack," in *Coastal Engineering 1984*, 1984, pp. 2620–2634.

[23] J. W. Van der Meer, "Rock slopes and gravel beaches under wave attack.," 1990.

[24] M. Ehsani, M. N. Moghim, and M. Shafieefar, "An experimental study on the hydraulic stability of Icelandic-Type berm breakwaters," *Coastal Engineering*, vol. 156, p. 103599, 2020, doi: https://doi.org/10.1016/j.coastaleng.2019.103599.

[25] H. F. Burcharth *et al.*, *State-of-the-art of Designing and Constructing Berm Breakwaters*. PIANC General Secretariat, 2003.

[26] CEM, *Coastal Engineering Manual*. US Army Corps of Engineers, 2006.

[27] R. E. Moghadam, M. Shafieefar, and H. Akbari, "A probabilistic approach to predict wave force on a caisson breakwater based on Bayesian regression and experimental data," *Ocean Engineering*, vol. 249, p. 110945, 2022.

[28] R. Ehsani Moghadam, M. Shafieefar, and H. Akbari, "Reliability-Based Analysis of a Caisson Breakwater with the Application of Bayesian Inference," *Journal of Marine Science and Application*, vol. 20, no. 4, pp. 735–750, 2021.

[29] D. Lucio, J. L. Lara, A. Tomás, and I. J. Losada, "Projecting compound wave and sea-level events at a coastal structure site under climate change," *Coastal Engineering*, vol. 189, p. 104490, 2024, doi: https://doi.org/10.1016/j.coastaleng.2024.104490.

[30] J. Jo, S. Kim, N. Mori, and H. Mase, "Combined storm surge and wave overtopping inundation based on fully coupled storm surge-wave-tide model," *Coastal Engineering*, vol. 189, p. 104448, 2024, doi: https://doi.org/10.1016/j.coastaleng.2023.104448.

[31] P. Mares-Nasarre, M. R. A. van Gent, and O. Morales-Nápoles, "A copula-based model to describe the uncertainty of overtopping variables on mound breakwaters," *Coastal Engineering*, vol. 189, p. 104483, 2024, doi: https://doi.org/10.1016/j.coastaleng.2024.104483.

[32] S. Radfar, M. Shafieefar, and H. Akbari, "Impact of copula model selection on reliability-based design optimization of a rubble mound breakwater," *Ocean Engineering*, vol. 260, p. 112023, 2022.

[33] P. Zarbipour and H. Akbari, "Reliability design of seawater desalination outfalls based on a novel probabilistic environmental assessment," *Ocean Engineering*, vol. 313, p. 119465, 2024, doi: https://doi.org/10.1016/j.oceaneng.2024.119465.

[34] Y. Zhang, M. Beer, and S. T. Quek, "Long-term performance assessment and design of offshore structures," *Comput Struct*, vol. 154, pp. 101–115, 2015.

[35] O. Aghatise, F. Khan, and S. Ahmed, "Reliability assessment of marine structures considering multidimensional dependency of the variables," *Ocean Engineering*, vol. 230, p. 109021, 2021.

[36] Y. Zhao and S. Dong, "Design loads and reliability assessment of marine structures considering statistical models of metocean data," *Ocean Engineering*, vol. 241, p. 110099, 2021.

[37] M. Adibzade, M. Shafieefar, H. Akbari, and R. Panahi, "Multi-peaked directional wave spectra based on extensive field measurement data in the Gulf of Oman," *Ocean Engineering*, vol. 230, p. 109057, 2021, doi: https://doi.org/10.1016/j.oceaneng.2021.109057.

[38] H. Akbari, R. Panahi, and L. Amani, "A double-peaked spectrum for the northern parts of the Gulf of Oman: Revisiting extensive field measurement data by new calibration methods," *Ocean Engineering*, vol. 180, pp. 187–198, 2019, doi: https://doi.org/10.1016/j.oceaneng.2019.03.060.

[39] H. Akbari, R. Panahi, and L. Amani, "Improvement of double-peaked spectra: Revisiting the combination of the Gaussian and the JONSWAP models," *Ocean Engineering*, vol. 198, p. 106965, 2020.

[40] K. Koohestani, M. N. Allahdadi, and N. Chaichitehrani, "Oceanic Response to Tropical Cyclone Gonu (2007) in the Gulf of Oman and the Northern Arabian Sea: Estimating Depth of the Mixed Layer Using Satellite SST and Climatological Data," *J Mar Sci Eng*, vol. 9, no. 11, p. 1244, 2021.

[41] Z. Ranji and M. Soltanpour, "Optimization of bottom friction coefficient using inverse modeling in the Persian Gulf," *Ocean Science Journal*, vol. 56, pp. 331–343, 2021.

[42] A. Rezaee Mazyak and A. Hajmomeni, "Numerical Modeling of the Storm Surge of NANAUK and ASHOOBA Tropical Cyclones in the Makran Coasts," *Journal Of Marine Engineering*, vol. 17, no. 34, pp. 13–24, 2021.

[43] P. Zarbipour, "Probabilistic evaluation of effluent discharge performance in desalinations," Master of Science (M.Sc.) thesis in Coasts, Ports and Marine Structural Engineering, Tarbiat Modares University, Tehran, Iran, 2023. doi: http://dx.doi.org/10.13140/RG.2.2.15378.02244.

[44] R. B. Nelsen, *An introduction to copulas*. Springer, 2006.

[45] S. Sellés Valls, "A vine-based approach for defining critical infrastructure loads: Designing a breakwater in Galveston Bay, Texas," 2019.

[46] J. Van der Meer and et al., *Manual on wave overtopping of sea defences and related structures*. 2018. [Online]. Available: http://www.overtopping-manual.com

[47] C. Castillo, R. Mínguez, E. Castillo, and M. A. Losada, "An optimal engineering design method with failure rate constraints and sensitivity analysis. Application to composite breakwaters," *Coastal Engineering*, vol. 53, no. 1, pp. 1–25, 2006.

[48] S. Radfar, M. Shafieefar, H. Akbari, P. A. Galiatsatou, and A. R. Mazyak, "Design of a rubble mound breakwater under the combined effect of wave heights and water levels, under present and future climate conditions," *Applied Ocean Research*, vol. 112, p. 102711, 2021.

[49] Zarbipour, P., Akbari, H., & Nikoo, M. R. (2026). Quantum machine learning for wave overtopping estimation: Integrating with causal inference and uncertainty quantification. Ocean Engineering, 343, 123482. https://doi.org/10.1016/j.oceaneng.2025.123482

INTERNATIONAL JOURNAL OF
COASTAL, OFFSHORE & ENVIRONMENTAL ENGINEERING IJCOE Vol.11/No. 2/Spring 2026 (49-57)

Available online at: www. Ijcoe.org

Tidal Datum Transfer in Shallow Waters: A Comparison of Classical and Parametric Methods in the Northern Persian Gulf

Hamed Esmaeil Nazari[1], Abbas Abedini[1*], Bahman Tajfirooz[2]

[1] School of Surveying and Geospatial Engineering, College of Engineering, University of Tehran, Tehran, Iran; hamednazari.1379@ut.ac.ir, aabedeni@ut.ac.ir*
[2]Darya Tarsim Consulting Engineer Co., Tehran, Iran; bahman.tajfirooz@gmail.com

ARTICLE INFO

Article History:
Received 30 Jul 2025
Accepted 10 Dec 2025

Keywords:
Tidal Datum Transfer
Range-Ratio Method
Least-Squares
Grant's Method
Moving-Window Analysis
Hydrography

ABSTRACT

Accurate tidal datum transfer is crucial in hydrographic surveying and coastal engineering, particularly in regions characterized by complex tidal regimes. This study evaluates the performance of tidal datum transfer methods in a mixed semi-diurnal environment using simultaneous water level observations from a reference and a secondary station situated in the Persian Gulf and Strait of Hormuz. This specific area was selected due to its unique hydrodynamic conditions, shallow bathymetry, and significant non-linear tidal interactions that complicate conventional datum establishment. The classical Range-Ratio approach is systematically compared against Grant's parametric least-squares method, which mathematically estimates a scale factor, a time shift, and a datum shift by fitting the continuous tidal curve. To assess the robustness, accuracy, and sensitivity of these methods to observation lengths, a moving-window analysis was implemented over record lengths of 0.5, 1, 3, 7, and 15 days using 10-minute shift steps. Initial harmonic analysis of the observed data yielded form factor values of 0.38 and 0.43, confirming a mixed, predominantly semi-diurnal regime that theoretically satisfies the prerequisites for applying the Range-Ratio method. However, evaluation based on the Root Mean Square Error (RMSE) across all tested windows demonstrated that the parametric least-squares method is significantly more stable and reliable. By utilizing the entire continuous record rather than discrete data points, Grant's method mitigates the inherent limitations of the classical approach, which relies solely on a limited number of high and low water extrema and remains highly sensitive to short-term meteorological noise and shallow-water effects. Ultimately, the findings strongly advocate adopting continuous curve-fitting techniques combined with moving-window analyses for precise hydrographic datum transfers in complex coastal basins.

1. Introduction

Tidal datums form the foundation of hydrographic and coastal engineering activities. They serve as reference surfaces from which depths are measured and coastal boundaries are delineated [1]. These vertical reference planes, defined by tidal stages such as high water, low water, or mean sea level, provide the essential framework for safe navigation, coastal zone management, and maritime boundary delimitation [2]. The accurate determination of tidal datums carries significant legal implications, particularly in regions where the boundary between state and private ownership is defined by tidal water levels [3]. As Marmer [4] noted in his seminal work, the relationship between these reference surfaces and adjacent coastal land affects both navigation safety and coastal property rights.

From a practical perspective, the reliable realization of these reference planes requires long-term observations spanning a full nineteen-year National Tidal Datum Epoch to account for all astronomical periodicities affecting tidal variations [5]. However, such extended observation periods are rarely feasible for hydrographic surveys or coastal engineering projects. This practical consideration has motivated the development of various techniques collectively known as tidal datum transfers, which enable the estimation of datum elevations at a secondary site using short- to medium-term observations in conjunction with data from a reference station where the datum is already

established [6]. Among these, the Range-Ratio method has emerged as the most widely adopted approach in hydrographic practice worldwide [7]. This method assumes that the ratio of vertical distances from respective datum planes to mean water level at the secondary and reference sites equals the ratio of their tidal ranges, offering conceptual simplicity and ease of implementation.

However, the performance of datum transfer methods varies considerably depending on the tidal characteristics of a region. Areas with mixed tides, pronounced diurnal inequalities, or significant spatial variations in tidal ranges present particular challenges for conventional approaches. The Range-Ratio method, which primarily relies on extremal tidal values, utilizes only a fraction of the available observational data and may inadequately capture the full complexity of the tidal signal [8]. This limitation becomes particularly evident in locations where the ratio between diurnal and semi-diurnal constituents varies spatially or where rapid changes in tidal range occur over short distances.

An alternative parametric approach based on least-squares estimation was proposed by Grant and O'Reilly [9] to address these limitations. Their method simultaneously determines three critical parameters: a vertical scale factor, a horizontal time shift, and a vertical datum shift. This approach effectively slides the reference station tidal curve along the time axis, translates it vertically, and stretches it to achieve optimal superposition with secondary station observations. By utilizing all available observational data rather than just extremal values, the method provides statistical indicators of parameter accuracy. The mathematical foundation rests upon the least-squares adjustment theory articulated by Vaníček and Krakiwsky [10], while practical implementation requires interpolation techniques such as cubic splines to handle discrete tidal observations [11]. This parametric framework can be interpreted as a generalized extension of the conventional Range-Ratio concept, offering enhanced flexibility for application in spatially variable tidal regimes.

The Persian Gulf provides a suitable case study for evaluating datum transfer methods under challenging tidal conditions. This semi-enclosed marginal sea, connected to the Gulf of Oman through the narrow Strait of Hormuz, exhibits dynamically diverse tidal characteristics shaped by interactions between astronomical forcing, basin geometry, and bathymetric features [12]. Pous et al. [13] demonstrated that tidal impacts on volume and salt transport through the Strait of Hormuz play a crucial role in determining circulation patterns throughout the Gulf. The tidal characteristics of this region show considerable spatial heterogeneity, with semi-diurnal constituents displaying strong variations across the Strait, while diurnal constituents exhibit sensitivity to seasonal oceanographic conditions [13]. The relative contributions of these constituents determine the overall tidal regime classification for any particular location.

Within this broader regional context, the Hormuz Strait represents one of the most hydrodynamically active areas of the Persian Gulf. Located between Qeshm Island and the Iranian mainland, this waterway is characterized by extensive mangrove forests designated as a protected area since 1972 [14]. The region hosts several major ports including Bandar Shahid Rajaee, which serves as one of Iran's primary commercial gateways. Previous modeling studies in this area have demonstrated tidal ranges of approximately three meters along the northern coast of Qeshm Island, reaching up to four and a half meters in adjacent areas, classifying the region as mesotidal to macrotidal [15]. The heterogeneous bathymetry of the channel influences tidal phase and amplitude propagation, generating current patterns that may affect the performance of datum transfer methods.

The geographical location of the study area and the positions of the two tide gauge stations are illustrated in Figure 1.

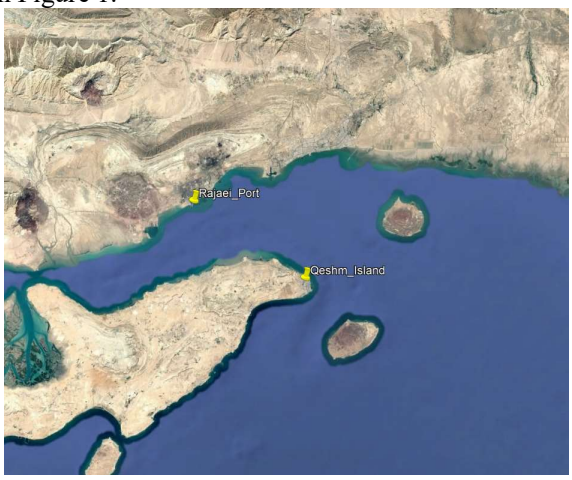

Figure 1. Location of the study area in the northern Persian Gulf, showing Bandar Shahid Rajaee and the Qeshm Island tide gauge station.

Previous investigations have well-established the baseline tidal characteristics of the region. Comprehensive tide and circulation studies, notably by Pous et al. [13], have identified the major tidal constituents and their spatial distribution throughout the Persian Gulf. These analyses confirm the predominance of semi-diurnal constituents across the region while noting significant local variations. Collectively, these investigations indicate that the tidal regime in the vicinity of the Strait of Hormuz exhibits mixed, mainly semi-diurnal characteristics, with the relative influence of diurnal and semi-diurnal constituents varying spatially depending on the exact bathymetry and location [13].

However, little comparative work has been done on datum transfer methods under northern Persian Gulf tidal conditions [16]. While the theoretical advantages of parametric least-squares approaches have been demonstrated in other regions, their practical efficacy in the spatially heterogeneous tidal environment of the Strait of Hormuz remains largely unexplored. Furthermore, the availability of three months of high-temporal-resolution radar tide gauge observations from Bandar Shahid Rajaee and a nearby station on Qeshm Island, together with complete harmonic analysis and independently established ground truth datum information, allows a systematic comparison of the methods.

Accordingly, the present study is structured around the following objectives: first, characterization of the tidal regime at both stations through form factor determination and harmonic analysis; second, implementation of both the conventional Range-Ratio method and the least-squares parametric approach using identical observational data; third, quantitative comparison of method performance against ground truth datum elevations; and fourth, assessment of method sensitivity to prevailing tidal conditions. The findings may help guide datum realization strategies in mesotidal mixed regimes and provide guidance for hydrographers operating in the Persian Gulf.

2. Theory of Problem

The accurate transfer of a tidal datum from a well-established reference station to a temporary secondary station relies on mathematical models that capture the relationship between the tidal dynamics at both locations. In this study, two distinct methodologies are evaluated: the conventional Range-Ratio method and a parametric least-squares approach.

2.1. Conventional Range-Ratio Method

The conventional Range-Ratio method is a well-established empirical technique used to transfer a vertical datum from a reference (primary) station to a newly established secondary station. The fundamental assumption of this method is that the ratio of the vertical distance between the datum and the mean water level at the secondary station to the corresponding distance at the reference station is equal to the ratio of their respective tidal ranges.

Mathematically, this relationship is expressed by the following principal equation:

$$d = m' - M'(\frac{r}{R}) \qquad (۱)$$

where:

d represents the unknown datum offset (relative to the mean water level) at the secondary station.

m' is the mean water level calculated at the secondary station over the simultaneous observation period.

M' is the mean water level at the primary reference station over the same period.

r is the mean tidal range at the secondary station.

R is the mean tidal range at the primary reference station.

To implement this method, the high and low water extrema must be explicitly extracted from the tidal records of both stations. The mean values of these specific extrema are then used to calculate the tidal ranges (r and R) and the mean water levels (m' and M'). While computationally straightforward, this approach relies exclusively on discrete peak and trough values, making the final datum calculation (d) highly sensitive to any high-frequency noise or meteorological disturbances occurring exactly at the times of high or low water.

2.2. Parametric Least-Squares Method (Grant's Method)

To overcome the limitations of the discrete extrema-based approach, Grant and O'Reilly [9] proposed a continuous parametric model. This method utilizes the entire simultaneous time-series dataset from both stations. The fundamental concept is to geometrically transform the reference station's tidal curve by scaling it vertically, shifting it in time, and translating it vertically to optimally align it with the secondary station's tidal curve.

The mathematical model expressing the secondary tidal height, $H(t)$, as a function of the reference tidal height, $G(t)$, at any given time t is formulated as:

$$H(t) = a.G(t + b) + c \qquad (۲)$$

In this formulation:

a represents the vertical scale factor (analogous to the range ratio).

b is the horizontal time shift, representing the phase difference between the stations.

c is the vertical datum shift.

To determine the optimal parameters (a, b, and c), the method employs the principle of least-squares estimation [10]. The objective is to minimize the sum of the squared residuals between the observed secondary water levels and the transformed reference curve. The residual function $v(t)$ is defined as:

$$v(t) = H(t) - [a.G(t + b) + c] \qquad (۳)$$

The objective function to be minimized over N simultaneous observations is:

$$J(a, b, c) = \sum_{i=1}^{N} (H(t_i) - [a.G(t_i + b) + c])^2 \qquad (۴)$$

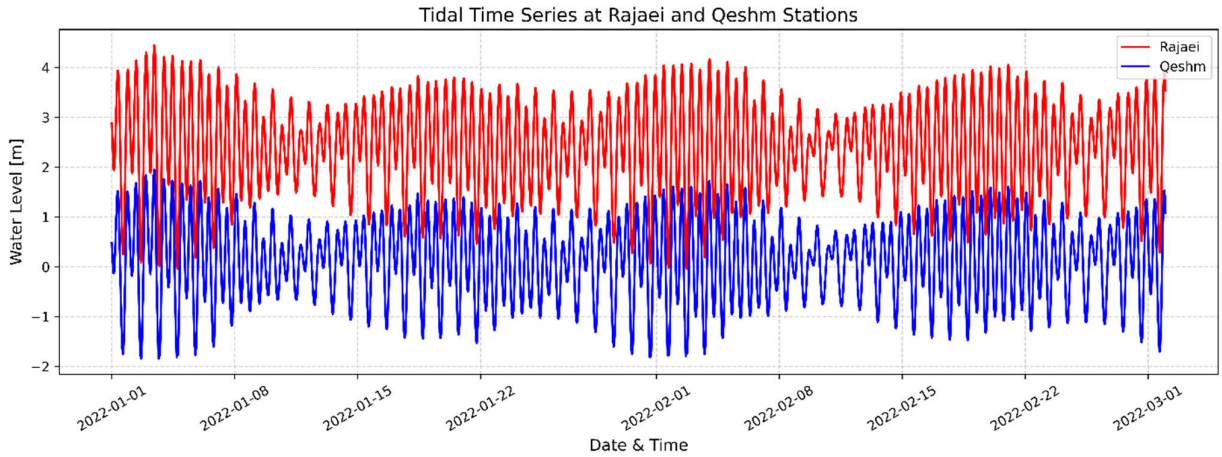

Figure 2. Raw tidal records from the Shahid Rajaei (reference) and Qeshm (secondary) radar tide-gauge stations.

Because the time shift parameter b is continuous whereas the recorded tidal observations $G(t_i)$ are discrete, $G(t_i + b)$ cannot be directly extracted from the raw data. To resolve this, cubic spline interpolation is applied to the reference station data, providing a smooth and continuous mathematical representation of the reference tidal curve [9, 11].

since the function $G(t_i + b)$ is generally non-linear with respect to the time shift parameter b, the least-squares optimization is a non-linear problem. It requires linearization using Taylor series expansion and is solved iteratively. The iterative process typically commences with initial approximations of $a_0 = 1$, $b_0 = 0$, and $c_0 = 0$, converging towards the optimal parameter set that defines the datum shift c [9].

2.3. Influence of Tidal Regimes and Form Factor

The reliability and accuracy of datum transfer methods are strongly influenced by the characteristics of the local tidal regime. Tidal types are quantitatively classified using the Form Factor (F), defined as the ratio of the sum of the amplitudes of the primary diurnal harmonic constituents ($K1$ and $O1$) to the sum of the primary semi-diurnal constituents ($M2$ and $S2$):

$$F = \frac{O1 + K1}{M2 + S2} \qquad (۵)$$

Based on the value of F, tidal regimes are categorized into four groups: semi-diurnal ($F < 0.25$), mixed predominantly semi-diurnal ($0.25 \leq F \leq 0.5$), mixed predominantly diurnal ($1.5 < F \leq 3$), and diurnal ($F > 3$).

The standard equations for the conventional Range-Ratio method, as described in Section 2.1, are fundamentally predicated on the occurrence of two regular and distinct high and low waters per tidal day. Therefore, these specific formulations are mathematically valid and practically applicable primarily in semi-diurnal and mixed predominantly semi-diurnal regimes ($F \leq 1.5$). In mixed predominantly diurnal or fully diurnal regimes ($F >$ 3), pronounced diurnal inequalities occur. Secondary extrema can become masked or completely vanish due to shallow-water effects or specific astronomical alignments (e.g., neap tides). When these essential extrema are missing or ambiguous, the fundamental assumptions of the standard Range-Ratio method break down, rendering it mathematically unstable or inapplicable without complex modifications.

Conversely, because the parametric least-squares approach (Grant's method) utilizes the continuous water level curve rather than relying on discrete extrema, it is not bounded by the requirement of a specific tidal form factor. It remains mathematically robust and operationally viable across all types of tidal regimes, making it particularly advantageous in complex coastal environments.

3. Experimental Investigations

3.1. Study Area and Data Acquisition

To evaluate the performance and temporal stability of the datum transfer methods, continuous water level datasets from coastal stations located in the northern coast of the Persian Gulf were utilized. For the purpose of this analysis, Shahid Rajaei was designated as the primary (reference) station, while Qeshm Island served as the secondary (subordinate) station. The geographical distribution and relative positions of these stations are illustrated in Figure 1.

The water level observations span a period of two month, from 1/1/2022 to 3/1/2022, with a sampling interval of 10 minutes. The data were provided by Darya Tarsim Company. The comprehensive metadata for each station, including geographical coordinates, mean sea level relative to the local benchmark, and basic data specifications, are summarized in Table 1.

3.2. Tidal Characteristics and Form Factor Validation

As discussed in Section 2.3, the validity of the standard Range-Ratio method depends on the presence of a semi-diurnal or mixed predominantly semi-diurnal tidal regime. To validate this prerequisite

for our chosen datasets, the eight primary harmonic constituents were extracted for each station.

Table 1. Station metadata and water level data specifications.

Specification	Reference Station	Secondary Station
Station Name	Bandar Shahid Rajaee	Qeshm Island
Coordinates	۲۷°۰۵′ N, 56°03′ E	26°57′ N, 56°16′ E
Observation Period	2 Months (Simultaneous)	
Sampling Interval	10 Minutes	
Ground Truth (Chart Datum)	−1.84 m (below MSL)	--

The amplitudes of these constituents and the resulting Form Factor (F) for each station are presented in Table 2.

As shown in Table 2, the calculated Form Factors for all stations are well below the 1.5 threshold ($F \leq 1.5$). This confirms that the tidal regimes are indeed mixed predominantly semi-diurnal, meaning distinct, regular high and low waters occur. Consequently, the fundamental conditions for applying the classical Range-Ratio method are satisfied, establishing a valid and fair baseline for comparing its performance against Grant's parametric approach.

3.3. The Moving Window Methodology

A rigorous evaluation of a datum transfer method requires assessing its sensitivity to the chosen observation period and its robustness against short-term environmental noise. To quantify the temporal stability of the estimated datums, a "moving window" algorithm was implemented.

The moving window technique operates by extracting a continuous subset of data (the window) of length W from the total available time series of length T_{total}. The chosen datum transfer algorithm is applied to this specific window to calculate a single datum difference estimate. Subsequently, the window is shifted forward in time by a constant step size, Δt, and the calculation is repeated. This iterative process continues until the moving window reaches the end of the available dataset.

The total number of independent datum estimates, k, generated for a given window length is determined by:

$$k = \left\lfloor \frac{T_{total} - W}{\Delta t} \right\rfloor + 1 \qquad (۸)$$

where $\lfloor \cdot \rfloor$ denotes the floor function. For the conventional Range-Ratio method, the window length must be sufficient to capture at least seven consecutive tidal extrema. In contrast, Grant's method can process the entire continuous curve regardless of extrema, allowing for the evaluation of various window lengths $W =$ 0.5, 1, 3, 7 or 15 days. In this study, the shift step was set to $\Delta t = 10\ min$ to provide a high-resolution temporal profile.

Table 2. Amplitudes of primary tidal constituents and the calculated Form Factor (F) for the study stations.

Constituent	Bandar Shahid Rajaee		Qeshm Island		Difference
	Amplitude (cm)	Phase (°)	Amplitude (cm)	Phase (°)	Phase (°)
M2	110.34	300.33	93.47	294.86	-5.47
S2	42.55	338.92	35.57	332.35	-6.57
K1	35.51	67.96	33.93	65.33	-2.63
O1	22.97	56.54	21.86	54.97	-1.57
N2	26.47	279.38	22.63	274.86	-4.52
K2	12.12	332.26	9.85	327.69	-4.57
P1	11.21	64.6	10.69	59.2	-5.4
Q1	5.03	51.04	4.83	50.67	-0.37
Form Factor and Tidal Regime Classification					
K_1+O_1	58.48		55.79		
M_2+S_2	152.89		129.04		
Form Factor	0.38		0.43		
Regime Type	Mixed, mainly semi-diurnal		Mixed, mainly semi-diurnal		

4. Results and Discussion

4.1. Visual Implementation of the Transfer Models

To illustrate the operational differences between the two methods, we examine their specific interaction with the water level datasets. For the conventional Range-Ratio method, the computational algorithm dictates the precise identification of high and low

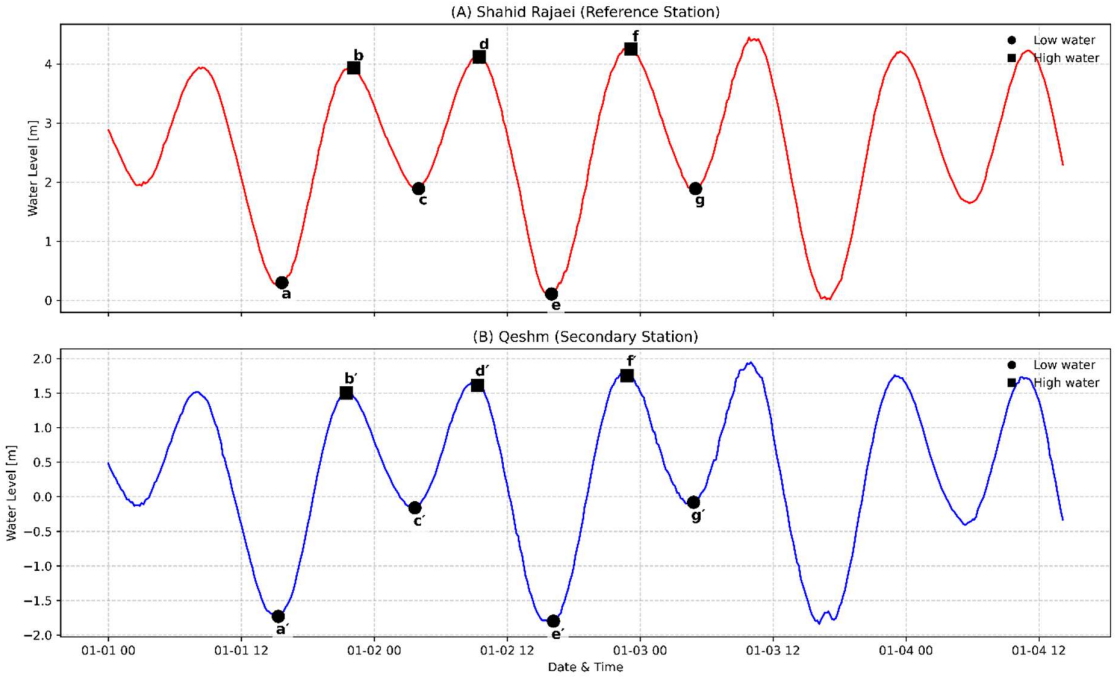

Figure 3. Identification of high and low water extrema required for the classical Range-Ratio method at both primary and secondary stations.

water extrema. Figure 3 demonstrates this process for a sample period. Only these discrete points (marked on the curves) are utilized in calculating the mean ranges and the range ratio. This visual representation highlights the method's inherent vulnerability: any localized disturbance or measurement noise occurring exactly at these extrema points will directly distort the final datum calculation.

In contrast, Figure 4 illustrates the application of Grant's parametric least-squares method over the same sample period. The upper panel shows the data points alongside the continuous fitted mathematical

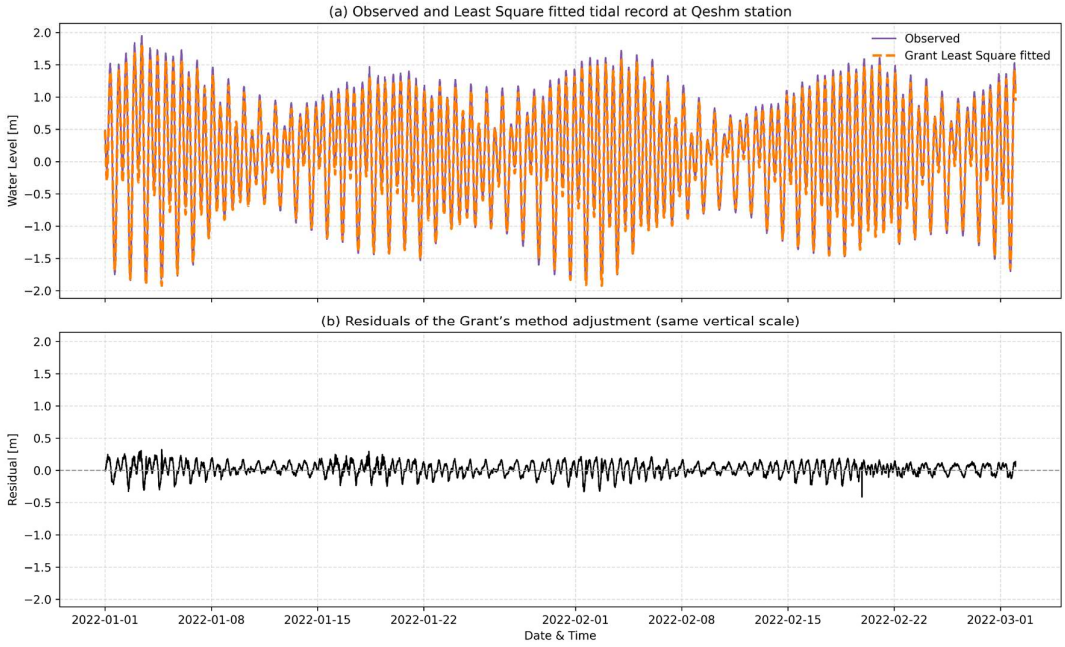

Figure 4. Application of Grant's method. Top panel: Data points and the fitted continuous curve. Bottom panel: Residuals demonstrating the goodness-of-fit.

model $H(t) = a.G(t + b) + c$. Instead of isolating extrema, the method utilizes all available data points within the window, effectively acting as a curve-fitting filter. The lower panel displays the residuals (the difference between the raw data and the fitted curve). The random distribution and small magnitude of these residuals confirm a good fit and the model's ability to successfully separate the dominant tidal signal from high-frequency environmental noise.

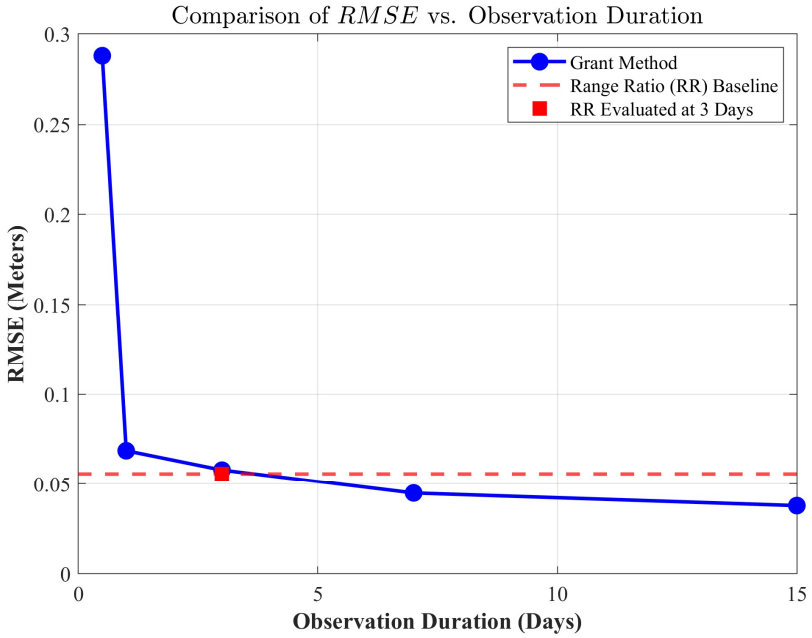

Figure 5. The trend of RMSE for Grant's method over varying window lengths, compared to the Range-Ratio baseline.

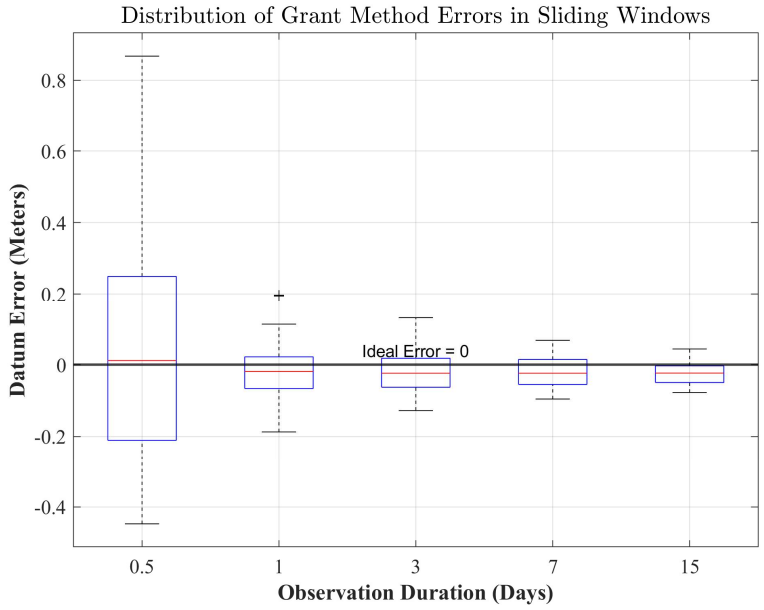

Figure 6. Boxplot illustrating the distribution and variance of datum transfer errors for the evaluated methods.

4.2. Temporal Stability and Statistical Analysis

To quantitatively evaluate the temporal stability, the moving window algorithm (Section 3.3) was applied. The performance was assessed by tracking the Root Mean Square Error (RMSE) and the statistical distribution of the datum differences.

Figure 5 presents the trend of the RMSE for Grant's method as a function of the observation window length, compared against the baseline established by the 3-day Range-Ratio method.

As shown in Figure 5, even at shorter window lengths, Grant's method exhibits a lower RMSE compared to

the conventional method. In addition, as the duration of the observation window increases, the RMSE for Grant's method demonstrates a clear downward trend, indicating that longer continuous datasets significantly enhance the stability of the parametric estimation.

To further analyze the variance and the presence of outliers, a boxplot of the datum transfer errors is presented in Figure 6.

The boxplot (Figure 6) clearly shows that the Range-Ratio method possesses a much wider interquartile range and a higher number of outliers. This wide spread signifies a lack of temporal stability. Conversely, the boxes representing Grant's method are significantly more compact, confirming tighter clustering of the estimates around the true mean.

The visual findings from Figures 5 and 6 are quantitatively supported by the statistical summary in Table 3.

Table 3. Performance comparison and statistical summary of the datum transfer methods using the moving window approach.

Method	Record Length	Number of Windows	RMSE (m)
Range-Ratio	3 days	١٠٩	0.0557
Least-Square (Grant)	12 hours	119	0.2880
Least-Square (Grant)	24 hours	118	0.0686
Least-Square (Grant)	3 days	114	0.0579
Least-Square (Grant)	7 days	106	0.0448
Least-Square (Grant)	15 days	90	0.0378

4.3. Discussion

The empirical results strongly align with the theoretical expectations. Although the selected study area possesses a Form Factor of $F \leq 1.5$ (Table 2) which theoretically validates the use of the Range-Ratio equations, the operational performance of the conventional method is severely limited by its discrete nature. Relying solely on 7 to 10 points over a 3-day period makes the Range-Ratio method highly susceptible to short-term meteorological effects and random measurement errors.

Grant's method overcomes this fundamental flaw by employing a least-squares optimization over the entire continuous dataset. By utilizing hundreds of data points within the same 3-day window, the method inherently filters out non-tidal anomalies. The continuous mathematical formulation ($H(t) = a.G(t + b) + c$) ensures that the extracted datum difference (c) is robust, stable, and less dependent on the exact timing of high or low waters. Consequently, Grant's approach appears to be a more effective alternative for vertical datum transfer, even in tidal regimes well-suited for classical methods.

5. Conclusions

Accurate vertical datum transfer is a critical component of hydrographic surveying, coastal engineering, and marine navigation. In this study, the performance of the traditional Range-Ratio method was comparatively evaluated against Grant's Least-Squares methodology for tidal datum transfer between Bandar Shahid Rajaee (reference station) and Qeshm Island (subordinate station). A continuous moving-window approach was employed to rigorously evaluate the stability, accuracy, and operational viability of these models over varying record lengths.

The harmonic analysis revealed that both stations exhibit a "Mixed, mainly semi-diurnal" tidal regime with Form Factors of F=0.38 and F=0.43. While the condition of F≤1.5 theoretically validates the application of the Range-Ratio method in this region, empirical findings demonstrated its inherent operational limitations. For a standard 3-day observation period, both methods yielded almost similar accuracies; the traditional Range-Ratio method produced a Root Mean Square Error (RMSE) of 0.0557 m, while Grant's method resulted in a comparable RMSE of 0.0579 m.

However, the fundamental advantage of Grant's method over the conventional approach lies in its mathematical structure and its capability to utilize continuous datasets. The Range-Ratio method is intrinsically limited to merely 7 high and low water extrema over a 3-day period. This reliance on isolated data points not only makes the model highly susceptible to short-term meteorological noise but also restricts its potential for achieving better accuracies.

In contrast, Grant's continuous least-squares optimization model processes hundreds of continuous data points. Because it is not restricted to extrema, Grant's method allows for the inclusion of larger datasets to improve precision. By extending the observation window, the model reduces the influence of non-tidal anomalies and random measurement errors. As demonstrated, increasing the continuous data record to 15 days using Grant's method reduced the RMSE to 0.0378 m, an accuracy level not observed in the Range-Ratio results.

Based on these comprehensive empirical results, it is concluded that Grant's least-squares approach offers a more robust and flexible alternative for vertical datum transfer. While it matches the accuracy of the conventional method over short timeframes, its advantage becomes more evident from its ability to process larger continuous datasets to yield

significantly higher precision. Therefore, adopting Grant's method is may be considered for routine use for modern hydrographic applications and precise datum establishment.

Acknowledgement

The authors would like to express their sincere gratitude to Darya Tarsim Company for generously providing the hydrographic and tidal data essential for this research. Their support and cooperation significantly contributed to the successful completion of this study.

References

1. Gill, S.K. and J.R. Schultz, Tidal datums and their applications. NOAA Special Publication NOS CO-OPS, 2001. 1.
2. Cole, G.M., Water boundaries. 1997: John Wiley & Sons.
3. Bekiashev, K.A. and V.V. Serebriakov, International Hydrographic Organization (IHO), in International Marine Organizations: Essays on Structure and Activities. 1981, Springer. p. 478-485.
4. Marmer, H., Tidal Datum Planes, NOAA National Ocean Service, Special Publication No. 135, US Coast and Geodetic Survey, US Govt. Printing Office, revised ed, 1951.
5. Evans, D., et al., Computational techniques for tidal datums handbook. NOAA Special Publication NOS CO-OPS, 2003. 2.
6. Swanson, R.L., Variability of tidal datums and accuracy in determining datums from short series of observations. 1974: National Ocean Survey.
7. Bodnar, N., Estimating Accuracies Of Tidal Datums From Short Term Observations. Technical Report NOS CO-OPS 0077 1981.
8. Kowalik, Z., T. Proshutinsky, and A. Proshutinsky, Tide-tsunami interactions. Science of Tsunami Hazards, 2006. 24(4): p. 242-256.
9. Grant, S. and C. O'Reilly, A new look at Tidal Datum Transfers. The Canadian Surveyor, 1986. 40(4): p. 477-494.
10. Vanicek, P. and E.J. Krakiwsky, Geodesy: the concepts. 2015: Elsevier.
11. De Boor, C. and C. De Boor, A practical guide to splines. Vol. 27. 1978: springer New York.
12. Reynolds, R.M., Physical oceanography of the Gulf, Strait of Hormuz, and the Gulf of Oman—Results from the Mt Mitchell expedition. Marine pollution bulletin, 1993. 27: p. 35-59.
13. Pous, S., P. Lazure, and X. Carton, A model of the general circulation in the Persian Gulf and in the Strait of Hormuz: Intraseasonal to interannual variability. Continental Shelf Research, 2015. 94: p. 55-70.
14. Zahed, M.A., et al., An overview of Iranian mangrove ecosystems, northern part of the Persian Gulf and Oman Sea. Acta Ecologica Sinica, 2010. 30(4): p. 240-244.
15. Masselink, G. and A.D. Short, The effect of tide range on beach morphodynamics and morphology: a conceptual beach model. Journal of coastal research, 1993: p. 785-800.
16. Kazemi, H., A. Abedini, and B. Tajfirooz, Prediction of Tidal Current Using FVCOM Hydrodynamic Model in Khuran Strait of Persian Gulf. IJCOE 2024, 9(4); p.64-72 2024.

INTERNATIONAL JOURNAL OF
COASTAL, OFFSHORE & ENVIRONMENTAL ENGINEERING IJCOE Vol.11/No. 2/Spring 2026 (58-71)

Available online at: www. Ijcoe.org

The impact of rivers, ports, and coastal sediment transport on sediment distribution along the southern shore of the Caspian Sea

Mohammadreza Esfandiari[1], Ulrich Reza Kamalian[2*], Mohammad Babaee Malekshah[3,4]

[1] *PhD student in Coastal and Marine Structures,University of Qom, Iran, mr.esfandiari@stu.qom.ac.ir*
[2*] *Assistant Professor in Civil Engineering, University of Qom, Iran, ur.kamalian@qom.ac.ir*
[3] *Water Research Institute, Tehran, Iran,*
[4] *PhD student in coastal environmental science,University of Tehran,Iran, babaee.malekshah@ut.ac.ir*

ARTICLE INFO

Article History:
Received 22 July 2025
Accepted 14 Jan 2026

Keywords:
Caspian Sea
Sedimentology
Heavy Mineral
Sediment Cell
Littoral Drift
Downstream Erosion

ABSTRACT

The grain size distribution and mineral composition of coastal sediments vary along the shoreline and beach profiles. This variation depends on several factors, including the sources of the sediments (such as rivers), the distance from these sources, and the direction of littoral drift. Additionally, harbors and water intakes can lead to downstream erosion, which impacts the texture of the sediments. Understanding these changes is essential for comprehending littoral drift and the impact downstream from harbors and river mouths. Understanding these changes helps to better understand the littoral drift and the impact extent downstream from harbors and river mouths. This article analyzes data from 539 sediment samples taken from the southern shoreline of the Caspian Sea, across 94 beach profiles and at 6 different depths.The findings confirm a general eastward direction of littoral drift and identify a specific sediment cell (from Sefidrud to Anzali) where the littoral drift direction contradicts this overall trend. The study also reveals that the length of the eroded shoreline downstream of the Nowshahr and Amirabad harbors (which are 74 and 33 years old, respectively) measures 28 km and 14 km to the east. These results are supported by hydrographic maps at Nowshahr and satellite images indicating beach retreat at Amirabad. Furthermore, the affected shoreline near the Sefidrud River has been identified. The heavy minerals found in the studied area predominantly include magnetite, goethite, rutile, and zircon. The concentration of heavy minerals generally decreases from east to west, which aligns with the overall direction of sediment transport.

1. Introduction

The characteristics of sediment on different coasts are influenced by the properties of their sources and the processes involved in coastal sediment transport. The sediment found along various coasts differs in terms of its sedimentology and mineralogy. Engineering studies and numerical simulations take into account these differences both along the coastline and in perpendicular directions. This information also enhances our understanding of longshore sediment transport (LST) and cross-shore sediment transport (CST) patterns and also provides valuable field data for coastal engineering and environmental impact assessments of coastal structures.

Coastal sediment characteristics have long been of interest to researchers. Ward and Folk (1957), MacLaren and Bowles (1984), Van Mohtar et al. (2017), and Yang et al. (2024), conducted comprehensive analyses of the geometric parameters of grain size distribution by examining river and coastal sediments. Their findings revealed that coastal sediments become progressively finer as they move away from their source. The grain size distribution curve shifts towards finer particles, and the sorting index improves[1–4]. Friedman (1967), and Bing fu (2012), studied various sediment samples from coastlines and rivers. Their research showed that differences in transport mechanisms and sediment deposition between rivers and the sea lead to distinct patterns in grain size distribution. Specifically, the

skewness of the grain size distribution curve for river sediments skews towards coarser particles, while marine sediments, particularly in the swash zone (the area where waves break on the shore), tend to exhibit finer particles.[5,6]. Gao and Collins (1992), Shandao (2012), Yun-pin (2015), Li et al. (2018), and Wang et al. (2023), By analyzing surface sediment samples from the shallow seabed and the river, researchers identified sediment transport trends at various points in a relatively complex environment through variations in grain size distribution. They noted that this method is limited to environments where grain size characteristics do not vary significantly and irregularly over short distances.[7–11].

Wang and Ki (1997), Cheng et al. (2009), Yamashita et al. (2018), and Muhardi et al. (2022), Using several sediment samples from cross-sections, researchers investigated the differences in sorting and skewness of sediment grain size curves at coastal locations and river mouths. They also examined the profiles related to erosion, deposition, and stability[12–15]. Duc et al. (2007), and Jiang et al. (2014), The researchers analyzed grain size curves from several collected sediment samples to study sediment transport both near and far from the coast. Their study revealed that sediment distribution and transport in this area are influenced by various factors, including river currents, coastal currents, waves, and the morphological characteristics of the delta. Specifically, they found that coarser sediments are more abundant near the river mouth, while finer sediments are prevalent in areas farther from the coast and in deeper waters. Additionally, they examined how different seasons, particularly high-flow and low-flow periods, affect sediment transport patterns[16,17]. Amalan et al. (2014), Perera et al. (2023), and Wickramasooriya et al. (2024), Gradistat software analyzed sediment samples collected from the coast and sea, focusing on mineral abundance and grain size characteristics to identify suitable sand and gravel deposits for construction after sediment washing[18–20]. Timothy (2016) investigated the impact of tidal range (6.6 meters) and waves on sediment sorting and grain size within the estuary and surrounding shores of the River Tamar in southwest England, comparing 80 surface sediment samples from riverbeds and coastal areas[21]. Pham et al. (2017) and Bandari et al. (2020) investigated the origin of the sediments by using surface sediments and obtaining geometric parameters, along with conducting XRD and XRF tests to determine the mineral types[22,23].

Studies on the relationship between coastal sediment characteristics and environmental conditions have been limited along the Caspian Sea coast. Khajeh et al. (2004), and Bahador et al. (2023 Coastal sediment samples from the southern Caspian Sea were analyzed, revealing that the average grain size and quartz content of sediments decrease from the northeast to the southwest, which aligns with the prevailing winds in the region[24,25]. Lashet Nasha'i et al. (2006), comparing surface samples from the Astara coast to the eastern part of Gilan Province in the Caspian Sea, showed that the direction of D50 reduction along the coast is aligned with the transport direction of coastal sediments[26]. Khoshravan et al. (2011), and Bagheri (2016) Using surface sediments along the Caspian Sea coast, researchers examined the mineralogy and geometric parameters. The results indicated that sediments from the western and central southern coasts of the Caspian Sea mainly originate from the Sefidrud River. It was shown that in areas with abundant heavy minerals, the seabed slope in shallow waters is steep, and the beach slope is moderate. Conversely, in areas with light minerals, the seabed slope is gentler, and the beach slope is steeper. In sections with coarse-grained sediments, both the seabed and beach slopes are steep. The coasts were categorized into three types: erosional, intermediate, and actively depositional[27,28]. MirKazemian et al. (2011), using 17 sediment samples from the sandy Babolsar coast to Nour and 16 samples from the Haraz River, identified the source of sediments as the upper Azarin massifs (basalt, andesite, and diabase) transported by the Haraz River to the coast[29]. Amini et al. (2012) studied 70 sediment samples from the Miankaleh and Neka coasts, showing that sediment transport strength decreases eastward along the coast and coastal hills transition from active to inactive[30]. Kiani and Afraideh (2012) found that reduced wave energy is associated with a decrease in the average grain size. They also highlighted the impact of human activities on sediment characteristics[31].

This study analyzed around 600 surface sediment samples collected from the southern coast of the Caspian Sea. The samples were compared based on their grain size distribution and mineral composition. Additionally, the research examined the effects of rivers, harbors, and other marine structures on the adjacent coastlines.

2. The study area

The research was conducted on the southern (Iranian) coast of the Caspian Sea, which has a shoreline length of 740 kilometers. This area is a remnant of the ancient Tethys Ocean surrounded by mountains formed from Late Miocene-Pliocene tectonic activity. Coastal sediments in the Caspian Sea are primarily influenced by river inputs, coastal erosion, wind transport, and biological processes. The mineral composition of the sediments is influenced by mountain erosion, river sediment transport, nearshore currents, and human activities. In recent decades, the Caspian Sea has faced significant challenges, including rapid water level decline, unsustainable development, sand extraction from the beach, and destruction of coastal habitats (see Fig. 1).

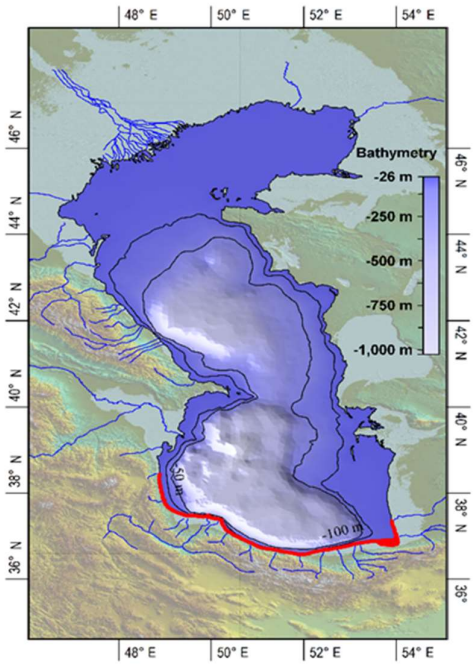

Figure 1: The location of the study area

3. Materials and Methods

3.1. Materials

A total of 539 sediment samples were analyzed from the shoreline and nearshore seabed up to a depth of 10 meters, along with 39 sediment samples from the most effective riverbeds leading to the sea. The sample collection took place from November to December 2013 and May to June 2014 by the Iranian Water Research Institute.

The sampling was conducted at 94 cross-shore profiles. Each profile was comprised of six sediment samples: one from the beach and the others from depths of 0.5, 1.5, 3, 6, and 10 meters. Additionally, three bed samples were collected from each river cross-section, including samples from the talweg, left bank, and right bank. The distribution of sampling sections can be seen in Figure 2. The sections for riverbed sampling were carefully selected to be sufficiently far from the river mouth and free from marine sediment influence, ensuring an accurate representation of the sediments entering the sea.

3.2. Methods

3.2.1. Grading

The sediment samples were analyzed at the laboratory of the Water Research Institute using sieve analysis. The hydrometer method was used for particles smaller than 0.063 millimeters.

The characteristics of grain size distribution curves of the samples have been compared using parameters such as mean (δ), sorting (M_Z), skewness (SK_G), and kurtosis (K_G). Formulas 1 to 5 were used to calculate the dimensionless grain size (ϕ) and the mentioned parameters. (Folk 1974[32]):

$$\varphi = -\log_2 d = -\ln d / \ln 2 \quad (1)$$

$$\delta = \frac{\phi_{84} - \phi_{16}}{4} + \frac{\varphi_{95} - \varphi_5}{6.6} \quad (2)$$

$$M_Z = \frac{\varphi_{16} + \varphi_{50} + \varphi_{84}}{3} \quad (3)$$

$$SK_G = \frac{\varphi_{16} + \varphi_{84} - 2\varphi_{50}}{2\,(\varphi_{84} - \varphi_{16})} + \frac{\varphi_5 + \varphi_{95} - 2\varphi_{50}}{2\,(\varphi_{95} - \varphi_5)} \quad (4)$$

$$K_G = \frac{\varphi_{95} - \varphi_5}{2.44\,(\varphi_{75} - \varphi_{25})} \quad (5)$$

The shape indices of the size distribution curve are useful in determining the origin of sediment. For example, the skewness parameter, which measures the departure from symmetry in grain size distribution, indicates whether there is an excess source of finer or coarser particles. Coastal and riverine sediments are typically categorized according to Tables 1 and 2[33].

The grain size distribution curve of coastal sediments generally falls within the moderate to good sorting range, while dunes are characterized by good sorting. River sediments, on the other hand, usually exhibit moderate to very poor sorting[32].

Coastal sediments usually have a negative skewness value in their grain size distribution, while aeolian (wind-blown) sediments tend to have positive skewness values. River sediments, exhibit skewness toward coarser particles[34].

There is a direct relationship between kurtosis and sorting, with higher kurtosis corresponding to better sorting[35]. Beach sands typically exhibit moderate to well-sorted kurtosis, while aeolian dunes fall within the well-sorted to very well-sorted range. River sediments tend to have broader kurtosis[36].

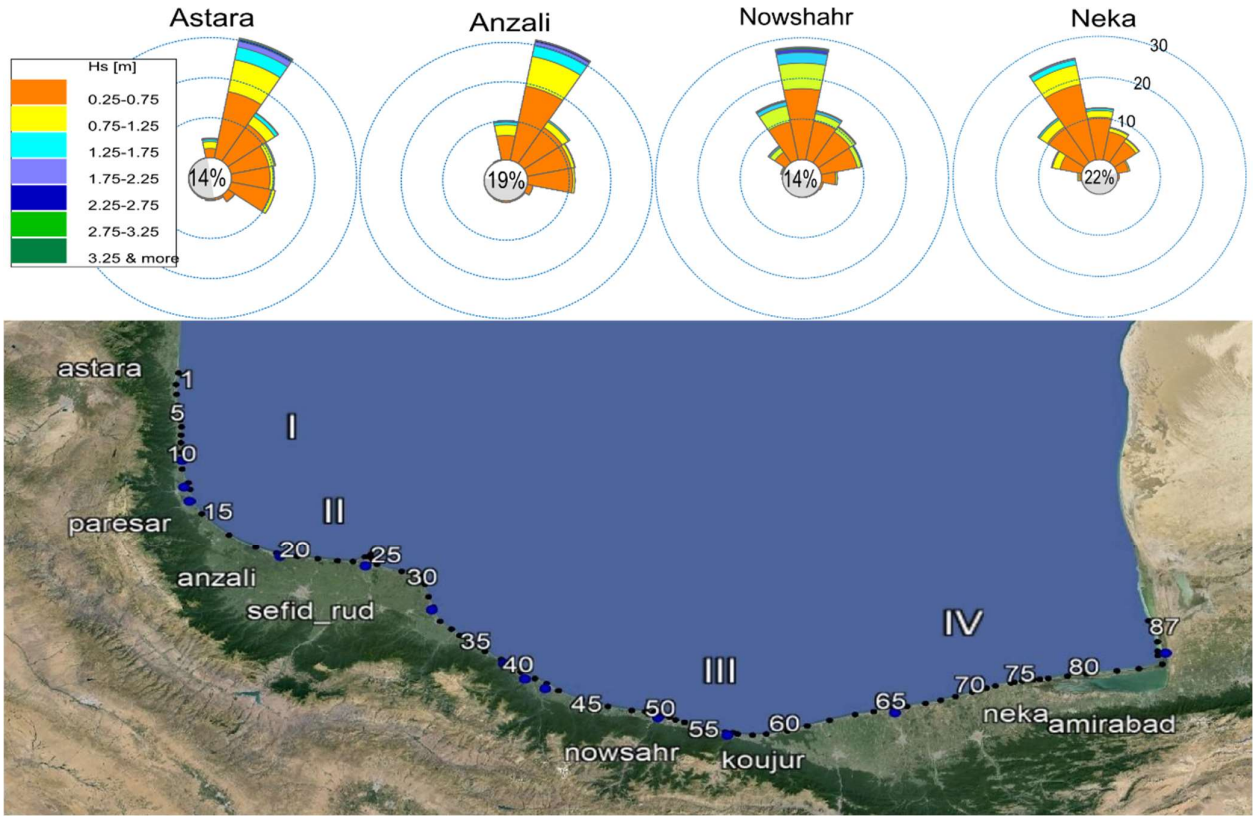

Figure 2: Location of surface bed samples and wave roses affecting the area

Table 1: Sorting and kurtosis classification[32]

Sorting		kurtosis	
Very well	>0.35	Very platykurtic	<0.67
Well	0.5-0.35	Platykurtic	0.9-0.67
Moderately well	0.7-0.5	Mesokurtic	1.11-0.9
Moderately	1-0.7	Leptokurtic	1.5-1.11
Poorly	2-1	Very leptokurtic	3-1.5
Very poorly	4-2	Extremely leptokurtic	> 3

Table 2: Classification of skewness[32]

Strongly fine_skewed	+1 - +0.3
Fine_skewed	+0.3 - _+0.1
Near_symmetrical	+0.1 - -0.1
Coarse_skewed	-0.1 - -0.3
Strongly coarse_skewed	-0.3 - _-1

3.2.2. Mineralogy

A Nikon (Eclipse E100) microscope with a 100X zoom scale was utilized to classify minerals in bed samples in the University of Qom's laboratory. Each sediment sample was photographed under the microscope, and the number of grains for each mineral in each sample was determined through visual counting. The percentage abundance of each mineral was calculated by dividing the number of grains for that mineral by the total number of grains. Figure 3 shows an example image of the collected sediment[37].



Figure 3: Microscopic image of a sample (100X)
(Location: profile # 2-deph 1.5m)

4. Results and Discussion

The amount of minerals in sediment samples varies along the shoreline and by the water depth. The reason is difference in distance and direction from the sediment sourthes (ie river mouths) and the density/strength difference of different minerals. The amount of heavy minerals changes significantly along the studied coastline. The heavy minerals are pyroxenes, augite, diopside, magnetite, goethite, tourmaline, pyrite, hematite, garnet, ilmenite, rutile, and zircon.
The grain size distribution of the sediment samples varies along the studied coastline. There is a general trend along the coastline and also some local variations near large rivers and harbors. The grain size distribution variations along the coastline are used to verify the dominant LST direction and to determine the impact zone of coastal structures and river mouths.

4.1. The general trend

Figure 4 illustrates the relative abundance of heavy minerals in collected sediment samples. It shows that heavy minerals are more prevalent along the western and central shorelines, compared to the eastern coasts. Here the mountains are near the sea. The rivers originate from mountainous regions and the bed slope along their entire path is steep, with no mild slope area to deposit the heavy minerals or larger grain sizes. These rivers transport a greater amount of heavy minerals to the shore. In contrast, eastern rivers contribute fewer heavy minerals to the coast. For instance, the Gorganrud River, located in the easternmost section, carries quartz-rich sediments without significant heavy minerals into the sea. The trend of decreasing heavy minerals aligns with the dominant littoral drift direction from west to east. Heavy minerals are less associated with littoral sediment transport compared to other grain sizes. Additionally, Figure 4 shows that the variation in heavy mineral abundance with depth, decreases along each section as we move eastward. Decrease in the intensity of waves and the presence of heavy minerals play a role in this regard.
Figures 5 and 6 illustrate the mean and sorting parameters of the grain size distribution for the sediment samples (see formulas 2 & 3). The two graphs shaw that the sediments are predominantly fine sand, and their sorting parameter falls within the moderate to good range. Considering Figure 2 for sample locations, the graphs reveal that in mountainous coasts, sediments at the shoreline and half-meter depth are much coarser than other depths. For these coasts, the sorting parameter is also much lower at the shoreline and half-meter depth compared to the other depths.

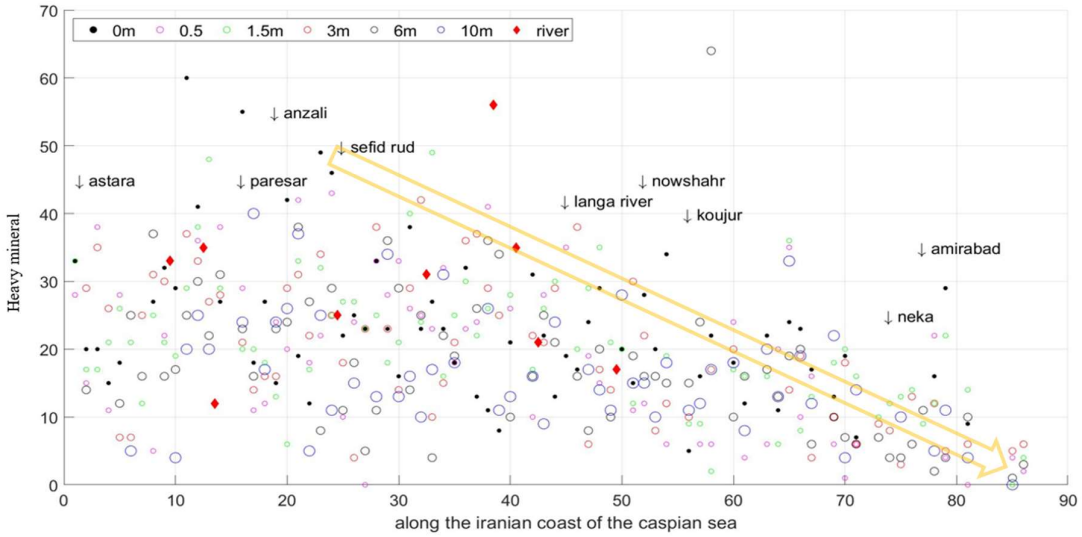

Figure 4: The abundance of heavy minerals in sediment samples.
(The horizontal axis indicates the section numbers in Fig. 2)

On the easternmost coast, where fine-grained sediment-rich rivers flow into the sea, sediment grain size is much smaller at all depths (both inside and outside the surf zone) compared to other coasts.

The studied coast along the Caspian Sea can be divided into three categories and five sections:

A) From sections 1 to 16 (Astara to Paresar) and from sections 35 to 61 (Kelachay to Khoshtsar), where the shoreline is near the mountains with mountainous rivers and coarse beach sands, exhibiting moderate to very poor sorting.

B) From sections 16 to 35 (Paresar to Kelachay) and from sections 61 to 83 (Khoshtsar to Miyankaleh), where the coastlines are far from the mountains, with sediments on the shoreline relatively similar to the entire surf zone.

C) From sections 83 to 87 (Gomishan coast), with very fine silty sediments on the coastline and the entire surf zone and beyond. The bed slope is extremely gentle due to the long-term influence of the Gorganrud and Atrak rivers, which pass through dry regions with a very low slope, carrying very fine sediments into the sea. The sorting of sediments in this region is also severely poor and distinct from other studied areas.

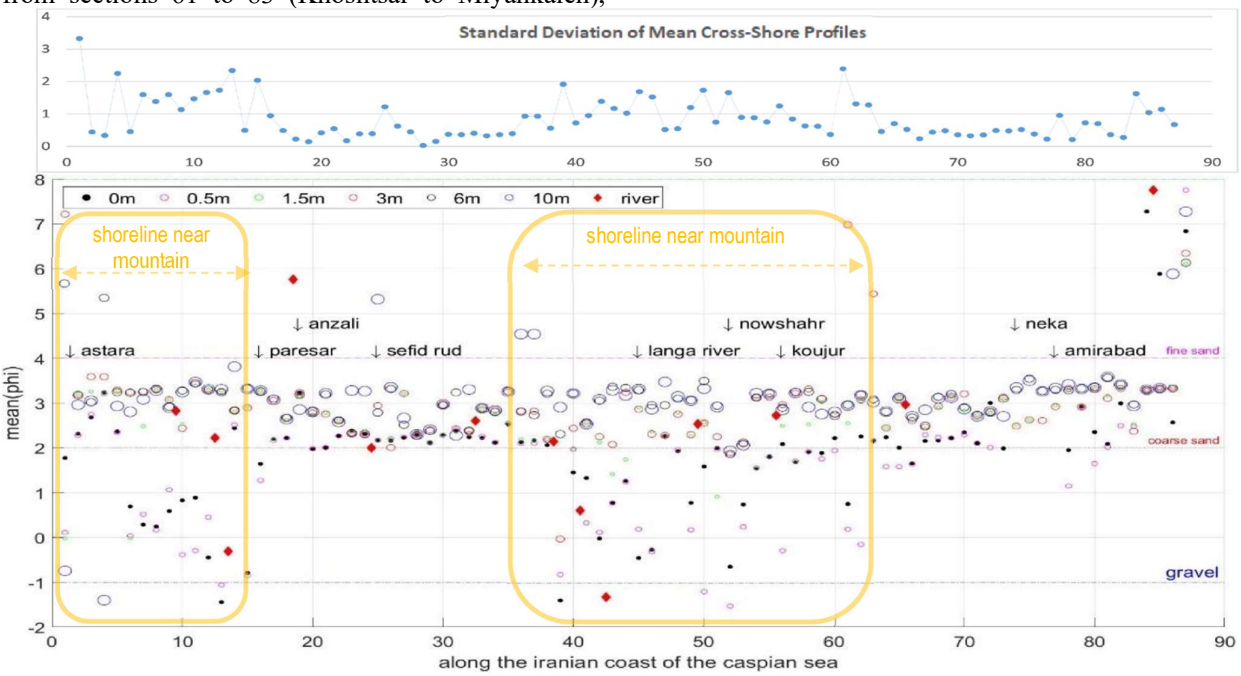

Figure 5: The mean grain size along the studied shoreline at different water-depths and the standard deviation of the mean parameter along each profime (The horizontal axis indicates the section numbers in Fig. 2).

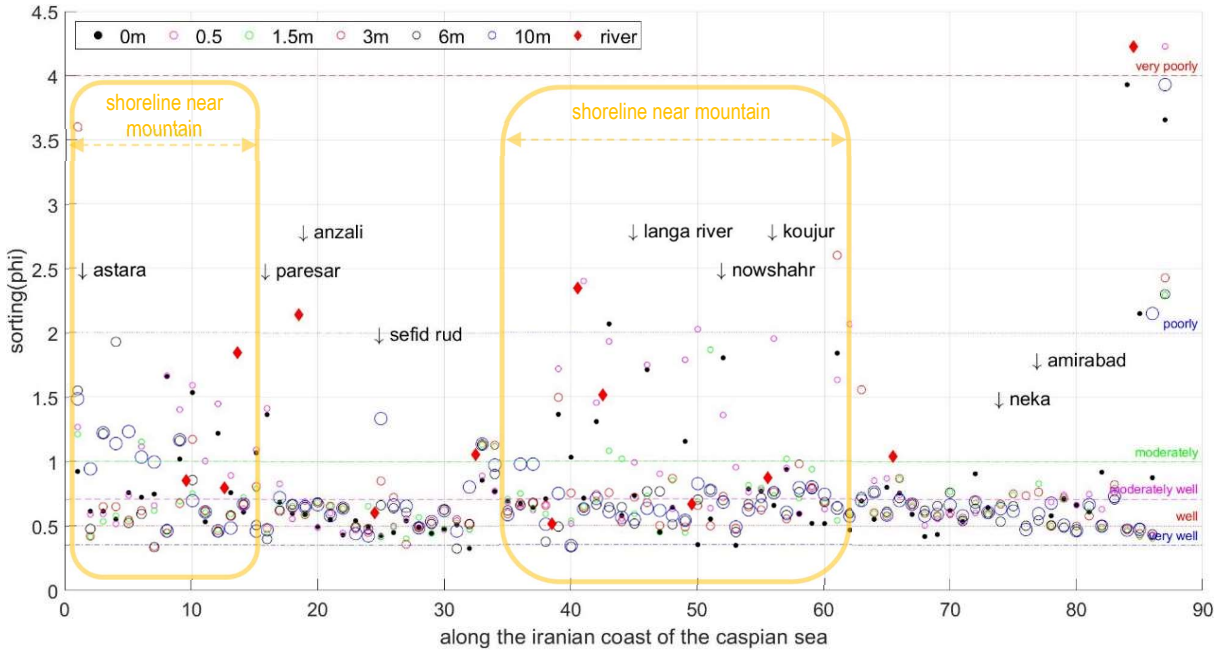

Figure 5: The sorting of grain size distribution along the studied shoreline at all inquiried water-depths (The horizontal axis indicates the section numbers in Fig. 2)

4.2. The direction of littoral drift

Considering the prevailing wave directions and shoreline angles shown in Figure 2, sediment transport along the southern coasts typically occurs from west to east or north to south. However, there is one exception: along the shoreline sections 18 to 25 depicted in Figure 2, the direction of LST is from east to west (see Fig. 7). This section of the shoreline constitutes a distinct sediment cell. The eastern boundary of this cell is marked by the mouth of the largest river in the study area, while the western boundary corresponds to the edge of a large bay that existed four centuries ago (as indicated by historical maps and travelogues) and is currently located near the entrance of a significant estuary.

An analysis of grain size variations along the studied coastline supports the aforementioned transport directions. For example, Figure 8 illustrates that the sand becomes progressively finer as one moves from section 25 (the river mouth) toward section 18, with no significant changes in coastal morphology. In the absence of any intervening factors, it is expected that sediment grain size along the coastal transport path will gradually decrease. This occurs because finer sediments are lighter and are more easily moved by littoral currents.

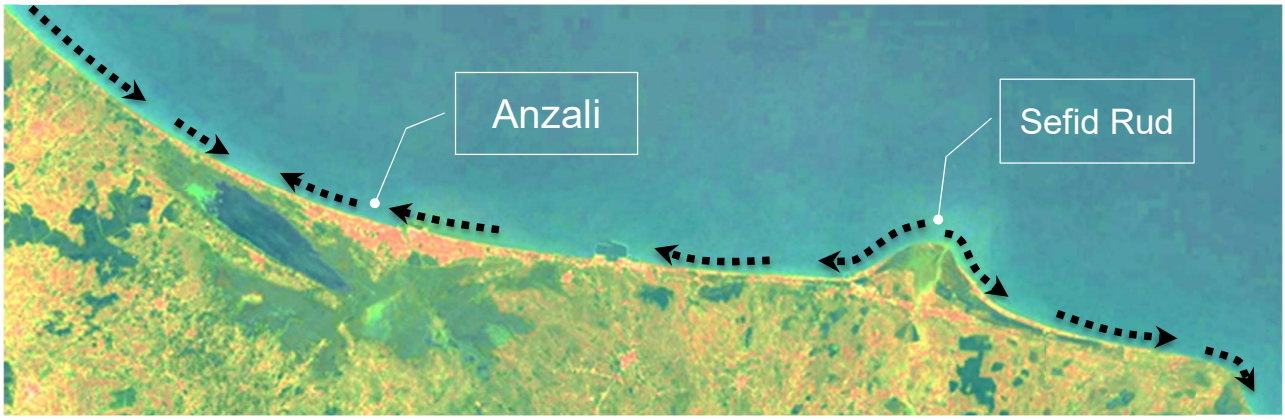

Figure 6: Satellite images of the area from Anzali to Sefidrud (Google Earth)

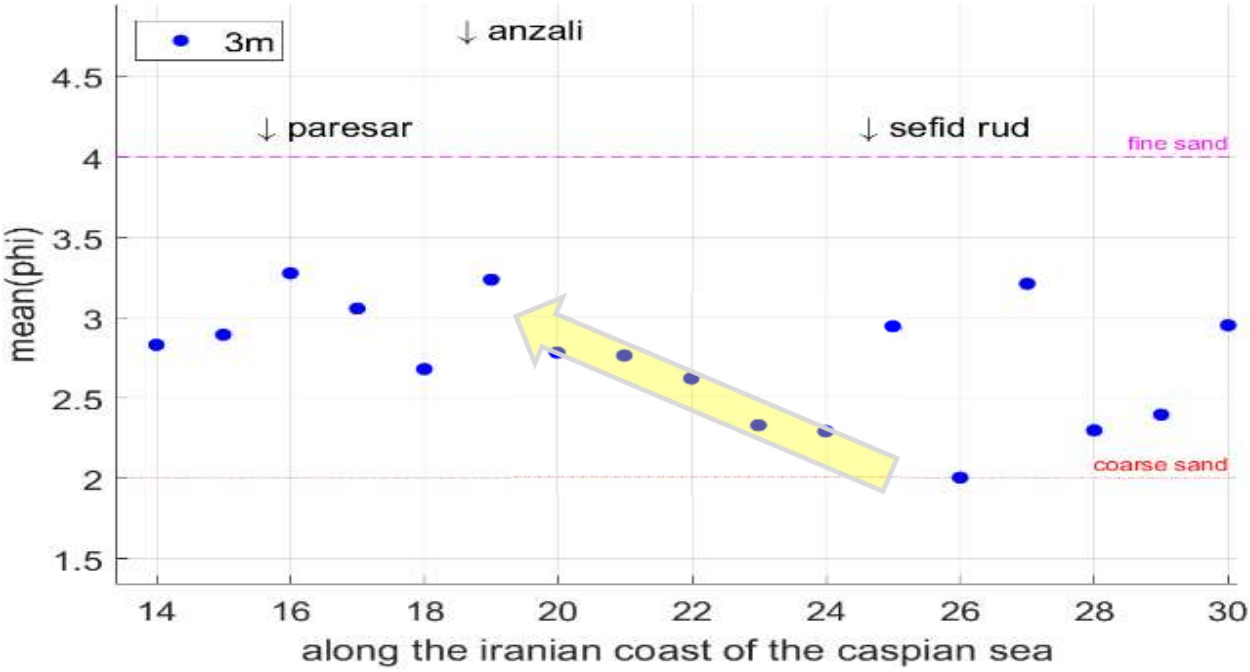

Figure 7: The mean grain around Anzali and Sefidrud shorelines at a depth of 3 meters

4.3. The impact zone of rivers and harbors

Studying the changes in grain size distribution along the coast is essential for understanding the length of coastline sections influenced by sediment-supplying rivers and large harbors that interrupt littoral drift.
Sediment-fed rivers disrupt the gradual variations in grain size distribution along the LST direction, as they introduce sediment with grain sizes that differ from those typically found along the shoreline. Similarly, large harbors alter coastal sediment dynamics by interrupting the natural transport of littoral sediments. Downstream of these harbors, waves are more effective at carrying finer and lighter grains, while there is no supply of replacement sand from upstream. This leads to a shift towards coarser sediments and heavier minerals.
This section analyzes sediment samples collected at depths of 1.5 and 3 meters, as the primary LST occurs within the nearshore area at depths ranging from 1.5 to 4 meters. Figures 9 and 10 illustrate the mean and sorting parameters, respectively.
The analysis focuses on two coastal structures and two river mouths. The selected harbor is Nowshahr Harbor, located at section 51, while the Neka-Sadra-Amirabad complex, which includes two water intakes and two harbors, is assessed at sections 73 to 76. The river mouths examined are the Sefidrud River at section 25 and the Atrak-Gorganrud River at sections 84 and 87.

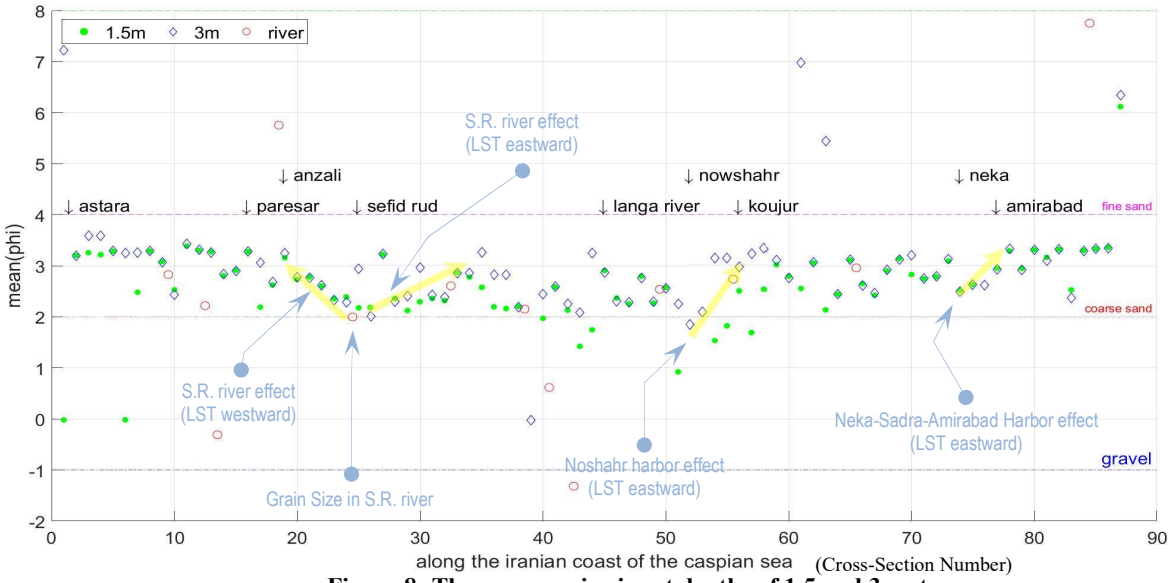

Figure 8: The mean grain size at depths of 1.5 and 3 meters
(The horizontal axis indicates the section numbers in Fig. 2)

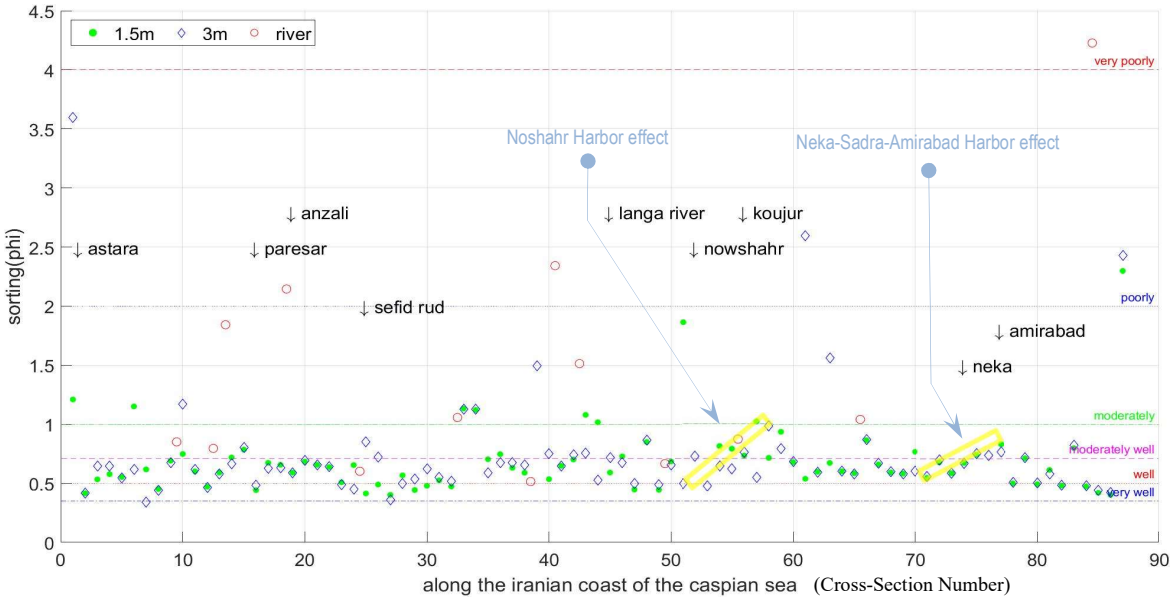

Figure 9: The sorting of grain size distribution at depths of 1.5 and 3 meter
(The horizontal axis indicates the section numbers in Fig. 2)

4.3.1. Nowshahr Harbor

Nowshahr Harbor (section 51) was constructed between 1929 and 1939, with its entrance located 900 meters from the initial shoreline. The dominant LST direction in this area is eastward. Over the past 85 years, the harbor has prevented the surf-zone sand from reaching the eastern beach. There are no significant sediment-supplying rivers to the east of the harbor (see Fig. 11).



Figure 10. Satellite images of the shorline from Nowshahr Harbor to Sysangan (Google Earth)

Figure 9 illustrates that the sediment size on the eastern shore is much coarser than that on the western coast, a difference attributed to erosion occurring on the lee side of the harbor. As one moves further east to section 56, the coarseness of sediment gradually decreases, aligning more with the general trend in the area. This indicates that Nowshahr Harbor has affected approximately 28 kilometers of the downstream beach as of the sampling year of 2011.

Figure 12 reveals the surf-zone bathymetry downstream of the harbor (sounding date: 2005). It shows that the 2-meter depth contour line is very close to the shoreline, only 15 to 30 meters away, for up to 23 kilometers downstream of the harbor. Beyond this point, the distance increases to between 120 and 200 meters. The length of the eroded beach, determined by grain size comparison (28 km), aligns reasonably well with the result obtained from surf zone hydrography (23 km). The discrepancy is only 15%, while sediment sampling and grain size comparison method is more cost-effective than beach profiling.

The coastal land east of Nowshahr Harbor consists of hard soil that does not erode easily due to wave action. Consequently, satellite imagery does not provide useful information for identifying the eroded zone.

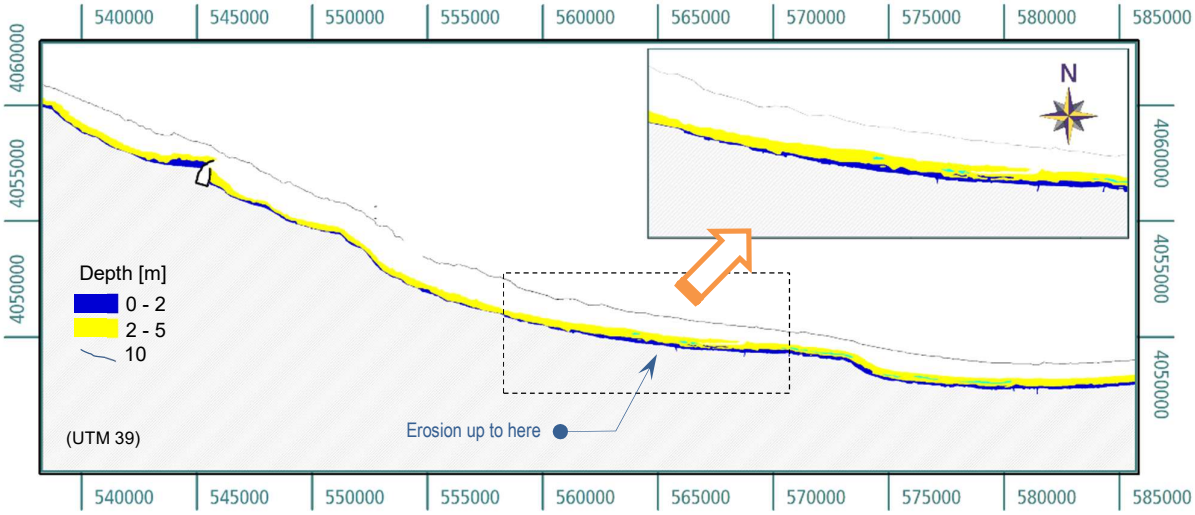

Figure 11: The 2 and 5-meter depth contours along the coast from Nowshahr to Sisangan, based on the measurements conducted by the National Cartographic Center in 2005

4.3.2. Neka-Sadra- Amirabad complex

The Neka power plant has two water intakes and is located near the Sadra harbor at section 73, with another harbor situated 8 km to the east at section 76. These facilities were built between 1977 and 2005 and extended between 800 to 2000 meters from the original shoreline (refer to Fig. 13). In this region, the LST direction is eastward. The presence of these structures disrupts the natural LST, leading to erosion along the eastern shorelines.



Figure 12: Satellite images of the area from Neka to Amirabad (Google Earth)

Figure 9 illustrates how the Neka-Sadra complex has resulted in a sudden increase in sediment grain size due to erosion at section 73. As one moves eastward away from Sadra toward section 78, which is located downstream of the Amirabad harbor (section 76), the grain size gradually decreases. This indicates that the area impacted by erosion from Amirabad harbor merges with the impact zone of the Neka-Sadra complex. The erosion in this region has also caused a slight decline in the sediment sorting index from Sadra to Amirabad harbors (see Fig. 10).

The irregularities in grain size and sorting observed conclude after section 78. This signifies that the total area affected by erosion from the Neka-Sadra-Amirabad facilities spans approximately 14 km (from section 73 to section 78), which corresponds with findings from satellite imagery.

Interestingly, the grain size on the lee side of Amirabad harbor is not coarser than that on the upstream (west) side. This is because a significant portion of the materials dredged during construction was deposited on the eastern coast, which is then eroded by larger storms along the shoreline. As a result, there is a sediment source to replace the finer particles of the eroded materials from the surf zone.

4.3.3. Sefidrud River

The Sefidrud River, located at section 25, is the largest river flowing into the Iranian shores of the Caspian Sea. As shown in Figure 9 (see section 25), the sediment carried by the river is coarser than that of the surrounding shoreline. This coarser sediment greatly influences the grain size in the surf zone of the sea.
Moving away from the river mouth, the sediment grain size decreases on both sides (from section 25 to section 18 and from section 25 to section 35). This decrease is due to the direction of sediment transport being away from the river mouth. Interestingly, the sediment transport path from the Sefidrud mouth to Anzali (section 25 to section 18) is the opposite of what is generally observed along most southern Caspian shores, which typically transport sediment from west to east (see Fig. 7).
Based on the trend lines in Figure 9, the river's sediment supply significantly affects the sediment grain size distribution along the western and eastern shorelines, extending up to 43 km and 68 km, respectively. An anomaly observed at section 30 is attributed to a local river mouth, known as RoodSar.
At section 18, there is an estuary inlet that serves as the entrance to Anzali harbor. The river associated with this inlet carries fine-grained sediments; however, the majority of these sediments settle either inside the estuary or within the harbor basin. Consequently, they have minimal impact on the sediment texture in the surf zone on both sides of the inlet. The wash load and remaining cohesive materials that are released into the sea cannot settle in the surf zone due to wave action.

4.3.4. Gorganrud and Atrak Rivers

The Gorganrud River (section 84) and the Atrak River (near section 87) flow into the southeastern corner of the Caspian Sea (see Fig. 9, section 84). The mouth of the Gorganrud River is located precisely at the corner, while the mouth of the Atrak River is situated 20 kilometers to the north. The LST direction on both sides is towards this corner. The Atrak River carries very fine-grained sediments to the sea. In this region of the Caspian Sea, the coastal and seabed slopes are quite gentle. The distance from the shoreline to a depth of 30 meters is approximately 50 kilometers, and the maximum slope of the seabed is less than 0.1%. As a result, large waves do not reach the nearshore area in this part of the Caspian Sea

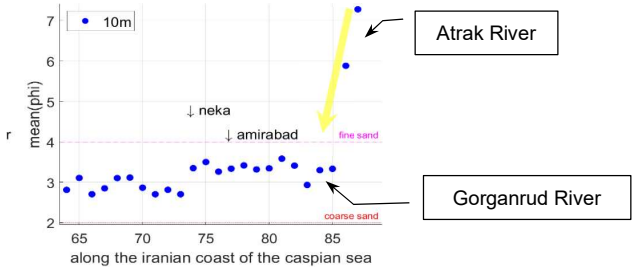

Figure 13: The mean grain size off the south-eastern shoreline (at a depth of 10 meters)

5. Conclusions

Sediment texture along the southern (Iranian) shores of the Caspian Sea has been analyzed using approximately 600 sediment samples collected from nearly 90 beach profiles, with six samples taken from both inside and outside the surf zone along each profile. The differences in sediment samples were examined in both the longshore and cross-shore directions from sedimentological and mineralogical perspectives. The study highlights the impact of sediment supplies from rivers and the erosional effects of harbors, which have contributed to changes in sediment texture along the southern Caspian coast.
This research specifically focuses on variations in three selected indices: mean grain size, sorting, and abundance of heavy minerals. These indices were used to assess sediment transport directions and the influence zones of major rivers and harbors.
The findings confirm a general trend of eastward LST direction, except for the Anzali-Sefidrud shoreline, which is identified as a distinct sediment cell with LST directed westward. A shift in the LST direction occurs at the mouth of the Sefidrud River.
Additionally, the study demonstrates that the erosional impact zones for Noshahr harbor and the Neka-Sadra-Amirabad complex extend approximately 27 and 15 kilometers eastward, respectively. The influence zone of the Sefidrud River mouth within the surf zone spans about 68 kilometers to the east and 43 kilometers to the west.
Attempts were made to estimate the closure depth based on the variations in sediment sample characteristics inside and outside the surf zone. However, a specific criterion for distinguishing

sediments in these two areas was not established. This may be due to the limited number of sediment samples collected along each profile or the historical changes in sea level, which included a decrease of approximately 3 meters, followed by an increase of 2.5 meters, and a further decrease of 2 meters within a century.

Acknowledgements

We extend our utmost gratitude and appreciation to the Water Research Institute of the Ministry of Energy for providing sediment samples and grain size analysis data. Without their support, conducting this research would not be possible.

6. References

1. Folk RL, Ward WC. Brazors river bar: A study in the significant of grain size parameters. *Journal of sedimentary petrology*. 1997;27:3-26.

2. Mclaren P, Bowles D. The effects of sediment transport on grain_size distributions. *Journal of sedimentary petrology*. 1985;55:0457-0470.

3. Wan Mohtar WHM, Nawang SAB, Abdul Maulud KN, Benson YA, Wan Mohamed Azhary WAH. Textural characteristics and sedimentary environment of sediment at eroded and deposited regions in the severely eroded coastline of Batu Pahat, Malaysia. *Science of the Total Environment*. 2017;598:525-537. doi:10.1016/j.scitotenv.2017.04.093

4. Yang L, Ma X, He Y, et al. Spatiotemporal variations in the grain size distribution in the water column and sediments from the Yellow River Delta to distal areas under coastal currents. *Journal of Marine Systems*. Published online 2024:103997-103997. doi:10.1016/j.jmarsys.2024.103997

5. Friedman GM. Dynamic processes and statistical parameters compared for size frequnecy distribution of beach and river sands. *Journal of sedimentary petrology*. 1967;37:327-354.

6. Bing-fu J. Influencing factors and significance of the skewness coefficient in grain size analysis. *Marine Sciences*. Published online 2012.

7. Gao Shu, Collins Michael. Net sediment transport patterns inferred from grain-size trends, based upon definition of "transport vectors. *sedimentary geology*. 1992;80:47-60.

8. Shandao Z. Grain size distribution and transportation trends of bottom sediments in the sand ridge field of the south yellow sea,china. *Marine Geology & Quaternary Geology*. Published online 2012.

9. Yun-Pin Y. Trend and Dynamic Cause of Sediment Transport on the Adjacent Continental Shelf of the Yangtze River Estuary. *Marine Science Bulletin*. Published online 2015.

10. Li T, Li T, Li TJ. Sediment transport processes in the Pearl River Estuary as revealed by grain-size end-member modeling and sediment trend analysis. *Geo-marine Letters*. 2018;38(2):167-178. doi:10.1007/S00367-017-0518-2

11. Wang H, Wu Y, Qin W, Wang S. Grain Size Characteristics of Surface Sediments and Their Migration Trends in the Nearshore Waters of East Guangdong. *Sustainability*. Published online 2023. doi:10.3390/su151411069

12. Wang Xiankun, Ke Xiankun. Grain-size characteristics of the extant tidal flat sediments along the Jiangsu coast, China. *sedimentary geology*. 1997;112:105-122.

13. Cheng J, Gao S, Wang Y, Min F. Grain size characteristics of surficial sediments and their response to hydrodynamics over the coastal waters of northern jiangsu province. *Marine Geology & Quaternary Geology*. 2009;29(1):7-12. doi:10.3724/SP.J.1140.2009.01007

14. Yamashita S, Naruse H, Nakajo T. Reconstruction of sediment-transport pathways on a modern microtidal coast by a new grain-size trend analysis method. *Progress in Earth and Planetary Science*. 2018;5(1):1-18. doi:10.1186/S40645-018-0166-9

15. Muhardi M, Nurrahman AY, Risko R, Muliadi M, Rahayu N, Susiati H. Statistical parameters analysis of sediment grain size from raya river bengkayang regency, west borneo. *Bulletin of the marine geology*. 2022;36(2). doi:10.32693/bomg.36.2.2021.726

16. Jiang S, Xu F, Liu X, Zhao Y, Xu W. Distributional characteristics of grain sizes of surface sediments in the Zhujiang River Estuary. *Acta Oceanologica Sinica*. 2014;33(4):30-36. doi:10.1007/S13131-014-0462-1

17. Duc Dao Manh, Nhuan Mai Trong, Nghi Chu Van, et al. Sediment distribution and transport at the nearshore zone of the Red River delta,

Northern Vietnam. *journal of asian earth sciences*. 2007;29:558-565.

18. Amalan K, Ratnayake NP, Weerawarnakula S. Prospecting sand resources at the continental shelf in offshore galle, Sri Lanka. *Journal of Geological Society of Sri Lanka*. 2014;16:65-73.

19. Perera U, Ratnayake AS, W. R. D, et al. Grain size distribution of modern beach sediments in Sri Lanka. *Anthropocene coasts*. 2023;6(1). doi:10.1007/s44218-023-00025-7

20. Wichkramasooriya A, U.A.D.P, Gunawardane. Analysis of Sediment Characteristics and Depositional Environment of Beach Sediment along the Pulmoddai Mineral Sand Deposit in Eastern Coast of Sri Lanka. *Journal of Geological Society of India*. 2024;100(4):554-560. doi:10.17491/jgsi/2024/173872

21. Timothy Oyedotun Temitope D. Sediment characterisation in an estuary – Beach system. *journal of coastal zone management*. 2016;19:433. doi:10.4172/2473-3350.1000433

22. Pham Dat T, Gouramanis Chris, Switzer Adam D, et al. Elemental and mineralogical analysis of marine and coastal sediments from Phra Thong Island, Thailand: Insights into the provenance of coastal hazard deposits. *Marine Geology*. 2018;385:274-292. doi:10.1016/j.margeo.2018.01.006

23. Golamdokht Bandari Mehdi, Rezaee Payman, Ghorbani mansour. Sedimentary and geochemical characteristics of coastal deposits in Hormoz Island in the south of Iran. *Journal of Stratigraphy and Sedimentology Researches University of Isfahan*. 2019;36:105-124. doi:10.22108/jssr.2020.118294.1111

24. Karimkhani Bahador Afshin, Feiznia Sadat, Aleali Mohsen, Arian Mehran. Sedimentary facies deposited on the continental shelf in the south part of Caspian sea-Iran. *Scientific Quarterly Journal*. 2023;33:27-54. doi:10.22071/gsj.2022.343081.2000. in persian

25. Khajeh Mansour, Ghoumian Jafar, Faiznia Sadat. Investigating the lateral changes of particle size and mineralogy in order to determine the prevailing wind direction in the formation of loess sediments in Golestan province. *desert journal*. 2004;9. in persian

26. Lashteh Neshaei Mir Ahmad, Asalami Abolfazl, Pirou Mohammad. Investigating the potential of sediment transfer in the shores of the Caspian Sea. *International Journal of engineering*. 2005;17:39-45. in persian

27. Khoshravan H, Rohanizadeh S, Malek J, Nejadgholi G. Caspian Sea southern coasts zoning on the basis of sedimentary morphodynamic indicators. *Journal of earth and space physics*. 2010;37:1-15. in persian

28. Bagheri H. Sedimentology and mineralogical characteristics of the coastal sediments in the southern part of the Caspian Sea (Iran). *Research Journal of Marine Sciences and Techniques*. 2016;11. in persian

29. Mirkazemian Maryam, Adabi Mohammad Hosein, Lotfi Mohammad, Saeedi Abdollah. Study of Distribution and Provenance of Zircon in Beach Sands of Babolsar- Noor. *earth quarterly*. 2010;1. in persian

30. Amini Arash, Moussavi-Harami Reza, Lahijani Hamid, Mahboubi Asaddollah. Sedimentological, geochemical and geomorphological factors in formation of coastal dunes and nebkha fields in Miankaleh coastal barrier system (Southeast of Caspian Sea, North Iran). *Geosciences Journal*. 2012;16:139-152. doi:10.1007/s12303-012-0014-7

31. Kayani Somia, Afride Faezeh. Comparison of particle diameters of beach sediments in Khazarabad and Royan beaches. *National Conference of the Iranian Association of Geomorphology*. in persian

32. Folk RL. *Petrology of Sedimentary Rocks*. Hemphill Pablishing Company Austin Texas; 2002.

33. Blott Simon J, Pye Kenneth. Gradistat: A grain size distribution and statistics package for the analysis of unconsolidated sediments. *Earth Surface Processes and Landforms*. 2001;26:1237-1248. doi:10.1002/esp.261

34. Das BM. *Geotechnical Engineering Handbook*. J. Ross; 2011.

35. Mohammadnia Maliha, Amir Ahmadi Abulgasem, Zanganeh Asadi Mohammad Ali. Investigation of granulometric parameters in wind erosion studies (case study: Gonabad city). *Applied Research Journal of Geographical Sciences*.

2022;66:159-169. doi:10.52547/jgs.22.66.159. in persian

36. Khanehbad Mohammad, Hajian Nilufar, Moussavi-Harami Reza, Mahboubi Asaddollah. Investigating the texture, sedimentary facies and sediment microerosion process in the Faroub Roman River (northeast of Neishabur). *Hydrogeomorphology Journal*. 2015;5:119-140. in persian

37. Esfandiari Mohammad Reza. *Sedimentology of the Southern Caspian Sea Coastline, from the Viewpoint of Coastal Engineering*. MSc Thesis. University of Qom; 2023.

INTERNATIONAL JOURNAL OF
COASTAL, OFFSHORE & ENVIRONMENTAL ENGINEERING IJCOE Vol.11/No. 2/Spring 2026 (72-78)

Available online at: www. Ijcoe.org

Seismic Assessment of Suspended-Zipper Braced Frame (SZBF) in Coastal Steel Structures Equipped with ADAS-SMA Hybrid Damper

[1] Ahmad Hasanpoor Ghadikolaei [1], Heydar Dashti Naserabadi [2*], Morteza Jamshidi[3]

[1)] *Department of Civil Engineering, Cha. C. Islamic Azad University, Chalus, Iran. 2162633140@iau.Phd student,*
[*2)] *Department of Civil Engineering, Cha. C. Islamic Azad University, Chalus, Iran. dashti.n@iau.ac.ir*
[3)] *Department of Civil Engineering, Cha. C. Islamic Azad University, Chalus, Iran. Morteza_jamshidi@iau.ac.ir*

ARTICLE INFO

Article History:
Received 30 Aug 2025
Accepted 26 Feb 2026

Keywords:
Suspended-zipper braced frames, SMA material, ADAS damper, Nonlinear static analysis, OpenSees.

ABSTRACT

In this paper, a suspended-zipper braced frame (SZBF) equipped with hybrid damper consisting of Added Damping and Stiffness (ADAS) metallic damper and shape memory alloy (SMA) wires is introduced. The proposed seismic-force-resisting system is designed by performance-based plastic design (PBPD) method, which in addition to a significant reduction in the residual displacement of the structure, can increase the collapse displacement amount by providing a suitable lateral strength and ductility compared to the conventional SZBF. A new method for designing the proposed hybrid damper is presented, in which a factor of highest hysteretic energy is provided. The existing models in this paper are two high-rise 12 and 16-story SZBFs in two cases (a) with the conventional system and designed by force-based design method (b) with proposed hybrid damper and designed by the PBPD method. Seismic assessment of the proposed SZBF (PSZBF) by nonlinear static analysis is performed under two lateral load patterns of parabolic and uniform, in accordance with the FEMA-P695 in OpenSees software. Using the PBPD design method instead of the FBD method reduces the steel consumption by approximately 5.5-7.3% in the SZBF, which is expected to decrease further with the increasing number of stories. Since the PBPD method results in a weaker design of columns and braces than the FBD method by about 5-10%, the elastic stiffness of the PSZBF models is about 5% lower than the FBD models, that the elastic stiffness in both models can be assumed to be equal. Although PSZBF models have lower maximum lateral resistance than FBD models, they are able to absorb energy about 25% more in addition to increasing collapse lateral displacement.

1. Introduction

The bracing members, due to their high strength and stiffness, are in many structures responsible for controlling and resisting the applied lateral loads on the structure. One of the conventional types of steel bracing is the chevron bracing, which, due to its special configuration, has suitable compatibility to create architectural openings. When lateral loads are applied, at first, both bracing elements, by providing equal tensile and compressive strengths, resulting in the balancing of the lateral loads' effect.

The post-buckling strength of a compression brace according to EC8 [1], is equal to 30% of its yield strength, or its tensile strength. Also, according to the AISC [2], the post-buckling strength of a compression brace is equal to 30% of the initial buckling load of the brace. In the meantime, due to the loss of the brace compressive strength after buckling event, a large unbalanced force is created at the connection point of the braces to the beam. In this case, the seismic forces applied to the structure are concentrated in a particular story (the same story with the buckled brace). As a result, this system does not exhibit much force

redistribution capability and has not performed well in past earthquakes [3-5].

In order to achieve a stable inelastic seismic response, Khatib et al. [6] proposed adding a zipper column at the connection point of braces to the beam, in which case, along the structure height, the compressive braces buckle and the tensile braces yield. Leon and Yang [7] suggested that, if the upper story braces remain elastic, it prevents the global mechanism formation in the structure, and this modified configuration is known as an SZBF. Consequently, in the continuation of inelastic part of the capacity curve, by providing high stiffness and lateral strength, bring the structure to the target structural performance level during severe earthquakes. Despite the extensive numerical and experimental researches about the structural performance evaluation of the SZBFs in recent years [8-11], which were carried out by many researchers in order to improve the dynamic response of this type of system, we can point out some weaknesses in this system, which, in particular circumstances, removes it from an ideal seismic-force-resisting system. These weaknesses are referred to as below.

The zipper elements should be designed to transfer all unbalanced forces to the roof story, so, the size of the elastic hat members (two braces zipper column) becomes very large. If the SZBF is used in high-rise steel frames, the seismic demand for elastic hat members will be very large, therefore there is a need for large sections for them that could lead to problems such as implementation incompatibility with column and beam members with smaller sections in the roof story.

Although the SZBF with high energy absorption capacity results in minimum damage to the structural and non-structural system under moderate to severe earthquakes, it is often accompanied by large residual displacement after the earthquake that makes it unsuitable for confronting future earthquakes. Recent researches suggest that for a residual displacement ratio of more than 0.5%, building a new structure is more desirable than rebuilding or repairing a damaged structure [12]. Hence, the development of new devices without the mentioned limits requires the use of new materials. In this paper, the SZBF equipped with hybrid damper consisting of ADAS metallic yielding damper and SMA wires is introduced to deal with severe earthquakes. This proposed structural system in addition to having all the advantages of a conventional SZBF has two distinct characteristics of high recentering and high energy dissipating due to the of the super-elastic SMA material and the yielding of the ADAS damper steel strips, which is designed by considering the yielding mechanism and target drift.

2. Methods

The models' elevation is shown in Figure 1. The seismic-force-resisting system of these frames is a concentrically braced steel frame of a suspended zipper-type with special ductility. The models used in this paper are introduced in two cases. The first case models with the names of 12st-FBD and 16st-FBD are designed by the FBD method. The second case models with the names of 12st-PSZBF and 16st-PSZBF, which are designed according to the PBPD method, are equipped with the proposed hybrid damper in all zipper columns and the roof story braces. The design seismic level is life safety (LS) in accordance with ASCE7-16 standard [13].

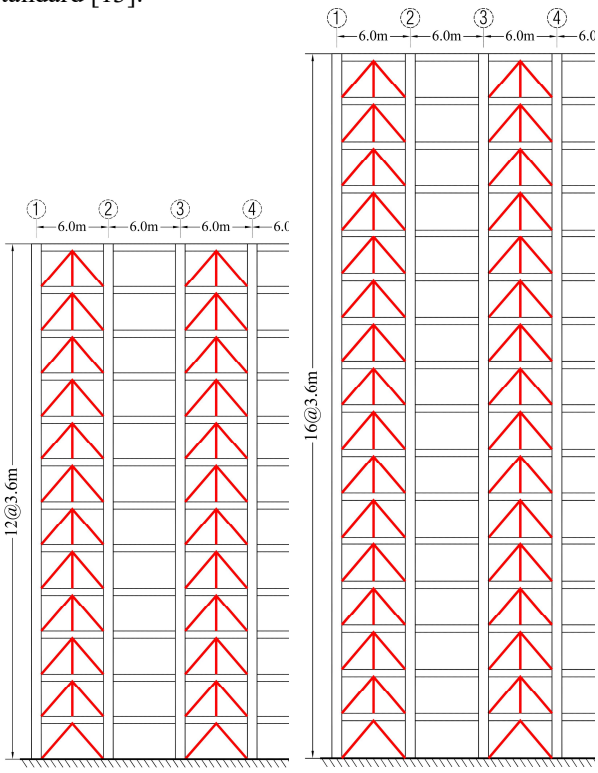

Figure 1. Elevations of models used in this paper

The steel elements of the models were designed in accordance with the AISC360-10 and IBC2006 codes [14, 15]. In the present study, the structural steel in the ADAS steel strips, SS400 grade according to the JIS G3101 standard, with yield stress, ultimate stress and modulus of elasticity are respectively equal to F_y = 308.5MPa, F_u = 446.5MPa, and E_s = 200GPa. Other steel elements of the SZBF are the A36 grade according to ASTM A36 / A36M standard, with F_y = 250MPa, F_u = 400MPa, and E_s = 200GPa. The frame mass in accordance with the ASCE41-06 standard [16] is equal to 3221 kN/Floor. The steel frames sections are shown in Figure 2. Table 1 shows the cross-section's specifications used for steel elements.

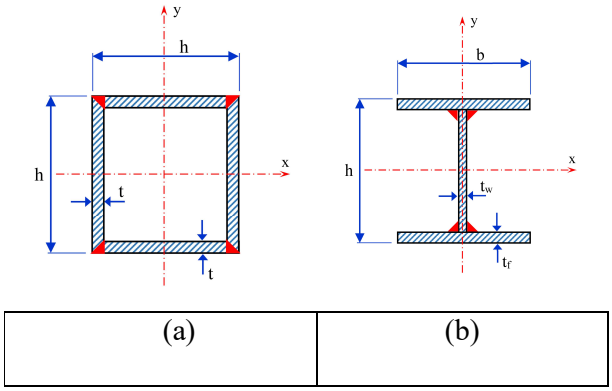

Figure 2. Cross-sections of Structural Components for, (a) Column, Zipper, and Braces, (b) Beams

Table 1. Specifications of the Cross-Sections

Column, Brace and Zipper Sections									Beam Sections				
Sections	h (mm)	t (mm)	Sections	h (mm)	t (mm)	Sections	h (mm)	t (mm)	Sections	h (mm)	b (mm)	t_w (mm)	t_f (mm)
C1	140	8	C12	375	22	C23	625	40	B1	325	175	8	10
C2	150	10	C13	400	24	C24	675	40	B2	350	200	8	10
C3	175	10	C14	425	25	C25	725	40	B3	350	200	8	12
C4	175	12	C15	450	26	C26	775	40	B4	350	200	8	15
C5	200	12	C16	475	28	C27	800	42	B5	375	200	8	15
C6	225	13	C17	500	30	C28	800	45	B6	400	225	8	15
C7	250	15	C18	525	30	C29	800	48	B7	425	250	8	17.5
C8	275	17	C19	550	32	C30	825	50					
C9	300	18	C20	550	35	C31	900	52					
C10	325	20	C21	550	40	C32	900	60					
C11	350	20	C22	600	40								

NONLINEAR STATIC ANALYSIS (PUSHOVER ANALYSIS)

In this section, the seismic behavior of SZBFs under nonlinear static analysis in two modes: (1) the SZBF designed by conventional FBD method; (2) the SZBF with SMA-ADAS damper designed by PBPD method is discussed. In order to evaluate the seismic performance of the sample frames and determine the seismic design parameter (Ω_0) of the seismic-force-resisting system under study, FEMA-P695 methodology [17] has been used. According to FEMA-P695 methodology, the structure under analysis should be affected by the combination of a gravity load of 1.05D + 0.25L where D is dead load and L is live load. The basis of loading according to FEMA-P695 methodology is based on ASCE/SEI41-06 specifications [18].

In nonlinear static analysis, earthquake lateral loads are applied statically and incrementally to structure until the displacement at a specific point (center of roof diaphragm) is reached to a target displacement or resulted in a collapse of the structure. The lateral load distribution on the structural model should be as similar as possible to what would occur during an earthquake and create critical states of deformation and internal

forces in the members. The distribution is proportional to the lateral load distribution in the nonlinear static method according to the relationship of the design lateral load distribution along the building height. The fundamental period of the 12- and 16-story models is respectively 1.143 and 1.438 seconds. Two types of uniform and parabolic lateral load patterns are used to perform nonlinear static analysis. The parabolic lateral load pattern for nonlinear static analysis is according to Eq. 1.

$$F_i = \frac{w_i h_i^{\,k}}{\sum_{j=1}^{n} w_j h_j^{\,k}} \quad ;$$

$$K = \begin{cases} 1 & T < 0.5 \\ 0.5T + 0.75 & 0.5 \le T \le 2.5 \\ 2 & T > 2.5 \end{cases} \qquad (1)$$

Where F_i is the load contribution of the base shear in the i-th story, w_i is the seismic weight of the i-th story, and h_i is the height from the seismic base level to the i-th story level. The structure pushing continues as long as either the structure has reached to the general instability or during the pushing process, one or more of its members has reached to a certain limit state (e.g. Shear failure and instability in the columns). The second state of instability, which is essentially a force-based control, is termed as " Non-Simulated Collapse Modes" and needs to be controlled separately for the critical components of the structure according to their ultimate capacity. In the models of this paper, basically the structures pushing is continued to the general instability of the structure and no effect of " Non-Simulated Collapse Modes" is observed.

Normalized base shear curves based on the seismic weight versus roof displacement for the models derived from nonlinear static analysis are shown in Figure 3. The elastic stiffness of the PSZBF models is about 5% lower than that of the FBD models, due to the weaker structural elements design of the PSZBF models because of the lower base shear obtained by the PBPD method. As a result, the elastic stiffness parameter for the two types of zipper bracing FBD and PSZBF are equal with a slight difference. Another important structural parameter in pushover analysis is the energy absorption in the structure that is equal to the area under the pushover curve, and the greater this area, the structure is able to absorb more energy. According to the pushover curve, the energy absorption of the structure is directly proportional to the base shear, maximum roof displacement, and elastic stiffness.

3. Results and Discussions

According to the results of pushover analysis, the energy absorption of the models and the increasing percentage in PSZBF models compared to the FBD models are shown in Table 2. The increasing percentage of the PSZBF models compared to the FBD models for the 12- and 16-story frames is about 43-50% and 17-23%, respectively. Although PSZBF models have lower maximum lateral resistance, they are able to absorb input energy by increasing the collapse lateral displacement. Also, by increasing the number of stories from 12 to 16, the energy absorption of PSZBF models is reduced by about 50% (figure 4 and 5).

Table 2. The Energy Absorption of the Models

Parabolic			Uniform		
Models	Energy Absorption (MJ)	Increasing Percentage*	Models	Energy Absorption (MJ)	Increasing Percentage
12st-FDB	1110	14.5	12st-FDB	1255	24.4
12st-PSZBF	12.71		12st-PSZBF	1561	
16st-FDB	1821	24.1	16st-FDB	1679	25.4
16st-PSZBF	2260		16st-PSZBF	2105	

*Increasing of PSZBF models to FBD models

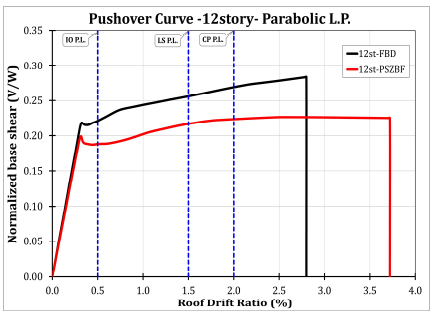

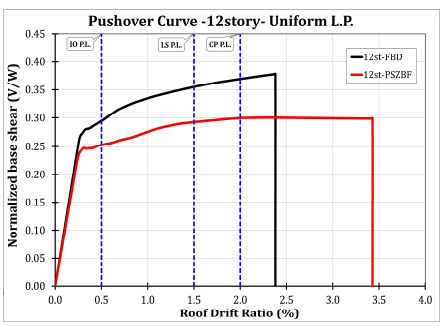

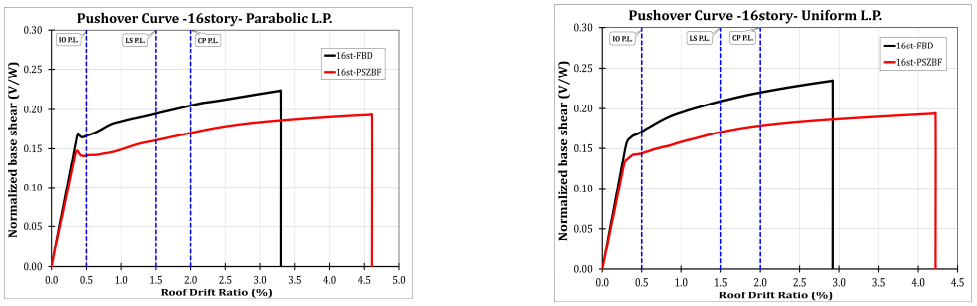

Figure 3. Pushover Curves of Models under Uniform and Parabolic Load Patterns

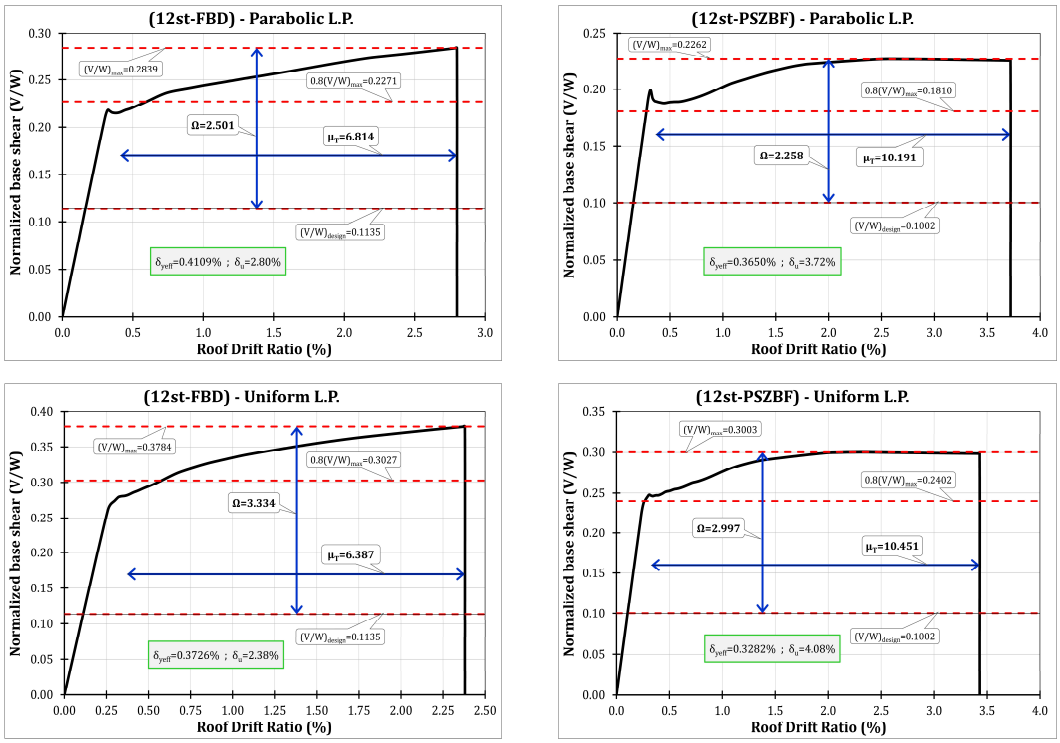

Figure 4. Seismic Performance Parameters of 12-Story Models

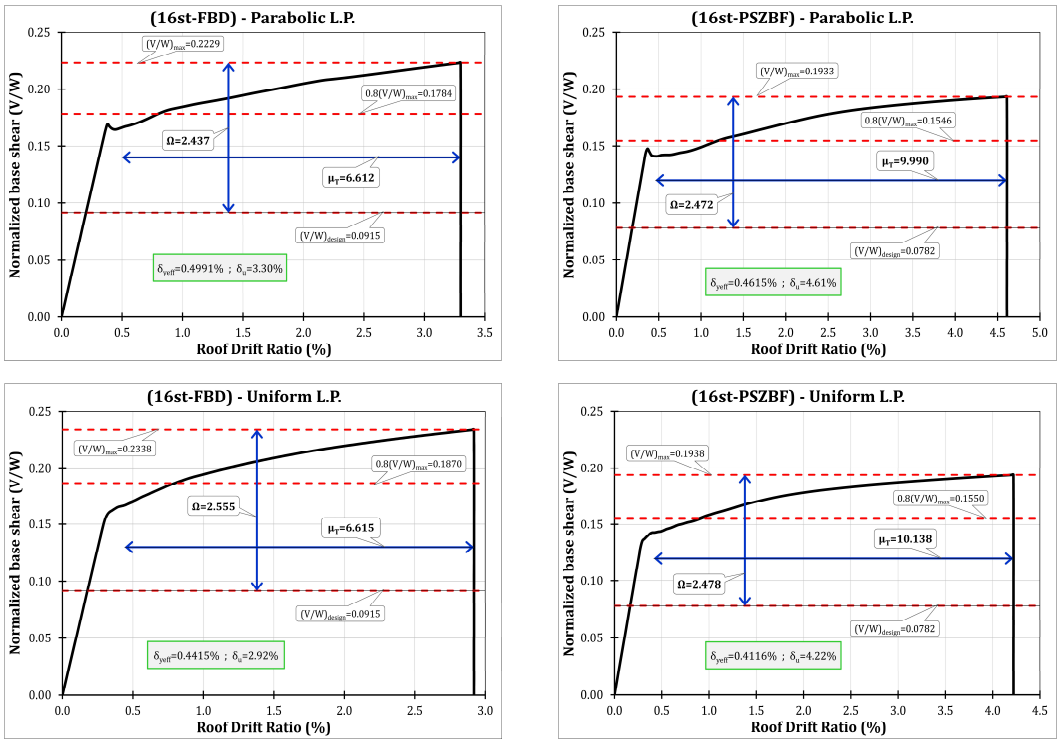

Figure 5. Seismic Performance Parameters of 16-Story Models

3. Conclusions

In order to compare the structural performance of the SZBF equipped with proposed hybrid damper designed by the PBPD method with the conventional SZBF, two high-rise 12- and 16-story SZBFs were designed according to these two cases. A comparative study of the models with nonlinear static analysis clearly shows the following results:

(1) Using the PBPD design method instead of the FBD method reduces the steel consumption by approximately 5.5-7.3% in the SZBF, which is expected to decrease further with the increasing number of stories.

(2) Since the PBPD method results in a weaker design of columns and braces than the FBD method by about 5-10%, the elastic stiffness of the PSZBF models is about 5% lower than the FBD models, that the elastic stiffness in both models can be assumed to be equal.

(3) Although PSZBF models have lower maximum lateral resistance than FBD models, they are able to absorb energy about 25% more in addition to increasing collapse lateral displacement.

4. References

[1] CEN - EN 1998-1, Eurocode 8, Design Provisions for Earthquake Resistance of Structures,
"Part 1: General Rules, Seismic Actions and Rules for Buildings", European Committee for Standardization, Brussels, 2007.

[2] AISC-LRFD, American Institute of Steel Construction, "Load and Resistance Factor Design Specification for Structural Steel Buildings", Chicago, USA, 2016.

[3] Rajeev, P., Wijesundara, K.K., "Energy-based damage index for concentrically braced steel structure using continuous wavelet transform", Journal of Constructional Steel Research, 103:241-250, 2014.

[4] D'Aniello, M., Costanzo, S., Landolfo, R., "The influence of beam stiffness on seismic response of chevron concentric bracings", Journal of Constructional Steel Research, 112:305-324, 2015.

[5] Rai, D.C., Goel, S.C., "Seismic evaluation and upgrading of chevron braced frames", Journal of Constructional Steel Research, 59: 971-994, 2003.

[6] Khatib, I., Mahim, S., Pister, K, "Seismic behavior of concentrically braced steel frames", Earthquake Engineering Research Center, University of California, Berkeley, 1988.

[7] Leon R.T., Yang C.S., "Special Inverted-V-braced Frames with Suspended Zipper Struts". International Workshop on Steel and Concrete Composite Construction", National Center for Research on Earthquake, Taipei, Taiwan, 2003.

[8] Yang, C.S., Leon, R.T., DesRoches, R., "Pushover Response of a Braced Frame with Suspended Zipper Struts", Journal of Structural Engineering, 134: 1619-1626, 2008.

[9] Ozcelik, Y., Saritas, A., Clayton, P.M., "Comparison of Chevron and Suspended-Zipper Braced Steel Frames", Journal of Constructional Steel Research, 119: 169-175, 2016.
[10] Rossi, P.P., Quaceci, G., "A Design Procedure for Suspended Zipper-Braced Frames in the Framework of Eurocode 8", Journal of Earthquake Engineering & Structural Dynamics, 2017.
[11] Wijesundara, K.K., Nascimbene, R., Rassati, G.A., "Evaluation of the Seismic Performance of Suspended Zipper Column Concentrically Braced Steel Frames", Journal of Constructional Steel Research, 150:452-461-2018.
[12] McCormick, J., Aburano, H., Ikenaga, M., Nakashima, M., "Permissible Residual Deformation Levels for Building Structures Considering both Safety and Human Elements', Proceedings of the 14th world conference on earthquake engineering, Beijing, China, 2008, Paper No. 05-06-0071.
[13] ASCE 7-16, American Society of Civil Engineers, "Minimum Design Loads for Buildings and Other Structures", Reston, Virginia, USA, 2016.
[14] ANSI/AISC 360-10, American Institute of Steel Construction, "Specification for Structural Steel Buildings", Chicago, USA, 2010.
[15] IBC, International building code, International Code Council, INC. 2006.
[16] Jani, J.M., Leary, M., Subic, A., Gibson, M.A., "A review of shape memory alloy research, applications and opportunities", Journal of Materials and Design, 56: 1078-1113, 2014.
[17] FEMA-P695, "Quantification of building seismic performance factors", Applied Technology Council for FEMA, Redwood City, California, USA, 2009.
[18] ASCE/SEI 41-06, American Society of Civil Engineers, Structural Engineering Institute, "Seismic Rehabilitation of Existing Buildings", Reston, Virginia, USA, 2006.

INTERNATIONAL JOURNAL OF
COASTAL, OFFSHORE & ENVIRONMENTAL ENGINEERING IJCOE Vol.11/No. 2/Spring 2026 (79-93)

Available online at: www. Ijcoe.org

Integrated Probabilistic Tsunami Hazard and Spectral Energy Analysis of the Makran Subduction Zone: Deriving Hydrodynamic Design Envelopes for Critical Marine Infrastructure near the Strait of Hormuz

Mahmood Reza Akbarpour Jannat[1*]; Mohammad Hossein Kazeminezhad[2]

[1]Iranian National Institute for Oceanography and Atmospheric Science, No.3, Etemad Zadeh St., Fatemi Ave, P.C: 1411813389, Tehran, Iran, *(Corresponding author) E-mail: akbarpour@inio.ac.ir*
[2]Iranian National Institute for Oceanography and Atmospheric Science, No.3, Etemad Zadeh St., Fatemi Ave, P.C: 1411813389, Tehran, Iran, E-mail: mkazeminezhad@inio.ac.ir

ARTICLE INFO

Article History:
Received: 05 Nov 2025
Accepted: 24 Feb 2026

Keywords:
Makran Subduction Zone
Probabilistic Tsunami Hazard Assessment (PTHA)
Hydrodynamic Design Envelopes
Time-Frequency Analysis
Strait of Hormuz

ABSTRACT

The strategic development of energy infrastructure along the Makran Subduction Zone (MSZ), particularly the Kooh Mobarak Terminal near the Strait of Hormuz, demands a rigorous transition from deterministic assessments to risk-informed frameworks. While the eastern MSZ has a well-documented seismic history, the western segment presents a critical latent threat due to strong inter-seismic coupling. This study introduces an integrated framework combining Probabilistic Tsunami Hazard Assessment (PTHA) with advanced time-frequency analysis to quantify multi-dimensional risks. Building upon high-resolution hydrodynamic simulations, site-specific "Hydrodynamic Design Envelopes" were derived to explicitly correlate wave height and current velocity. Results indicate that for the 975-year Maximum Credible Earthquake, the nearshore breakwater faces extreme compound loads, with wave heights approaching 3.0 m and velocities exceeding 2.3 m/s, necessitating a shift to hydrodynamic drag-based design criteria. Furthermore, spectral characterization using Welch's method and Continuous Wavelet Transform (CWT) identifies dominant energy bands at 24–30 and ~64 minutes, providing vital geometric constraints to avoid destructive harbor resonance. Additionally, time-frequency analysis reveals a significant lag between initial arrival and peak energy flux, demonstrating that hazardous agitation persists for over 4 hours. These findings underscore the imperative of adopting a performance-based design philosophy that accounts for probabilistic exceedance, resonance avoidance, and extended operational exclusion windows.

1. Introduction

The strategic expansion of critical energy infrastructure along coastal margins, particularly in tectonically complex regions like the northwestern Indian Ocean, necessitates a paradigm shift in natural hazard assessment. We are moving from deterministic, single-scenario analyses toward comprehensive, risk-informed frameworks that account for the stochastic nature of extreme events. The Makran Subduction Zone (MSZ), stretching approximately 900 km along the coasts of Iran and Pakistan, represents a formidable tsunamigenic structure formed by the northward subduction of the Arabian Plate beneath the Eurasian Plate. Characterized by an exceptionally thick accretionary wedge and a shallow dip angle, the MSZ possesses the geomorphological capacity to generate mega-thrust earthquakes exceeding Mw 8.5. The catastrophic tsunami of November 28, 1945 (M_w 8.1), which claimed over 4,000 lives and devastated the coasts of Pakistan, Iran, and Oman, serves as a stark historical benchmark (Heidarzadeh et al., 2008; Rajendran et al., 2008). However, the scarcity of instrumental records for earlier events, combined with the long recurrence intervals of mega-thrust ruptures, introduces significant epistemic uncertainty into hazard estimations. For the rapidly industrializing Iranian coastline, specifically the Oil Terminal situated near the strategic chokepoint of the Strait of Hormuz, the

potential for a large-scale tsunami poses a dual threat: an immediate risk to coastal assets and a broader strategic risk to global energy security. Consequently, ensuring the resilience of complex marine facilities such as breakwaters, jetties, and Moorings requires a rigorous quantification of hazard that transcends historical retrospection.

Traditionally, tsunami hazard assessments in the Makran region have predominantly relied on Deterministic Tsunami Hazard Assessment (DTHA). These approaches simulate specific "worst-case" scenarios based on maximum credible earthquakes to define ultimate limit states for inundation mapping. In a recent companion study, Kazeminezhad et al. (2026) provided a high-resolution deterministic assessment for the Kooh Mobarak region. That investigation was pivotal in identifying the critical threat posed by the western Makran segment, a region previously considered a "seismic gap", and highlighted the compound risks of tidal interactions. While deterministic scenarios are essential for emergency response planning and understanding the physical upper bounds of flooding, they inherently lack the temporal dimension of risk. They do not quantify the probability of exceedance over the operational lifespan of a structure, typically 50 to 100 years for critical infrastructure. Engineering stakeholders require probabilistic metrics to optimize capital investment against risk, balancing safety with economic viability. This necessitates a Probabilistic Tsunami Hazard Assessment (PTHA) that integrates seismic recurrence rates with hydrodynamic modeling to derive hazard curves, thereby addressing the aleatory variability in source characteristics.

Over the past decade, the scientific community has made significant strides in quantifying the probabilistic tsunami hazard in the Makran region. Heidarzadeh and Kijko (2011) conducted one of the pioneer PTHA studies for the entire MSZ using Monte Carlo simulations, estimating the probability of wave heights exceeding 5 meters. Subsequently, El-Hussain et al. (2016) applied a logic-tree approach to account for epistemic uncertainties in source parameters for the Omani coast. As computational power increased, recent studies have moved towards stochastic source modeling to capture rupture complexities. Rashidi et al. (2020) and Salah et al. (2021) incorporated heterogeneous slip distributions to refine hazard estimates for the eastern and central Makran. More specifically targeting the Iranian coast, Zafarani et al. (2022) performed a PTHA for the western Makran, providing valuable return period estimates for coastal cities. Most recently, Momeni and Goda (2024) presented a comprehensive PTHA using logic trees and stochastic rupture sources, investigating uncertainties associated with segmentation, geometry, and slip heterogeneity. Their work represents the current state-of-the-art, highlighting that tsunami heights are highly sensitive to the location of large slip areas and nearshore bathymetry.

Despite these advancements, a critical gap persists in the existing literature, including the most recent probabilistic studies. The vast majority of PTHA efforts in the region focus almost exclusively on maximum wave amplitude (run-up) as the primary intensity measure. While wave height is the governing parameter for flood mapping and crest elevation design, it fails to capture the spectral characteristics, time-frequency evolution, and kinetic energy of the tsunami wave train. Tsunami waves are not solitary pulses; they are broadband signals containing energy across a wide range of frequencies. When these long-period waves interact with the shallow continental shelf and semi-enclosed water bodies like harbor basins, the phenomenon of resonance can occur. If the dominant period of the incoming wave train aligns with the fundamental natural frequency of the harbor (Helmholtz mode), amplification factors can far exceed those predicted by simple run-up models (Rabinovich, 2009). This resonant response can induce severe harbor agitation and dangerous currents, disrupting port operations and causing damage to moored vessels even when the incident wave height appears manageable. Furthermore, for offshore structures like Moorings, the hydrodynamic drag force, which scales with the square of current velocity (V^2), is often the failure mechanism, yet probabilistic assessments of current velocity remain rare.

The application of advanced signal processing techniques to tsunami hazard assessment in the Makran region remains largely unexplored. Techniques such as the Fast Fourier Transform (Welch's Method) for identifying dominant energy bands and the Continuous Wavelet Transform (CWT) for analyzing the temporal localization of this energy are standard in other fields but absent in Makran tsunami studies. Understanding not just *how high* the wave is, but *when* the peak energy arrives, *what frequencies* it carries, and *how long* it persists in resonance-prone bands, is vital for defining operational downtime windows and resilience strategies.

This study aims to bridge the gap between traditional probabilistic assessments and advanced hydrodynamic characterization, providing a holistic framework for coastal resilience at the Kooh Mobarak terminal. Building upon the validated numerical models of the companion study (Kazeminezhad et al., 2026), this research shifts the focus from "what is possible" to "what is probable" and "how the energy evolves." The specific contributions of this paper are threefold. Firstly, we develop high-resolution hazard curves and novel hydrodynamic design envelopes for the Kooh Mobarak terminal, explicitly correlating wave height and current velocity for return periods relevant to

engineering design (475 and 975 years). This facilitates a "Performance-Based Design" approach where different limit states (serviceability vs. ultimate) are checked against different hazard levels. Secondly, we employ spectral analysis using Welch's method to identify the dominant periods of the expected tsunami waves and calculate the critical resonant lengths for future port basins, providing a proactive geometric constraint for harbor designers. Finally, utilizing Wavelet analysis, we visualize the time-frequency evolution of the tsunami energy, quantifying the duration of hazardous conditions. This integration of PTHA with spectral analysis provides a robust scientific basis for the safe development of strategic infrastructure in the Strait of Hormuz region.

2. Study Area and Tectonic Context

The geographical focal point of this research is the coastal zone of Kooh Mobarak and the adjacent Oil Terminal (OT), situated strategically at the entrance to the Strait of Hormuz in southeastern Iran (approximate coordinates: 25.85°N, 57.27°E). As illustrated in Figure 1, this region represents a pivotal node in the global energy transit network. The development of the OT serves as a critical strategic asset, facilitating the export of crude oil directly into the Gulf of Oman and effectively bypassing the potential chokepoint of the Strait of Hormuz. Given the high-value infrastructure involved, including storage tanks, moorings (Ms), and extensive breakwater systems, and the dense concentration of maritime traffic, the resilience of this zone against extreme hydrodynamic loads is of paramount national and international importance. The coastal geomorphology of Kooh Mobarak is characterized by a relatively wide continental shelf and a complex network of tidal creeks (Khors), features that can significantly modulate tsunami wave amplification and inundation patterns. To accurately capture these local bathymetric influences, the study area is enclosed within a high-resolution computational grid, which allows for detailed hydrodynamic modeling of nearshore interactions.

Tectonically, the study area lies directly north of the Western Makran Subduction Zone (W-MSZ), an active convergent boundary where the dense oceanic lithosphere of the Arabian Plate subducts beneath the continental Eurasian Plate. Geodetic measurements indicate a convergence rate increasing from approximately 19.5 mm/yr in the eastern Makran to roughly 27 mm/yr in the western segment (Vernant *et al*., 2004). This subduction process has resulted in the formation of an exceptionally thick accretionary sediment wedge (exceeding 7 km), a geological feature associated with the generation of tsunamis characterized by long periods and significant run-up potentials. The MSZ is structurally segmented into three distinct rupture zones: Western, Central, and Eastern Makran (Figure 1). While the eastern segment (offshore Pakistan) has a well-documented history of major tsunamigenic earthquakes, most notably the catastrophic 1945 M_w 8.1 event, the western segment adjacent to Jask has experienced a prolonged period of seismic quiescence spanning several centuries. This lack of historical seismicity has led to its classification as a "seismic gap" (Byrne *et al*., 1992).

However, the absence of recent large earthquakes in the Western Makran should not be misinterpreted as a lack of hazard. Recent inversions of GPS velocity fields and elastic block modeling suggest a high degree of inter-seismic coupling (locking) along the plate interface in this region (Frohling and Szeliga, 2016). This indicates that the fault is accumulating significant elastic strain, rather than releasing stress through aseismic creep, thereby possessing the potential to generate megathrust earthquakes exceeding M_w 8.5. To operationalize this tectonic framework for Probabilistic Tsunami Hazard Assessment (PTHA), the fault interface is conceptualized as a geometric grid of rectangular unit sources (sub-faults), superimposed on the physical map in Figure 1. This discretization comprises two parallel rows aligned with the trench strike: the shallow 'a-series' representing the up-dip interface closer to the deformation front, and the deeper 'b-series' corresponding to the down-dip interface. This configuration allows for the simulation of heterogeneous slip distributions and the definition of location-specific rupture scenarios, ranging from localized western events to full-margin ruptures, that form the basis of the probabilistic source model employed in this study.

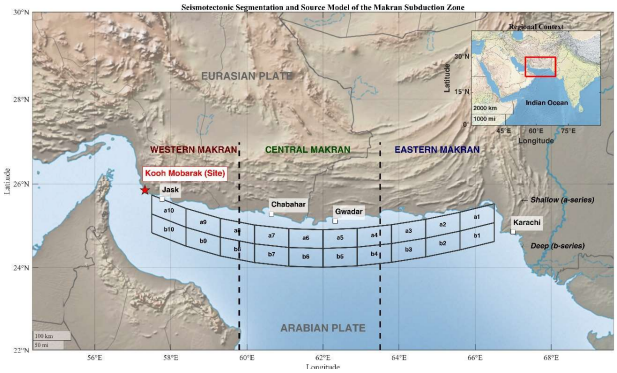

Figure 1. Seismotectonic setting and source characterization model of the Makran Subduction Zone (MSZ). The map illustrates the tripartite segmentation of the margin into Western, Central, and Eastern Makran sectors, separated by vertical dashed boundaries. The superimposed rectangular grid depicts the spatial discretization of the fault interface used for the probabilistic tsunami hazard assessment (PTHA), comprising a shallow 'a-series' (updip interface) and a deeper 'b-series' (downdip interface). The red star indicates the strategic location of the Kooh Mobarak project site, situated directly north of the Western Makran seismic gap. (Inset) Regional context of the study area within the northwestern Indian Ocean basin.

3. Methodology

3.1 Numerical Modeling Framework

To derive the extensive hydrodynamic dataset required for the Probabilistic Tsunami Hazard Assessment

Table 1. Seismogenic source parameters and statistical recurrence rates for the deterministic fault rupture scenarios used in the PTHA framework.

Magnitude (Mw)	Mean Annual Rate(λ) [1/yr]*	Slip (u) [m]	Rupture Dimensions (L×W) [km]	Seismic Moment (M_0) [N·m]	Scenario ID**
8.0	0.0080	4.0	200 × 50	1.26×10^{21}	M8.0-W M8.0-C M8.0-E
8.4	0.0038	10.0	300 × 50	4.47×10^{21}	M8.4-W M8.4-C M8.4-E
8.7	0.0021	17.0	500 × 50	1.26×10^{22}	M8.7-W M8.7-C M8.7-E
8.9	0.0013	23.0	700 × 50	2.51×10^{22}	M8.9-W M8.9-E
9.0	0.0011	27.0	900 × 50	3.55×1022	M9.0-C

*Mean annual rates (λ) are derived from the return periods (T) provided by El-Hussain et al. (2016), calculated as $\lambda = 1/T$
** The suffixes W, C, and E in the Scenario ID denote the Western, Central, and Eastern segments of the Makran Subduction Zone, respectively. Seismic moment (M_0) is calculated assuming a shear modulus (μ) of 30 GPa.

(PTHA) and the subsequent spectral analysis, a systematic numerical modeling campaign was executed. The generation, propagation, and coastal inundation phases of the tsunami were simulated using the ComMIT/MOST (Method of Splitting Tsunami) system. Developed by NOAA's Pacific Marine Environmental Laboratory, this model serves as a standard operational tool for tsunami forecasting due to its validated capability to handle trans-oceanic propagation and complex nearshore interactions. The modeling framework employed in this study is underpinned by the Nonlinear Shallow Water Equations (NSWE), formulated in spherical coordinates to explicitly account for the Earth's curvature, which becomes increasingly significant over the large spatial scales of the Makran Subduction Zone. The hydrodynamic solver is governed by the fundamental principles of conservation of mass and momentum, incorporating terms to represent the Coriolis force and bottom friction. The frictional dissipation is parameterized using the Manning's roughness coefficient, which was set to a standard value of 0.025 $m^{-1/3}s$ for the nearshore domain to represent the seabed roughness characteristics of the region. Rather than solving the fully coupled system simultaneously, the model utilizes a dimensional splitting numerical scheme. This algorithm decomposes the governing equations into two orthogonal one-dimensional problems, which are solved sequentially. This approach significantly optimizes computational efficiency without compromising numerical stability, allowing for the simulation of long-duration wave trains necessary for spectral analysis. For a detailed mathematical derivation of the governing equations and the specific numerical discretization techniques employed, the reader is referred to the foundational work of Titov and Synolakis (1998) and the comprehensive methodology presented in our companion study, Kazeminezhad et al. (2026).

The reliability of nearshore hydrodynamic estimates is intrinsically linked to the resolution of the spatial discretization and the quality of the bathymetric data. To bridge the scale gap between the basin-wide propagation in the Indian Ocean and the localized wave transformation at the Kooh Mobarak coastline, a dynamic nested grid strategy was implemented. As illustrated in Figure 2, the computational domain is structured into three telescoping grids that progressively refine the spatial resolution. The outermost regional grid (Grid A) encompasses the entire Northern Indian Ocean with a resolution of 2 arc-minutes, sufficient to capture the source generation and initial directivity of the tsunami energy. Nested within this is the intermediate grid (Grid B), which focuses on the Gulf of Oman and the entrance to the Strait of Hormuz with a resolution of 30 arc-seconds, resolving the shelf slope processes. Finally, the innermost local grid (Grid C) targets the specific study area of Kooh Mobarak and the Jask terminal with a high-resolution

mesh of 3 arc-seconds (approximately 90 meters). This fine-scale resolution is critical for accurately resolving the non-linear shoaling effects, flow constriction around breakwaters, and the run-up onto the complex coastal topography. The bathymetric and topographic data driving these grids were constructed by seamlessly integrating the GEBCO global dataset for deep waters with high-resolution SRTM digital elevation models and local hydrographic surveys for the nearshore zone, ensuring a continuous and artifact-free representation of the seafloor.

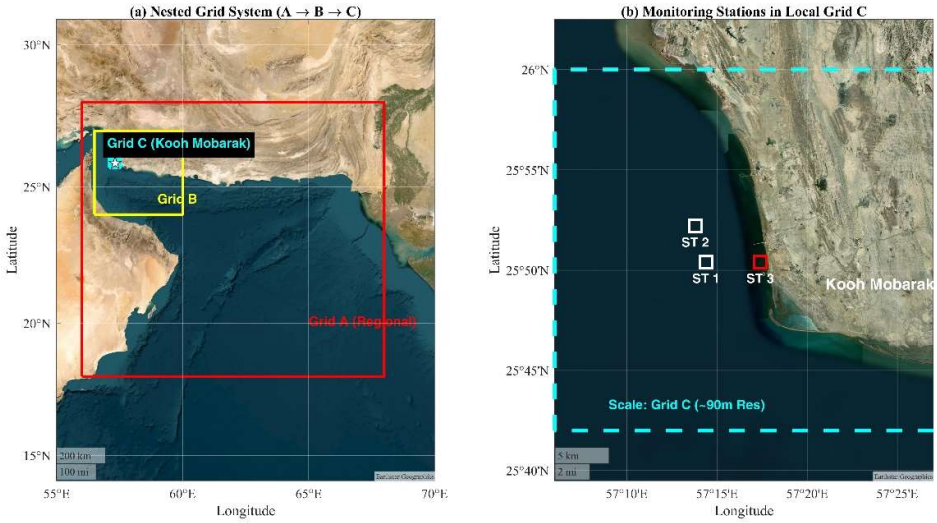

Figure 2. Configuration of the computational domains and monitoring stations employed for the hydrodynamic simulations. (a) The nested grid system hierarchy consisting of three dynamically coupled layers: the regional Grid A (covering the Northern Indian Ocean), the intermediate Grid B (focusing on the Gulf of Oman), and the high-resolution local Grid C (targeting the Kooh Mobarak coastal zone). (b) Detailed view of the local Grid C domain, illustrating the spatial distribution of virtual gauge points relative to the coastline. Stations ST 1 and ST 2 are positioned in the offshore zone (~50 m depth) to capture deep-water wave characteristics, while ST 3 is located in the nearshore zone (~10 m depth) adjacent to the nearshore to assess shoaling amplification and impact loads.

Within this high-resolution local domain, specific virtual monitoring stations were established to extract the time-series data necessary for the subsequent spectral and probabilistic analyses. As depicted in Figure 2b, three strategic locations were selected to capture the hydrodynamic regime transition. Stations ST 1 and ST 2 are situated in the offshore zone at water depths of approximately 45 to 50 meters, representative of the operational environment for Single Point Moorings (SPMs) and deep-draft tanker navigation. Conversely, station ST 3 is located in the nearshore zone at a depth of roughly 10 meters, immediately adjacent to the nearshore of Kooh Mobarak. This spatial configuration allows for a distinct comparative analysis of how the tsunami hazard amplifies as the waves transition from the linear deep water regime to the non-linear shallow water regime. The time histories of water surface elevation and depth averaged current velocity recorded at these stations form the raw input for the spectral energy density calculations and the construction of the hazard curves.

The probabilistic framework of this study is founded upon a suite of twelve deterministic fault rupture scenarios, defined to encapsulate the epistemic and aleatory uncertainties inherent in the seismic source characterization. As summarized in Table 1, these scenarios span a comprehensive range of moment magnitudes from M_w 8.0 to 9.0, spatially distributed across the Western, Central, and Eastern tectonic segments of the Makran trench (shown in Figure 1). To ensure physical consistency, the geometric fault parameters for each scenario, including rupture length, width, and average slip, were derived from the empirical scaling laws of Wells and Coppersmith (1994). The maximum hydrodynamic values (peak wave height and peak current velocity) extracted from these twelve deterministic simulations serve as the primary dataset. By weighting these deterministic outputs with their respective mean annual recurrence rates, we construct the probabilistic hazard curves and design envelopes that constitute the core findings of this research.

3.2. Seismotectonic Setting and Probabilistic Framework

The foundation of any robust Probabilistic Tsunami Hazard Assessment (PTHA) lies in the accurate characterization of the seismogenic source and the mathematical framework used to quantify the temporal likelihood of extreme events. The Makran Subduction Zone (MSZ) constitutes the active convergent boundary where the dense oceanic lithosphere of the

Arabian Plate subducts beneath the continental Eurasian Plate. This large-scale tectonic process, occurring at a convergence rate increasing from approximately 19.5 mm/yr in the east to roughly 27 mm/yr in the west (Vernant et al., 2004), serves as the primary engine for elastic strain accumulation. Geological evidence suggests that the MSZ is characterized by an exceptionally thick sedimentary wedge (>7 km) and a shallow dip angle. Such a geometric configuration is particularly conducive to generating tsunamigenic earthquakes because it allows rupture propagation into the shallow up-dip portion of the megathrust, potentially leading to large vertical seafloor displacements and significant water column perturbation (Smith et al., 2013). However, the translation of this continuous tectonic loading into discrete seismic release is highly heterogeneous along the strike of the subduction zone. While the eastern segment (offshore Pakistan) has a documented history of large earthquakes, most notably the 1945 M_w 8.1 event, the western segment (offshore Iran), situated directly adjacent to the strategic Strait of Hormuz, has exhibited a puzzling seismic quiescence for several centuries. This "seismic gap" presents a critical challenge for hazard assessment: does the absence of historical seismicity imply aseismic creep, or does it indicate a locked fault late in its seismic cycle? Recent elastic block modeling and GPS velocity fields strongly support the latter, estimating a high degree of interseismic coupling in the western Makran (Frohling and Szeliga, 2016). Therefore, relying solely on historical catalogs would catastrophically underestimate the hazard for the Jask region. Instead, a seismotectonic approach based on the conservation of seismic moment budget is required to estimate recurrence rates.

3.2.1 Seismic Recurrence Rates and Source Characterization

Quantifying the mean recurrence interval (T_r) for potential megathrust ruptures in the MSZ requires synthesizing geodetic data, paleoseismic evidence, and empirical scaling laws. In this study, we adopt the recurrence parameters derived by El-Hussain et al. (2016), who utilized a logic-tree approach to account for epistemic uncertainties in the maximum magnitude (M_{max}) and the b-value of the Gutenberg-Richter relationship. Their model balances the seismic moment accumulation (derived from the ~19 mm/yr convergence rate) with the moment release of characteristic earthquakes, providing a physically consistent basis for PTHA in data-poor regions.

The recurrence model integrated into this study is detailed in Table 1. The framework conceptualizes the MSZ as three segmented rupture zones: Western, Central, and Eastern. This segmentation allows for the spatial differentiation of hazard, ensuring that the specific threat to the Jask terminal from the near-field western segment is explicitly captured. For each tectonic segment, characteristic earthquakes with moment magnitudes (M_w) of 8.0, 8.4, 8.7, and 8.9 are defined to represent a spectrum of energy release scenarios. Furthermore, a "worst-case" full-margin rupture scenario (M_w 9.0) is included in the Central segment to account for the possibility of multi-segment cascading rupture, a phenomenon observed in other subduction zones (e.g., the 2004 Sumatra and 2011 Tohoku events). The estimated mean return periods range from approximately 125 years for moderate tsunamigenic events (Mw 8.0) to 946 years for catastrophic M_w 9.0 events. These values imply that while smaller events are relatively frequent, the accumulation of strain required for a full-scale rupture takes nearly a millennium, consistent with the long seismic gaps observed in the historical record.

3.2.2 The Poissonian Probability Model

The core of the PTHA methodology involves converting the mean recurrence intervals of seismic sources into a probability of exceeding specific hydrodynamic intensity measures (e.g., wave height or current velocity) at the site of interest over a given timeframe. Following standard practice in engineering hazard analysis, the temporal occurrence of tsunamigenic earthquakes is modeled as a Poisson process. The Poisson model assumes that earthquake occurrences are stochastic, memoryless events; meaning the probability of an earthquake occurring in the next interval is independent of when the last earthquake occurred (Heidarzadeh and Kijko, 2011). While time-dependent models (e.g., Brownian Passage Time) might be more physically rigorous for faults with well-known earthquake histories, the large uncertainties surrounding the last rupture date of the western Makran make the time-independent Poisson model the most prudent and robust choice for design purposes.

Under the Poisson assumption, the probability $P(t)$ that at least one earthquake of a specific magnitude class m will occur during a specified exposure time t is expressed as:

$$P(E>0 \mid t, \lambda_m)=1-e^{-\lambda mt} \quad (1)$$

Where $\lambda_m=1/T_r$ represents the mean annual rate of occurrence for the magnitude class m. However, the hazard at a specific coastal site like Jask is not determined by a single scenario but is the aggregate of

risks from all possible sources. Therefore, we calculate the **total mean annual rate of exceedance**, $\Lambda(h)$, for a specific hydrodynamic threshold h (e.g., wave height > 2.0 m). This is achieved by summing the contributions from all N potential rupture scenarios (Western, Central, and Eastern) that are capable of generating waves exceeding h at the site:

$$\Lambda(h) = \sum_{i=1}^{N} v_i \cdot P(H > h \mid Senario_i) \quad (2)$$

In this equation, v_i is the annual rate of occurrence for Scenario i (derived from Table 1), and $P(H> h|Scenario_i)$ acts as a binary indicator function (Heaviside step function): it equals 1 if the deterministic simulation of Scenario i produces a wave height greater than h at the Jask terminal, and 0 otherwise. The hydrodynamic inputs for this aggregation are derived directly from the high-resolution numerical simulations presented in our companion study (Kazeminezhad et al., 2026). In that study, the nonlinear shallow water equations were solved using the validated ComMIT/MOST model over a nested grid system, achieving a resolution of 90 meters in the nearshore zone. By coupling these deterministic hydrodynamic results with the probabilistic recurrence rates, we construct site-specific hazard curves.

This study evaluates the hazard for two distinct exposure times: $t=50$ years and $t=100$ years. The 50-year horizon aligns with the typical design life of standard maritime structures and is used to define "Operating Basis Earthquake" (OBE) conditions. The 100-year horizon is selected to address the extended lifespan and higher safety factors required for critical energy infrastructure like oil terminals, corresponding to "Maximum Design Earthquake" (MDE) considerations. This dual-timeframe approach provides stakeholders with a comprehensive risk profile, facilitating decisions that balance immediate operational continuity with long-term asset survivability.

4. Results and Discussion

4.1 Probabilistic Tsunami Hazard Assessment (PTHA)

Building upon the probabilistic framework established in the preceding section, this portion of the study quantifies the site-specific tsunami hazard for the Kooh Mobarak region and its associated marine facilities. By aggregating the contributions of the twelve deterministic rupture scenarios, weighted by their respective recurrence rates derived from the seismotectonic analysis, we derive a comprehensive risk profile. The results are presented through two complementary analytical lenses: Probability of Exceedance Curves for individual hydrodynamic parameters, and Integrated Hydrodynamic Design Envelopes that correlate wave height and current velocity with standard engineering return periods.

4.1.1 Hazard Curves for Elevation and Velocity

The hazard curves for maximum wave height (H_{max}) and current velocity (V_{max}), illustrated in Figures 3 and 4, reveal a characteristic "stepped" morphology rather than a smooth exponential decay. This stepwise behavior is a direct consequence of the logic-tree approach and the discrete nature of the characteristic earthquake scenarios used in the PTHA, which range from M_w 8.0 to 9.0. Each inflection point on the curve corresponds to the activation of a more severe, albeit less frequent, fault rupture segment, such as the transition from frequent Western Makran events to rare full-margin ruptures. A spatial comparison between the stations reveals a profound bathymetric amplification effect. In the deeper waters characteristic of the offshore zones (ST 1 and ST 2, depths ~45–50 m), the hazard curves decay rapidly. For a 10% probability of exceedance in 50 years, approximating a 475-year return period, the expected wave heights remain moderate, ranging between 0.8 m and 0.9 m, with current velocities staying below 0.5 m/s. This indicates that in the deep-water regime, the tsunami energy remains primarily potential rather than kinetic.

In stark contrast, the nearshore regime represented by the nearshore zone (ST 3, depth ~10 m) exhibits a dramatic intensification of hazard due to shoaling processes. The wave height hazard curve shifts significantly, indicating much higher values for equivalent probability levels. More critically, the velocity hazard curve shows that velocities exceeding 1.5 m/s have a tangible probability of occurrence. This non-linear amplification underscores that determining hazard levels solely based on offshore observation points would drastically underestimate the hydrodynamic loads acting on coastal defense structures.

4.1.2 Hydrodynamic Design Envelopes

To translate these probabilistic findings into actionable engineering criteria, the data were synthesized into "Hydrodynamic Design Envelopes" shown in Figure 5. These dual-axis charts plot both the Design Wave Height and Design Current Velocity as a continuous function of the Return Period (T_r), allowing for a Performance-Based Design (PBD) evaluation at two standard levels: the Operating Basis Earthquake (OBE, 475 years) for serviceability, and the Maximum Credible Earthquake (MCE, 975 years) for ultimate survival. Detailed analysis of the design envelopes

identifies the Breakwater Head as the most critical asset subject to severe loading. At the 475-year return period, the design wave height is calculated at 1.90 m, accompanied by a design current velocity of 1.30 m/s. These values suggest that even for the serviceability limit state, the breakwater armor units must be sized to withstand significant dynamic pressure. As the return period extends to the MCE level of 975 years, the design values escalate to approximately 2.85 m for wave height and over 2.0 m/s for current velocity. Notably, the current velocity curve at ST 3 exhibits a steep gradient between the 100-year and 400-year return periods, implying that once the hazard threshold corresponding to Western Makran ruptures is crossed, the flow regime transitions rapidly from a low-velocity oscillation to a high-velocity hydraulic bore. This necessitates that toe protection designs account for high-shear scouring flows that can destabilize the structure's foundation.

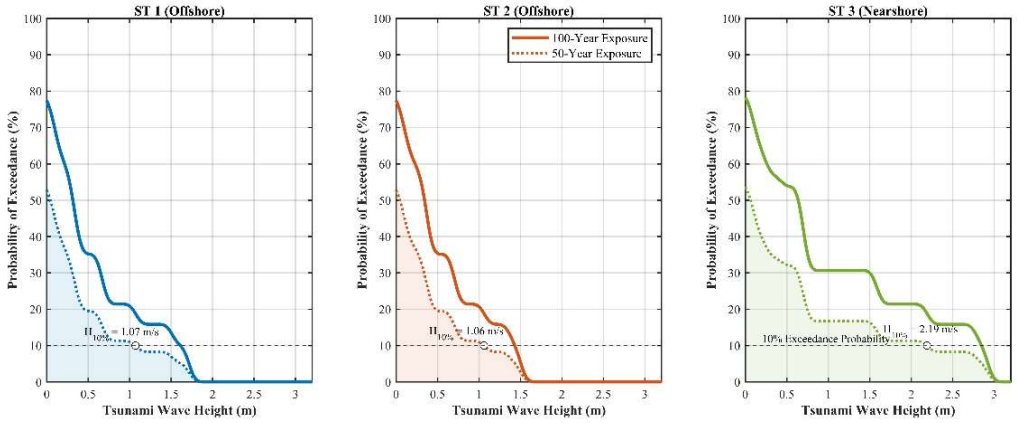

Figure 3. Probabilistic tsunami hazard curves for maximum wave height (H_{max}) at three strategic monitoring stations: ST 1 and ST 2 (Offshore) and ST 3 (Nearshore). The solid and dotted lines represent the probability of exceedance over exposure periods of 100 years and 50 years, respectively. The horizontal dashed line marks the 10% probability of exceedance threshold, with annotated values highlighting the expected wave heights for the 50-year exposure time. Note the significant amplification of hazard at the nearshore station (ST 3) compared to the offshore locations due to shoaling effects.

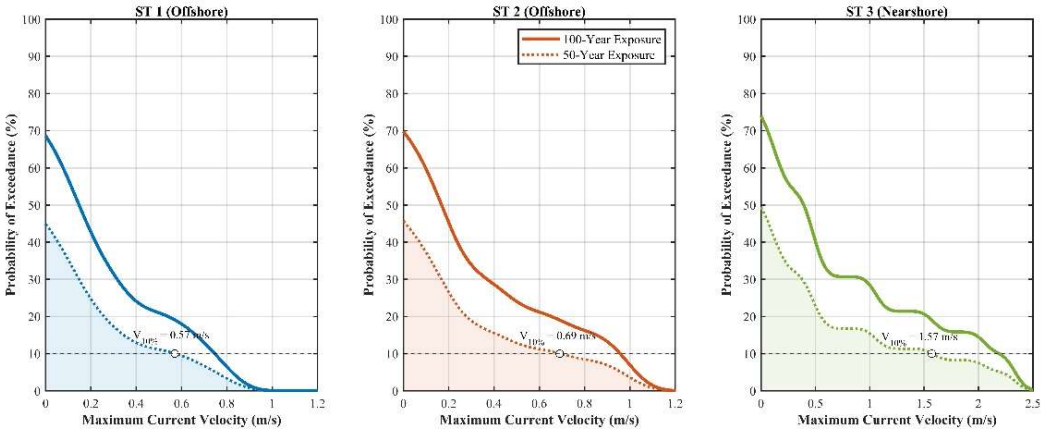

Figure 4. Probabilistic hazard curves for maximum tsunami-induced current velocity (V_{max}) at the designated monitoring stations. Similar to the wave height trends, the nearshore station (ST 3) exhibits a markedly higher probability of experiencing extreme velocities compared to the offshore sites (ST 1 and ST 2). The annotated values corresponding to a 10% probability of exceedance in 50 years (e.g., 1.57 m/s at ST 3 versus ~0.6 m/s offshore) serve as critical inputs for assessing hydrodynamic drag forces and scour potential.

Conversely, the design envelopes for the offshore stations (ST 1 and ST 2) exhibit a fundamentally different hydrodynamic behavior. At ST 1, for the 475-year return period, the design wave height is 0.79 m with a current velocity of 0.43 m/s, while at ST 2, these values are slightly higher at 0.83 m and 0.56 m/s, respectively. Although these wave heights are manageable, the current velocities in the "Low Hazard Zone" are negligible. However, as the return period approaches the MCE event, velocities rise towards 0.8–0.9 m/s. While significantly lower than the nearshore values, these currents acting on the immense hull area of Very Large Crude Carriers (VLCCs) can generate massive hydrodynamic drag forces ($F_D \propto V^2$). Therefore, while the breakwater design is governed by scouring and impact loads, the offshore facility design must prioritize the fatigue limit and peak-load capacity of mooring hawsers and subsea pipeline connections to prevent rupture during rare mega-thrust events.

4.2 Spectral and Time-Frequency Dynamics

While probabilistic hazard curves provide essential metrics for establishing design return periods, they inherently compress the temporal complexity of tsunami waves into single peak values. However, tsunami interaction with coastal infrastructure is a

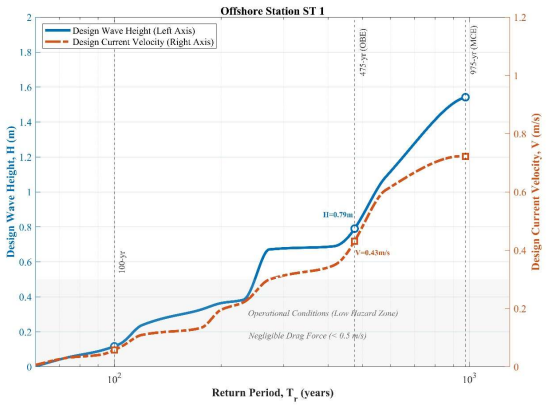

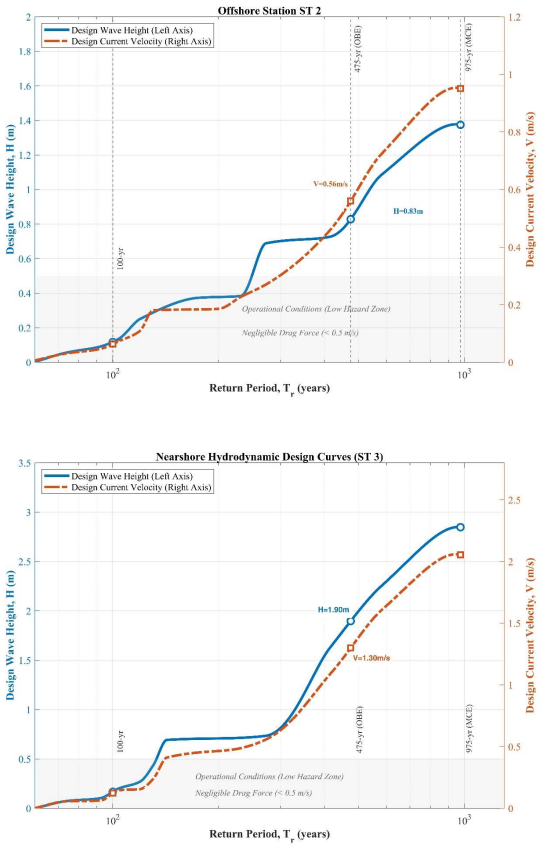

Figure 5. Integrated hydrodynamic design envelopes derived from PTHA for the offshore locations (ST 1 and ST 2), and the nearshore station (ST 3). The dual-axis plots correlate Design Wave Height (solid blue line, left axis) and Design Current Velocity (dashed orange line, right axis) as a function of the Return Period (T_r). Specific design values are annotated for the Operating Basis Earthquake (OBE, 475 years) and Maximum Credible Earthquake (MCE, 975 years). Note the drastic non-linear amplification of current velocity at the nearshore station (ST 3) reaching >2.0 m/s for the MCE, contrasting with the deeper offshore stations where velocities remain largely below 1.0 m/s but are sufficient to induce drag loads on moored vessels. The shaded grey regions indicate the low-hazard operational zone with negligible drag forces.

dynamic process governed not only by amplitude but critically by the frequency content and duration of the wave train. Therefore, this section complements the PTHA by providing a rigorous spectral analysis of the simulated waveforms at the offshore control points (SPM 1), elucidating the energy distribution that drives harbor resonance and operational downtime.

4.2.1 Time-Domain Characteristics and Waveform Complexity

The temporal evolution of the free-surface elevation for the three governing tectonic scenarios, Central Makran

(M_w 9.0), Western Makran (M_w 8.9), and Western Makran (M_w8.7), is visualized in Figure 6. A comparative analysis of these waveforms reveals that the tsunami signature is not a solitary soliton but a complex, dispersive wave train characterized by multiple crests and troughs. A critical hydrodynamic feature observed across all scenarios is the initial phase of the arrival. The waveforms exhibit a distinct leading depression (drawdown) prior to the arrival of the primary crest. For the offshore location, this drawdown reaches approximately -1.4 m for the M9.0-C scenario. This phenomenon is hydrodynamically significant for offshore loading terminals, as unexpected drops in water level can reduce the under keel clearance of deep draft tankers, posing a risk of grounding even before the destructive crest arrives. Furthermore, the time-domain comparison reinforces the findings of the deterministic assessment regarding the "Western Threat." The wave train generated by the Western M_w 8.9 scenario exhibits an amplitude structure and period modulation remarkably similar to the catastrophic Central M_w 9.0 event, with maximum elevations reaching 1.52 m compared to 1.71 m, respectively. This similarity confirms that the proximity of the western rupture zone compensates for the lower seismic moment, generating near-field energy fluxes comparable to far-field mega-thrusts.

4.2.2 Spectral Energy Distribution and Dominant Periods

To identify the frequency bands responsible for potential harbor resonance, the time-series data were transformed into the frequency domain using Welch's Periodogram method. The resulting Energy Spectral Density (ESD) is presented in Figure 7, where the power spectral density is plotted against wave period on a base-2 logarithmic scale to resolve low-frequency components. The spectral analysis uncovers a bi-modal energy distribution characteristic of the Makran basin response. The spectra for all three scenarios are dominated by two distinct energy peaks. The primary peak (T_{p1}) is consistently located at a period of approximately 64.0 minutes, representing the fundamental mode of the continental shelf oscillation

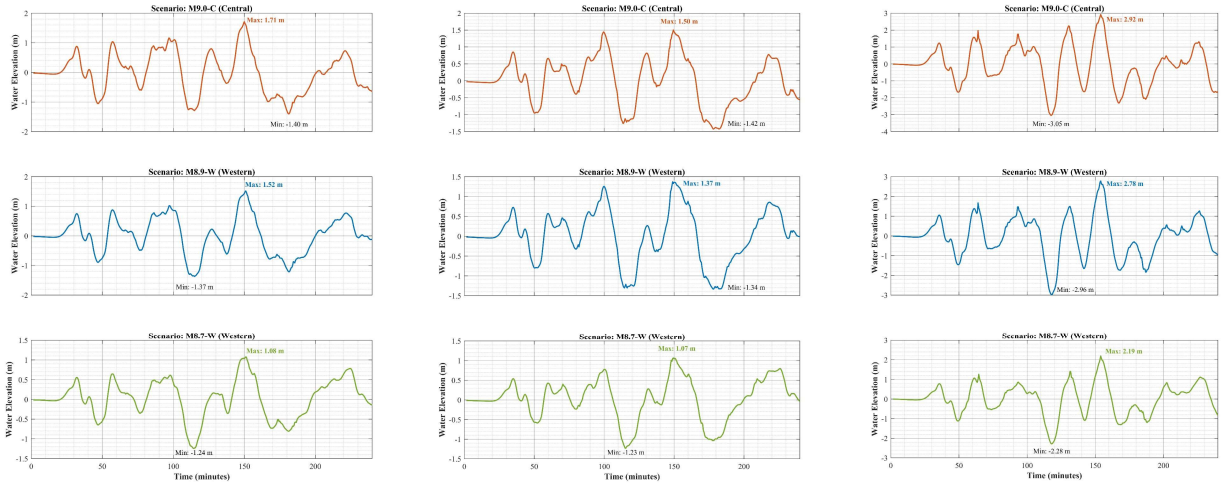

Figure 6. Comparison of simulated tsunami waveforms at the offshore sites (ST 1 and ST 2) and nearshore station (ST 3) for the three governing rupture scenarios from left to right respectively.

or the source duration effect. A secondary, yet highly energetic peak (T_{p2}) is observed in the 24.0 to 30.0-minute band.

The identification of these dominant periods provides a crucial geometric constraint for the design of the future Kooh Mobarak port basin. Semi-enclosed harbors act as high resonators; if the natural eigen-period of the basin aligns with these incoming energy bands, destructive resonance will occur. Specifically, the high energy concentration in the 24–30 minute band is particularly hazardous for medium-sized commercial ports, as it often corresponds to the fundamental Helmholtz mode of basins with typical dimensions (e.g., lengths of 2–3 km). Therefore, port layouts must be dimensioned such that their natural periods are detuned from these critical spectral peaks to prevent amplification of harbor agitation and currents. Comparing the scenarios, the M9.0-C event naturally contains the highest total energy (integral of the curve), yet the M8.9-W scenario follows closely, maintaining

high energy density across the same critical frequency bands, further validating the necessity of considering western ruptures in resonance calculations.

4.2.3 Time-Frequency Evolution of Wave Energy

While the Fourier analysis identifies *which* frequencies carry the most energy, it does not reveal *when* these frequencies arrive or how they evolve over time. To visualize the non-stationary nature of the tsunami, a Continuous Wavelet Transform (CWT) was applied using the Morlet wavelet. Figure 8 presents the resulting wavelet power spectra (scalograms) for the three scenarios. The vertical axis represents the wave period (logarithmic scale), the horizontal axis represents time, and the color intensity signifies the energy density.

The scalograms reveal a distinct frequency dispersion pattern characteristic of distant tsunami propagation. The energy does not arrive as a monochromatic packet; instead, we observe a temporal separation of frequencies. In the Western Makran scenarios (M_w 8.9 and 8.7), the high-frequency components (periods < 15 min) tend to arrive slightly earlier, followed by the high-energy, long-period components (periods > 30 min) which dominate the later phases. This is physically consistent with the physics of wave celerity in dispersive media. Crucially, the "red" zones of high energy are not short-lived flashes but appear as elongated bands stretching horizontally. This indicates that once the resonant frequencies (identified in Section 4.2) enter the domain, they excite the water column for a prolonged duration, likely due to the trapping of edge waves on the continental shelf. The magenta dashed line marks the initial arrival time, clearly showing that the bulk of the destructive energy (the "energy packet") lags behind the leading wave front by nearly an hour, a critical factor for safety protocols.

4.2.4 Hazard Duration in the Resonance Band

Standard spectral analyses, such as the Fourier transform presented in the previous section, assume stationarity and provide a time-averaged view of energy distribution. However, tsunamis are inherently non-stationary transient events where the energy content fluctuates significantly over time. To explicitly quantify the persistence of dangerous hydrodynamic conditions, we employed a Continuous Wavelet Transform (CWT) to compute the Scale-Averaged

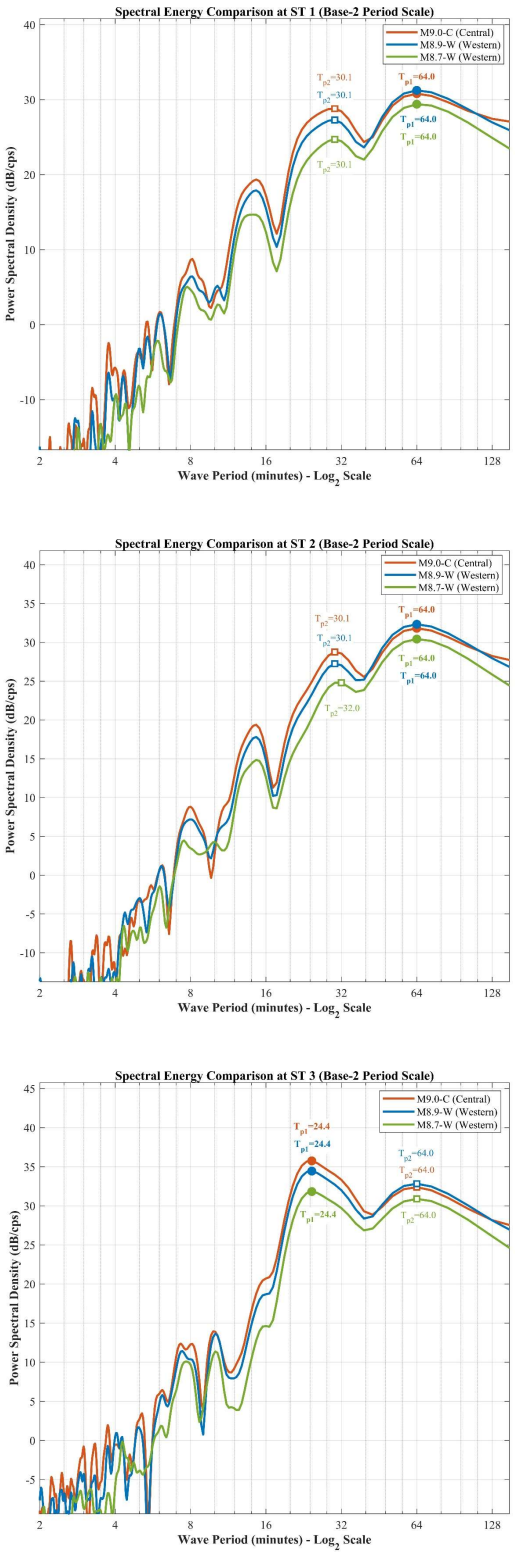

Figure 7. Spectral energy density analysis for Offshore Station (ST 1 and ST 2) (depth∼45-50 m) and nearshore station (ST 3) (depth ∼10 m) , computed using Welch's periodogram method

Wavelet Power (SAP). This analysis focuses specifically on the resonance-prone period band of 8 to 64 minutes, a critical range for medium-to-large harbor basins, as visualized in Figure 9.

A striking feature of the SAP profiles is the significant temporal lag between the initial wave arrival and the attainment of maximum spectral energy. While the leading wave reaches the Kooh Mobarak approximately 30–40 minutes post-rupture, the peak energy flux within the resonance band does not culminate until 2.2 to 2.3 hours after the earthquake. For the Central Makran scenario (M_w 9.0), the peak power occurs at 2.2 hours, whereas for the Western scenarios (M_w 8.9 and 8.7), it occurs slightly later at 2.3 hours. This delay indicates that the most destructive phase of the tsunami, in terms of its capacity to excite harbor oscillations and induce cyclical currents, is not driven by the initial wavefront. Instead, the maximum hydrodynamic stress arises from later wave packets, which are likely reinforced by multipath interference, shelf resonance, and the arrival of edge waves trapped along the continental shelf. This finding challenges the intuitive assumption that the first wave is invariably the most dangerous.

From an operational resilience perspective, the "Hazard Duration" is defined as the interval during which the wave energy exceeds a critical "Harbor Agitation Limit," conservatively set at 10% of the maximum peak power in this study. As depicted by the dashed threshold line in Figure 9, hazardous agitation levels persist for more than 4 hours post-event for all major scenarios. Even for the slightly smaller M_w 8.7 Western scenario, the energy remains above the safety threshold well beyond the 4-hour mark. This prolonged duration of high-energy agitation has profound implications for post-disaster recovery. It suggests that maritime operations, such as the movement of support vessels or the re-berthing of tankers, cannot resume immediately after the passage of the initial wave train. Rather, a significant "exclusion window" of at least 5 to 6 hours must be enforced to ensure that the resonant energy within the basin has sufficiently decayed to levels safe for navigation and mooring operations.

4.3 Engineering Implications and Design Constraints

The integration of probabilistic hazard curves, spectral energy analysis, and momentum flux calculations provides a holistic set of constraints for the design and operation of the Kooh Mobarak future Terminal. Unlike conventional approaches that rely solely on

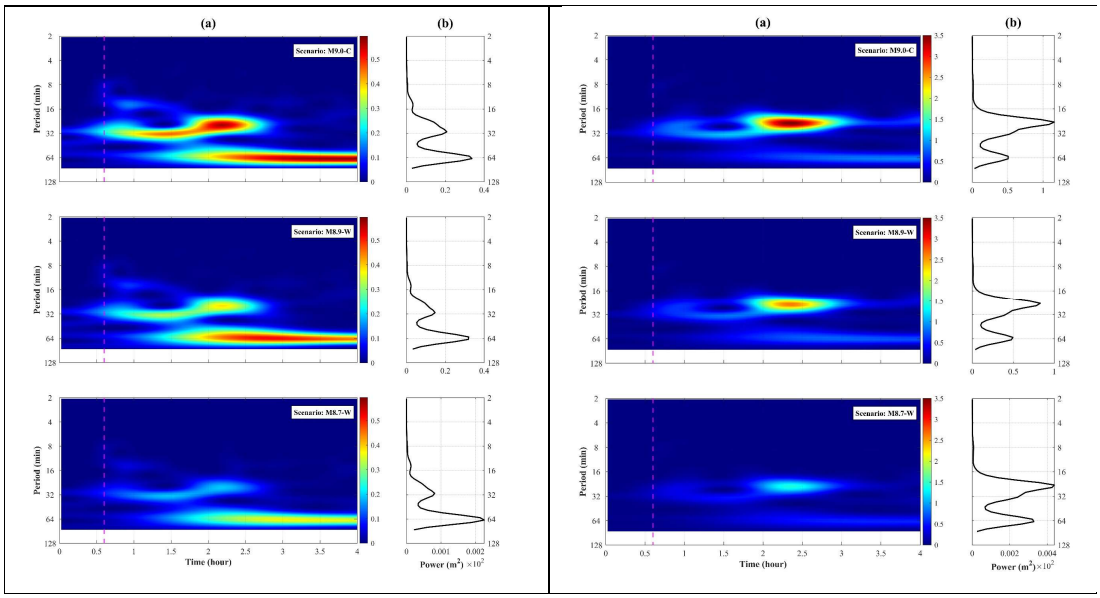

Figure 8. Time-frequency analysis of the tsunami wave train at the offshore station (ST 1) (left panel) and nearshore station (ST 3) (right panel) using Continuous Wavelet Transform (CWT). The figure compares the spectral energy evolution for three governing rupture scenarios: Top row: Central Makran (M_w 9.0), Middle row: Western Makran (M_w 8.9), and Bottom row: Western Makran (M_w 8.7). (a) Wavelet Power Spectrum (Scalogram). (b) Global Wavelet Spectrum. The vertical dashed magenta line indicates the initial tsunami arrival time (≈0.6 hours)

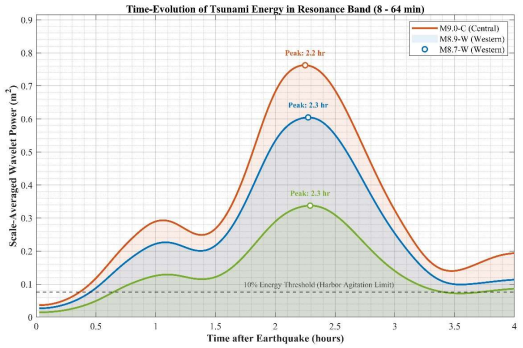

Figure 9. Temporal evolution of tsunami energy within the critical resonance frequency band (periods of 8–64 minutes), calculated via Scale-Averaged Wavelet Power (SAP). The curves depict the energy flux for the three governing rupture scenarios: Central Makran (M_w 9.0), Western Makran (M_w 8.9), and Western Makran (M_w 8.7).

wave height, this study advocates for a multi-dimensional design philosophy that explicitly accounts for hydrodynamic force intensity, geometric resonance avoidance, and operational downtime windows.

4.3.1 Structural Vulnerability based on Momentum Flux

The stability of coastal structures, particularly breakwaters and quay walls, is more fundamentally governed by the Specific Momentum Flux ($M_F = hV^2$) than by flow depth alone. This parameter serves as a direct proxy for the hydrodynamic drag force and the potential for structural dislodgement. Figure 10 synthesizes the probabilistic hazard into a "Destructive Potential Curve," plotting specific momentum flux against the return period. The curve reveals a highly non-linear escalation of force, necessitating distinct design strategies for different performance levels.

4.3.1.1 Serviceability Limit State (OBE - 475 Years):

At the Operating Basis Earthquake level (475-year return period), the specific momentum flux reaches approximately 3.0 m^3/s^2 . As illustrated in the figure, this value falls within Zone II (Moderate Structural Damage). From an engineering perspective, this implies that under OBE conditions, the breakwater armor units may experience partial displacement, and scour protection aprons will be subjected to significant shear stresses. Consequently, the design must ensure that such damage is "repairable" and does not compromise the core integrity of the port basin or lead to immediate operational shutdown. The armor layer weight calculations (e.g., using the Hudson or Van der Meer formulas) should utilize the velocity component derived from this flux value (V ≈ 2.1m/s) rather than assuming a static standing wave.

4.3.1.2 Ultimate Limit State (MCE - 975 Years):

For the Maximum Credible Earthquake (975-year return period), the hazard trajectory rises sharply into Zone III (Critical/Heavy Damage), with the momentum flux peaking at 12.3 m^3/s^2. This represents a four-fold increase in destructive force compared to the OBE level, despite the return period only doubling. This extreme flux indicates a potential for massive hydraulic loading capable of dislodging heavy concrete armor units (e.g., Antifer or Xbloc) and causing catastrophic scouring. Therefore, the design criterion for the MCE event must shift from "damage control" to "collapse prevention." To mitigate this risk, it is recommended to employ composite breakwater designs with reinforced toe protection and to consider the use of high-density concrete units for the most exposed sections of the breakwater head.

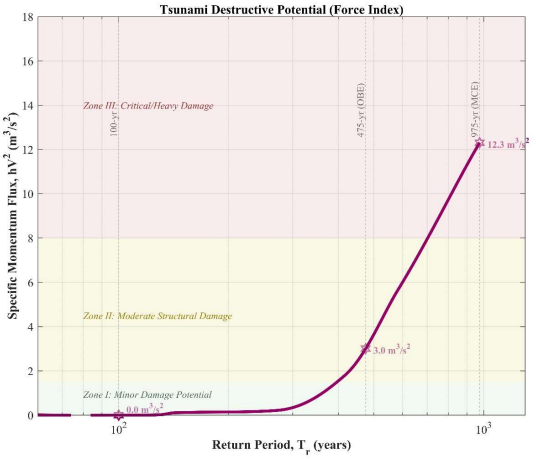

Figure 10. Probabilistic assessment of tsunami destructive potential at the nearshore station, quantified by the Specific Momentum Flux (M_F=hV^2). The curve correlates the hydrodynamic force index with the return period, overlaid on empirical damage severity zones. Key design points are highlighted as Zone I (Green): Minor damage potential, relevant for frequent events (<100 years), Zone II (Yellow): Moderate structural damage, encompassing the Operating Basis Earthquake (OBE, 475-yr) with a flux of 3.0 m^3/s^2 that indicates that armor units may experience displacement but the structure retains core stability and Zone III (Red): Critical/Heavy damage, encompassing the Maximum Credible Earthquake (MCE, 975-yr) where the flux surges to 12.3 m^3/s^2

4.3.2 Geometric Tuning for Resonance Avoidance

Beyond structural strength, the layout of the port basin itself serves as a passive defense mechanism. The spectral analysis (Section 4.2.2) identified two dominant tsunami energy bands centered around 24–30 and 64 minutes. To prevent destructive harbor

resonance, the characteristic dimensions of the future basin must be "detuned" from these incoming frequencies. Utilizing the quarter-wavelength resonator principle derived in this study, port planners must avoid basin lengths that correspond to the critical resonant lengths (L_{crit}). Specifically, any proposed layout with a fundamental axis length approaching the values calculated in Section 6.2 should be modified, either by altering the dredging depth or changing the breakwater configuration, to shift the harbor's natural frequency away from the tsunami's high-energy spectral peaks. This proactive "geometric tuning" is a cost-effective non-structural mitigation strategy that significantly reduces the amplification of currents inside the basin.

4.3.3 Operational Resilience and Recovery

Finally, the time-frequency analysis (Section 4.2.3) dictates the protocols for emergency response and business continuity. The findings demonstrated that hazardous energy levels persist in the resonance band for over 4 hours, with the peak intensity occurring roughly 2.3 hours after the earthquake. This implies that the "All Clear" signal cannot be issued immediately after the first wave recedes. For the Jask terminal, an exclusion window of at least 6 hours post-event is recommended before allowing support vessels to re-enter the harbor or attempting to re-moor tankers. Furthermore, given the "leading depression" characteristic observed in the time-domain analysis, rapid-response protocols must mandate the immediate emergency unberthing of vessels to deeper waters (>50 m depth) to avoid hull grounding damages during the initial drawdown phase.

5. Conclusion

This study establishes a comprehensive, risk-informed framework for the protection of critical energy infrastructure in the northwestern Indian Ocean, specifically focusing on the Kooh Mobarak future Terminal near the strategic Strait of Hormuz. By integrating a high-resolution Probabilistic Tsunami Hazard Assessment (PTHA) with advanced spectral and time-frequency analyses, the research transcends traditional deterministic limitations to provide a multi-dimensional understanding of the tsunami threat. The investigation yields pivotal insights into the recurrence of extreme events, the hydrodynamic transformation of waves, and the frequency-dependent response of coastal basins.

The probabilistic analysis reveals that the tsunami hazard at Jask is governed by a complex interplay between source proximity and bathymetric amplification. The derived hazard curves exhibit a characteristic stepped morphology, reflecting the contribution of distinct tectonic segments ranging from frequent moderate earthquakes to rare mega-thrust events. A critical finding is the profound disparity between offshore and nearshore hazards; while offshore conditions are relatively benign, the nearshore zone experiences a drastic non-linear amplification of hydrodynamic forces. The developed Hydrodynamic Design Envelopes quantify this risk, establishing clear performance-based criteria. For the Serviceability Limit State (OBE, 475-year return period), the breakwater must withstand specific momentum fluxes corresponding to Zone II (Moderate Damage), requiring designs that allow for repairable displacement of armor units. Conversely, for the Ultimate Limit State (MCE, 975-year return period), the hazard escalates into Zone III (Critical Damage), where the momentum flux quadruples. This necessitates a design philosophy focused on collapse prevention through the use of high-density concrete armor units and reinforced toe protection to resist extreme scouring velocities exceeding 2.3 m/s.

Beyond amplitude and velocity, the spectral analysis using Welch's method uncovers the hidden frequency-domain risks. The identification of dominant energy peaks in specific period bands provides a crucial geometric constraint for future port development. To prevent destructive resonance, it is imperative that the characteristic dimensions of the port basin be "detuned" from these incoming spectral peaks. Furthermore, the time-frequency analysis via Continuous Wavelet Transform (CWT) challenges the conventional assumption that the initial wave arrival marks the moment of maximum danger. The results demonstrate a significant temporal lag, with the peak energy flux in the resonance band culminating approximately 2.3 hours after the earthquake and hazardous agitation persisting for over 4 hours. This finding dictates that emergency response protocols must enforce an extended exclusion window for maritime operations, prioritizing the evacuation of vessels to deep waters to avoid grounding during the leading depression phase and delaying re-entry until the resonant energy has sufficiently decayed.

Finally, the sensitivity analysis reinforces the necessity of a "Dual-Criterion" design approach for macrotidal regions. The study confirms that while the Mean High Water Springs (MHWS) condition represents the governing scenario for flood inundation and crest elevation due to higher total water levels, the Mean Sea Level (MSL) condition governs the design of scour protection systems due to higher particle velocities. Collectively, these findings advocate for a paradigm shift in the design codes for the Makran region, moving from single-scenario checks to a holistic resilience strategy that accounts for probabilistic exceedance, spectral resonance, and compound tidal interactions. This framework serves as a robust blueprint for

securing strategic assets against the multi-faceted threat of tsunamis in the 21st century.

References

Byrne, D. E**.,** Sykes, L. R., & Davis, D. M. (1992). Great thrust earthquakes and aseismic slip along the plate boundary of the Makran subduction zone. *Journal of Geophysical Research: Solid Earth*, 97(B1), 449-478.

El-Hussain, I., Omira, R., Deif, A., Al-Habsi, Z., Al-Rawas, G., Mohamad, A., ... & Baptista, M. A. (2016). Probabilistic tsunami hazard assessment along Oman coast from submarine earthquakes in the Makran subduction zone. *Arabian Journal of Geosciences*, 9(1), 1-14.

Frohling, E., & Szeliga, W. (2016). GPS constraints on interplate locking within the Makran subduction zone. *Geophysical Journal International*, 205(1), 67-76.

Heidarzadeh, M., Pirooz, M. D., Zaker, N. H., Yalciner, A. C., Mokhtari, M., & Esmaeily, A. (2008). Historical tsunami in the Makran Subduction Zone off the southern coasts of Iran and Pakistan and results of numerical modeling. *Ocean Engineering*, 35(8-9), 774-786.

Heidarzadeh, M., Pirooz, M. D., Zaker, N. H., & Yalciner, A. C. (2009). Preliminary estimation of the tsunami hazards associated with the Makran Subduction Zone at the northwestern Indian Ocean. *Natural Hazards*, 48(2), 229-243.

Heidarzadeh, M., & Kijko, A. (2011). A probabilistic tsunami hazard assessment for the Makran subduction zone at the northwestern Indian Ocean. *Natural Hazards*, 56(3), 577-593.

Kazeminezhad, M. H., Akbarpour Jannat, M. R., & Rastgoftar, E. (2026). Deterministic Tsunami Hazard Assessment for a Nearshore–Onshore Domain close to the Strait of Hormuz: The Overlooked Threat of the Western Makran Segment and Tidal Sensitivity. *International Journal of Coastal, Offshore & Environmental Engineering*, 10(1).

Momeni, P., & Goda, K. (2024). Probabilistic tsunami hazard assessment for the Makran Subduction Zone using logic tree and stochastic rupture sources. *Coastal Engineering Journal*, 1-29.

Rabinovich, A. B. (2009). Seiches and harbor oscillations. In *Handbook of Coastal and Ocean Engineering* (pp. 193-236). World Scientific.

Rajendran, C. P., Ramanamurthy, M. V., Reddy, N. T., & Rajendran, K. (2008). Hazard implications of the late arrival of the 1945 Makran tsunami. *Current Science*, 95(12), 1739-1743.

Rashidi, A., Ortwin, R., & Sadeghi, M. (2020). Coastal vulnerability assessment of the Chabahar Bay due to tsunami hazard. *Natural Hazards*, 103, 2215–2234.

Salah, P., Sasaki, J., & Soltanpour, M. (2021). Comprehensive probabilistic tsunami hazard assessment in the Makran subduction zone. *Pure and Applied Geophysics*, 178, 5085-5107.

Smith, G. L., McNeill, L. C., Wang, K., He, J., & Henstock, T. J. (2013). Thermal structure and megathrust seismogenic potential of the Makran subduction zone. *Geophysical Research Letters*, 40(7), 1528-1533.

Titov, V. V., & Synolakis, C. E. (1998). Numerical modeling of tidal wave runup. *Journal of Waterway, Port, Coastal, and Ocean Engineering*, 124(4), 157-171.

Vernant, P., Nilforoushan, F., Hatzfeld, D., Abbassi, M. R., Vigny, C., Masson, F., ... & Bayer, R. (2004). Present-day crustal deformation and plate kinematics in the Middle East constrained by GPS measurements in Iran and northern Oman. *Geophysical Journal International*, 157(1), 381-398.

Wells, D. L., & Coppersmith, K. J. (1994). New empirical relationships among magnitude, rupture length, rupture width, rupture area, and surface displacement. *Bulletin of the Seismological Society of America*, 84(4), 974-1002.

Zafarani, H., Etemadsaeed, L., Rahimi, M., Kheirdast, N., Rashidi, A., Ansari, A., ... & Eskandari-Ghadi, M. (2022). Probabilistic tsunami hazard analysis for Western Makran coasts, South-East Iran. *Natural Hazards*, 115(2), 1275-1311.